Magnetic Energy Release in Relativistically Expanding Magnetic Loops

January 2009

Chiba University
Department of Physics, Faculty of Science

Hiroyuki TAKAHASHI

HIROYUKI TAKAHASHI
Graduate School of Science and Technology, Chiba University
1-33, Yayoi-cho, Inage-ku, Chiba, 263-8522, Japan
email: takahasi@asro.s.chiba-u.ac.jp

ABSTRACT

We studied the mechanism of the magnetic energy release in the magnetosphere of strongly magnetized neutron star (magnetars) to explain giant flares observed in soft gamma-ray repeaters (SGRs). Since the magnetic field strength should be as large as 10^{15} Gauss to supply the energy of SGR giant flares (10^{47} erg), we should deal with the relativistic plasma in which the magnetic energy density exceeds that of the rest mass. As the model of observed flares in magnetars, we adopt a model that a magnetic energy is released in expanding magnetic loops. The magnetic loops emerging at the surface of the magnetar expand relativistically when they are twisted by crustal motions at their footpoints. Inside the magnetic loops, a current sheet is created. Magnetic reconnections taking place inside the current sheet can be responsible for the observed flares in magnetars. In this thesis, we studied the dynamics of the relativistically expanding magnetic loops and the magnetic reconnection inside such loops.

For the purpose of understanding the dynamics of the expanding magnetic loops, we obtained self-similar solutions of relativistically expanding magnetic loops. We neglect stellar rotation and assume axisymmetry and a purely radial flow. As the magnetic loops expand, the initial dipole magnetic field is stretched into the radial direction. Inside the magnetic loops, shell structures appear behind the loop top. Pressure and density pulses appear in the shell. Their amplitudes are larger for a thinner shell. When the expansion speed approaches the light speed, the displacement current reduces the toroidal current and modifies the distribution of the plasma lifted up from the central star. A current sheet is formed inside the magnetic loops.

Next, we extended the Sweet-Parker model of magnetic reconnections for relativistic plasma to study the magnetic energy release in the current sheet. The magnetic fields are assumed to reconnect steadily in a small thin rectangular dissipation region. Applying the conservation laws of mass and energy to the dissipation region, we obtain the relation between the inflow and outflow. The model takes account of the pressure gradient between the diffusion and outflow regions as well as increase in the inertia due to the thermal energy. For a fixed inflow velocity, the outflow velocity is faster when the ratio of the Poynting to kinetic fluxes of the inflow ($\sigma_{\rm i}$) is larger. The outflow velocity approaches to the saturation value in the limit of large $\sigma_{\rm i}$ owing to the increase in the inertia. The saturated velocity is reciprocal to square root of the inflow velocity. When the inflow speed is slow and the Poynting flux is dominant, the outflow can be relativistic. Our model reproduces the classical Sweet-Parker model when the magnetic energy density is much smaller than that of the rest mass. The outflow velocity depends also on the aspect ratio of the diffusion region, which is a free parameter in our model as well as in the Sweet-Parker model.

We performed 2-dimensional Particle-In-Cell (PIC) simulations of the magnetic reconnection to determine the reconnection rate for the relativistic magnetic reconnection, which cannot be determined by MHD analysis. We assumed the collisionless pair plasma and ignored the radiative processes. The results show that the outflow increases with $\sigma_{\rm i}$ when $\sigma_{\rm i} < 1$.

In the limit of large $\sigma_{\rm i}$, the outflow velocity converges to the saturation value, which is only mildly relativistic (Lorentz factor ~ 2). We found that the plasma heating rate is so large that the outflow cannot be ultra-relativistic. On the other hand, the thermal enthalpy linearly increases with $\sigma_{\rm i}$ without saturation. These results are consistent with those based on the MHD analysis. We conclude that the outflow velocity from the magnetic reconnection region is only mildly relativistic because the thermal energy mainly contributes to the plasma inertia.

PIC simulations of relativistic magnetic reconnection produced nonthermal particles accelerated in the reconnection region. We also carried out PIC simulations of the formation of the current sheets by applying shear motions at the footpoints of the magnetic loops. As the magnetic loops expand, Weibel instability grows ahead of the magnetic loops. We found that magnetic reconnection taking place in the expanding magnetic loops produce nonthermal particles with maximum energy ~ 3 MeV.

ACKNOWLEDGMENT

I greatly appreciate many people who give me their help to complete this thesis. I would like to express my most heartful thanks to Professor R. Matsumoto and Professor T. Hanawa. I thank Doctor E. Asano, Professor K. Shibata, Professor S. Shibata, Proffessor R. Horiuchi, Professor M. Hoshino, Professor K. Mase, Professor S. Miyaji, Professor S. Nitta, Professor H. Ohtani, Professor T. Terasawa, Professor S. Usami, Professor T. Yokoyama, Professor S. Yoshida, and Doctor S. Zenitani for discussions and valuable comments. I also thank members in Astrophysics Laboratory and Particle Physics Group at Chiba University.

Numerical works were performed on SX-6 at the Japan Aerospace Extrapolation Agency (JAXA), SR 11000 at Institute of Media and Information Technology (IMIT) of Chiba University, and XT4 at Center for Computational Astrophysics (CfCA) of National Astronomical Observatory, Japan (NAOJ).

I would like to express my gratitude to my friends for having fun with me and relaxation.

Finally I thank my family for their kind supports.

Contents

Chapter 1

Introduction

1.1 Introduction to Magnetar Flares

On December 27, 2004, solar system was exposed to an intense gamma-ray flux (~ 10 erg s^{-1} cm^{-2}) we'd never experienced (Mereghetti et al. 2005; Palmer et al. 2005). Because of the intense gamma-ray flux, almost all the gamma-ray detectors aboard the satellites were saturated. The gamma-ray detector aboard GEOTAIL spacecraft, which was launched with the aim of studying the structure and dynamics of the earth's magnetosphere, was not saturated because of its low energy sensitivity. The initial spike of the outburst was lasted for $T_{\rm dur} \sim 0.2$ sec with energies $\sim 10^{47}$ erg (Terasawa et al. 2005) followed by a long pulsating tail (Palmer et al. 2005). The Russian spacecraft Coronas-F also observed the flare without saturation (Mazets et al. 2005). When the outburst happened, the spacecraft was occulted by the Earth. Nevertheless, the detector could observe the outburst by observing the gamma-rays scattered by the Moon. It was the first observation of a cosmic gamma-ray flare reflected from a celestial body. The outburst is believed to be produced by a strongly magnetized neutron star called Soft Gamma-ray Repeaters (SGRs).

The outburst from soft gamma-ray repeaters was first observed on January 7, 1979. It was originally classified as Gamma-Ray Bursts (GRBs) with a short duration and a soft spectrum (Mazets & Golenetskii 1981). This identification was drastically changed soon. On March 5, 1979, a more energetic SGR burst was recorded from the same object SGR 1806-20. This extraordinary burst began with the bright spike with the luminosity peaking at $\sim 10^{45}$ erg s^{-1}, followed by a long pulsating tail with 8 s period whose flux decayed exponentially (Golenetskii et al. 1984). These multiple bursts clearly showed that the SGRs are completely different from the GRBs since GRBs occur only once when a

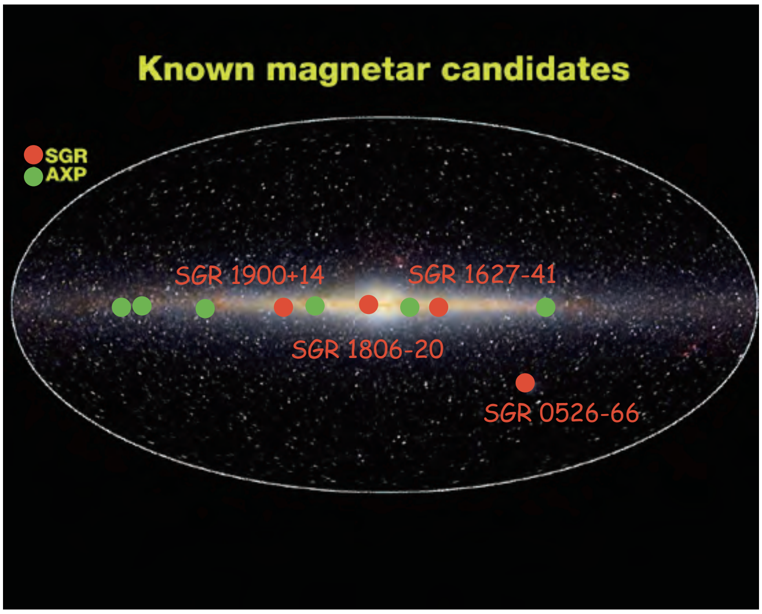

Figure 1.1: Locations of four known SGR candidates. Three of them are located in the plane of the Milky Way and one (SGR 0526-66) in the Large Magellanic Cloud (Image Credit: Rob Duncan)

massive star collapses (see Campana et al. 2006, for details of the relation between the GRBs and Supernova). For about 30 years from the first detection, many bursts have been observed from the same SGRs.

From a phenomenological point of view, the bursts are classified into three types.

- **short bursts** These are the most common, short durations ($\sim 0.1 - 0.2$ sec), less energetic SGR flares, the thermal spectrum, and the peak luminosity of $\sim 10^{41} - 10^{42}$ erg s^{-1}. This luminosity is above the Eddington luminosity for the standard neutron star, $L_{\mathrm{E}} \sim 10^{38}$ erg s^{-1}. These bursts are observed both in a single and multiple events.

- **intermediate bursts** This type of bursts are intermediate in the luminosity ($\sim 10^{41} - 10^{43}$ erg s^{-1}) and duration ($\sim 1 - 60$ sec) between the short bursts and giant flares.

- **giant flares** This is the most energetic event in SGR flares. They have durations with a few hundred seconds and luminosity of $\sim 10^{44} - 10^{47}$ erg s^{-1}. The intense spike is followed by a soft pulsating tail lasting hundreds of seconds.

Besides the three types of outbursts, persistent X-ray emissions from the SGRs are

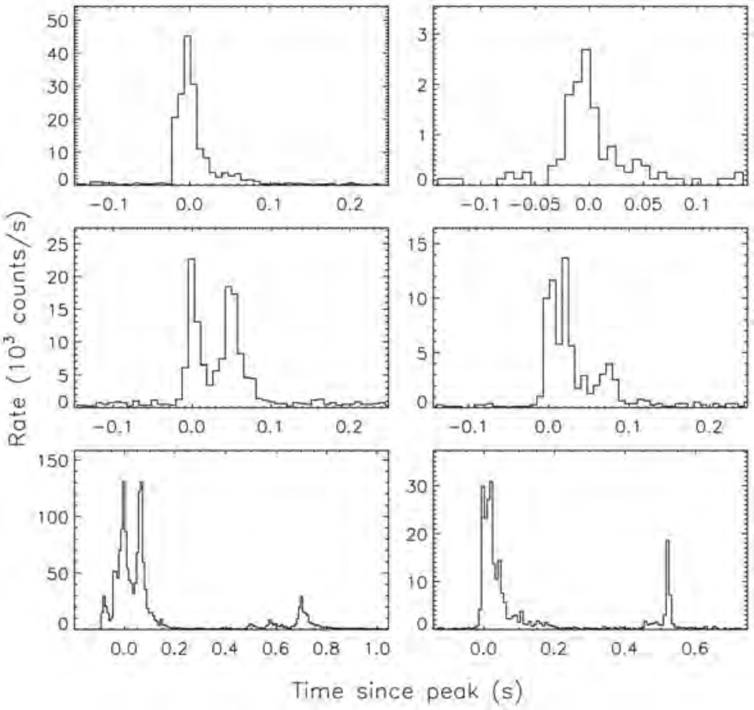

Figure 1.2: Time profile of some bursts in SGR 1900+14 and SGR1806-20 (Göğüş et al. 2001).

observed with luminosity $\sim 10^{34} - 10^{36}$ ergs^{-1} (Murakami et al. 1994; Rothschild et al. 1994; Vasisht et al. 1994). In the persistent emission, the X-ray pulse profile typically has two maxima per cycle. The pulse profile can be fitted by a simple sinusoidal function with period $P \sim 5 - 12$ sec (see Fig. 1.16, for the light curve of the persistent emission). The period of the X-ray pulse is considered to be the rotation period of the central star.

Four SGRs are found so far, three of which are in our Galaxy (SGR 18060-20, SGR 1900+14, SGR 1627-41) and one in the Large Magellanic Cloud (SGR 0526-66). Fig. 1.1 shows the location of the four known SGRs. Recently a new soft gamma-ray repeater SGR 0501+4516 (Denisenko 2008; Palmer & Barthelmy 2008; Woods et al. 2008; Israel et al. 2008) triggered four short bursts. Another new candidate SGR 1550-5418 is also discovered (Krimm et al. 2008; Rea et al. 2008a; von Kienlin & Briggs 2008; Rea et al. 2008b).

1.1.1 The Properties of the Short Bursts

Short bursts are the most common bursts from SGRs. Their properties do not vary between different sources (Aptekar et al. 2001; Göğüş et al. 2001). The bursts typically

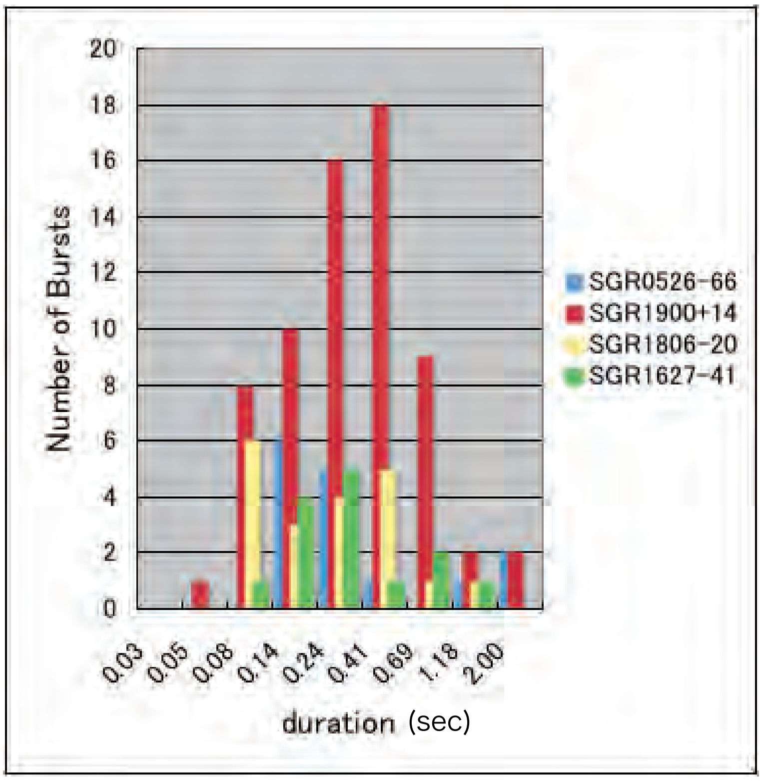

Figure 1.3: Distribution of the duration from the four SGRs by the Konus detectors between 1978 and 2000 (Aptekar et al. 2001).

show a rapid rise and a slower decay, which lasts $\lesssim$100 msec. Fig. 1.2 shows the light curve of the typical short bursts (Göğüş et al. 2001). A number of bursts have multiple peaks (middle plots in Fig. 1.2). Göğüş et al. (2001) showed that intervals between peaks have a broad distribution, which suggests that each burst does not have a correlation, and can be represented as the superposition of single bursts.

Although a number of broad-band spectroscopic studies of the short bursts were performed by many groups, its spectral model is still under discussions. Aptekar et al. (2001) found that the spectra can be well fitted by an optically-thin thermal bremsstrahlung (OTTB) with characteristic temperature ranging from 20 to 40 keV above 15 − 20 keV. Feroci et al. (2004) analyzed 1.5 − 100 keV BeppoSAX spectral properties from SGR 1900+14. They confirmed that the OTTB model provides acceptable spectral fit for energies higher than 15 keV, but it overestimates the flux at lower energies. Instead, they proposed the two component blackbody model or a cutoff power-low model as the more suitable spectral fitting model. Nakagawa et al. (2007) performed cumulative analysis of 50 bursts detected by *HETE-2* from SGR 1900+14. They concluded that the spectra

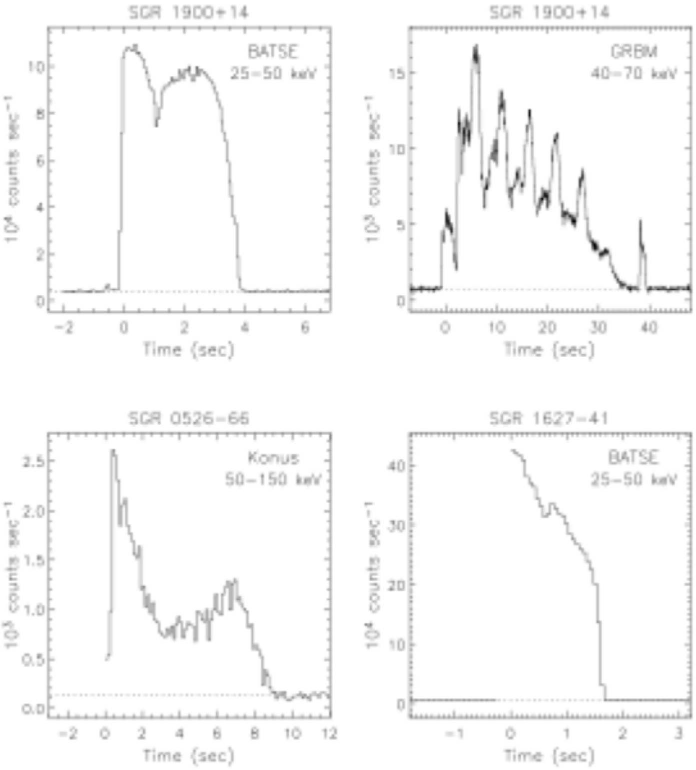

Figure 1.4: Time histories of four intermediate bursts for SGR 1900+14 (left top, right top) SGR 0526-66 (left bottom) and SGR 1627-41 (right bottom) (Woods & Thompson 2006).

from short bursts are well fitted by two blackbody model with temperatures $T_l \sim 4$ keV and $T_h \sim 11$ keV. These temperatures do not seem to depend on the burst intensity.

Fig. 1.3 shows the distribution of the duration of bursts in four known SGRs (Aptekar et al. 2001). Note that the burst duration has a narrow distribution. Average duration for SGR 0526-66, SGR 1900+14, SGR 1806-20, and SGR 1627-41 are 0.58 sec, 0.4 sec, 0.24 sec, and 0.26 sec, respectively. The coincidence of the duration between each SGR burst suggests that each burst has the same typical size and the same mechanism.

1.1.2 The Properties of the Intermediate Bursts

The intermediate flares are intermediate in the luminosity and the duration between the short burst and the giant flares. They are commonly observed in a few days or a few weeks after the giant flares. This fact suggests that they represents the residual energy release of the giant flare. Fig. 1.4 shows the time histories of four intermediate bursts. Their energy range is $10^{41} - 10^{43}(\Omega/4\pi)$ erg, where Ω is the opening angle. Their durations are

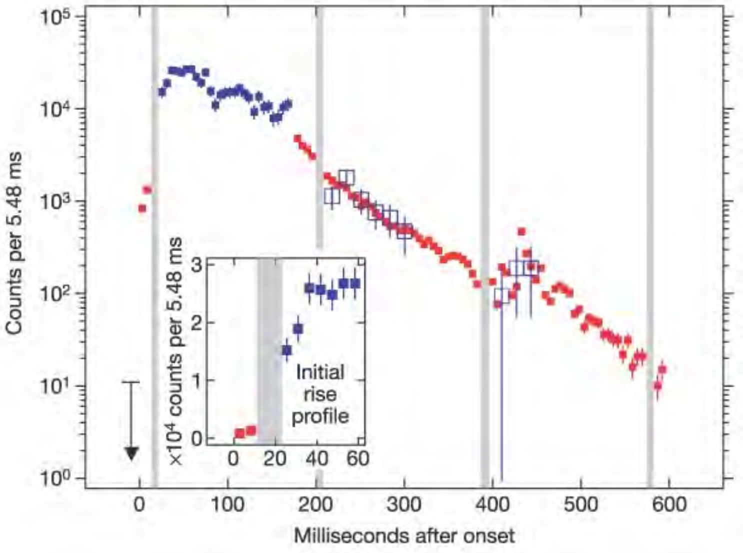

Figure 1.5: Time history of the photon counts during 600 ms of the giant flare from SGR 1806-20 (Terasawa et al. 2005).

typically a few seconds, but sometimes burst continues for several tens of seconds, longer than the rotation period of the central star (see § 1.2.1).

The spectra of the intermediate bursts are similar to those of the short bursts (Olive et al. 2004). The OTTB model overestimates the low energy (< 15 keV) flux. The broadband spectra in the range $7 - 100$ keV can be fitted by two component blackbody model with temperatures $T_l = 4.3$ keV and $T_h = 9.8$ keV. These properties are almost common with those of short bursts. The radiation spectra do not change between each burst.

1.1.3 The Properties of the Giant Flares

The giant flares are the most energetic SGR outbursts typically releasing the energy $\sim 10^{44} - 10^{47}$ erg in a short time (< 1 sec). Only three of giant flares have been recorded in decades: SGR 0526-66 on March 5, 1979 (Mazets et al. 1979), SGR 1900+14 on August 27, 1998 (Hurley et al. 1999), and SGR 1806-20 on December 27, 2004 (Hurley et al. 2005; Terasawa et al. 2005; Palmer et al. 2005; Mereghetti et al. 2005; Mazets et al. 2005).

The giant flare from SGR 1806-20 on December 27, 2004, is an exceptionally powerful phenomenon with the hard spike lasting $\lesssim 0.2$ sec. Fig. 1.5 shows the photon counts during the first 600 ms of the giant flares from the Low Energy Particle (LEP) experiment

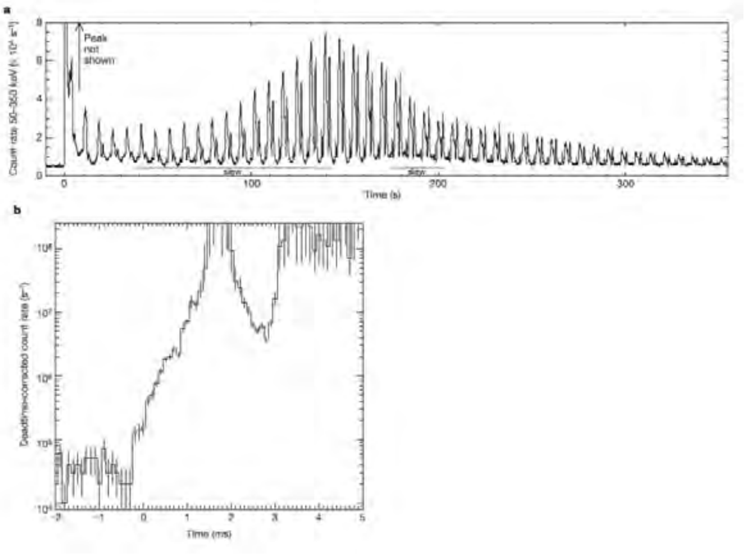

Figure 1.6: Light curve of the SGR spike and tail from the Burst Alert Telescope (BAT) on *Swift* at measured energy > 50 keV (Palmer et al. 2005) observed in SGR 1806-20. The pulsation at the long tail corresponds to the rotation period of the central star.

on GEOTAIL (Terasawa et al. 2005). After the initial spike with duration ~ 0.2 sec, the photon count decays exponentially with an e-foldind time of ~ 66 msec. Between $t = 397$ and 500 msec, several humps are observed. These humps may indicate the energy re-injection from the central engine.

Fig. 1.6 shows the light curve of the initial spike and the tails from the Burst Alert Telescope (BAT) on *Swift* (Palmer et al. 2005). The initial spike is followed by a long (~ 600 sec) pulsating tail. The pulsation period observed in the tail corresponds to the rotation period of the central star (Hurley et al. 2005; Palmer et al. 2005). It is difficult to infer the peak luminosity of the spike since almost all the instruments were saturated. The GEOTAIL, whose detectors was not saturated during the peak, revealed an isotropic peak luminosity of $\sim 2 \times 10^{46} d_{15}^2$ erg s^{-1}, where d_{15} is the distance to the source in the unit of 15 kpc. The tail luminosity which were measured by several instruments were $\sim 5 \times 10^{43} d_{15}^2$ erg s^{-1} comparable with the other giant flares. After about a week later, a radio afterglow was detected (Cameron et al. 2005). Its fluence (0.3 erg cm^{-2}) is a few hundred times larger than that of the previous giant flares.

The spectrum of the SGR burst can be fitted with exponential-cutoff power law of a photon index -0.2 for the spike, and a blackbody spectrum with the temperature $\sim 15 - 30$ keV for the tail (Palmer et al. 2005). The fitting model of the spectra, however,

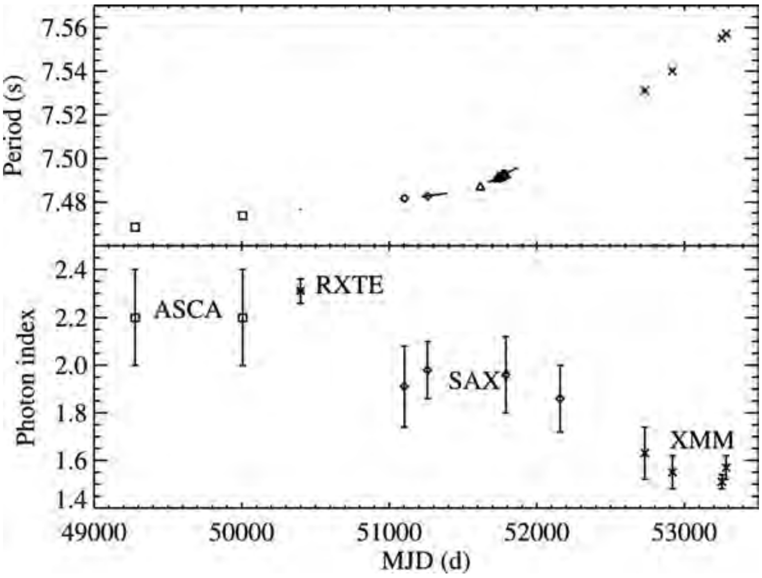

Figure 1.7: Long-term evolution of the pulse period (top) and power-law photon index (bottom) of SGR 1806-20 (Mereghetti et al. 2005).

is not conclusive because the events are rare.

Mereghetti et al. (2005) studied the low energy (< 10 keV) X-ray emission from the SGR 1806-20 for two years before the giant flares. They found that the source went to the different states of activity over the 2003-2004 period. Fig. 1.7 shows the time history of the photon index and rotation period in the quiescent phase. The $2 - 10$ keV flux increased and reached the twice of the historical level observed previously. The spectrum became hard with the power-law index decreasing from 2.2 to 1.5. The spin-down period rate (time derivative of the rotation period) became higher than the value observed in the previous year. After the giant flare event, these values returned to those in the quiescent phase (Rea et al. 2006). The spectrum softened with the power-law index ~ 1.8. The flux decreased to the level 20% lower than the preflare phase, which is larger than the quiescent phase. These results suggest that the burst energy is stored on the surface of the central star (active region) before the giant flares. The active region emits radiation with harder spectrum. The emergence of the active region results in the increase in the moment of inertia (increase in the spin period). Giant flares are driven by release of the stored energy. After the giant flare, the active region gradually evaporates in parallel to the decrease in the moment of inertia and softening of the spectrum. The SGRs go back to the quiescent phase.

1.2 The Origin of the SGRs outbursts.

1.2.1 The Evidences of the Strongly Magnetized Neutron Star

As discussed in § 1.1, persistent X-ray emissions from SGRs are observed. The light curve of the persistent emission can be fitted by the sinusoidal functions, similarly to the Pulsars, which originate from the neutron star. The similarity between these objects suggests that the SGRs flares also originate from the strongly magnetized star. In what follows, we evaluate the magnetic field strength of the central star of SGRs.

Suppose that a neutron star of radius $R_{\rm s}$ and moment of inertia I rotates with angular velocity $\Omega = 2\pi/P$, where P is the rotation period. The rotational energy and its time derivative are given as

$$\begin{aligned} E_{\rm rot} &= \frac{1}{2} I\Omega^2 \simeq 2\times 10^{46} I_{45} P^{-2} \ {\rm erg} && (1.2.1)\\ \dot{E}_{\rm rot} &= I\Omega\dot{\Omega} \simeq -4\times 10^{31} I_{45} \dot{P}_{-15} P^{-13} \ {\rm erg\ s^{-1}}, && (1.2.2) \end{aligned}$$

where P is in seconds, $\dot{P}_{-15} \equiv \dot{P}/10^{-15}$, and $I_{45} \equiv I/10^{45}$ g cm^2. $\dot{E}_{\rm rot}$ is called *spin-down luminosity*. Let us assume that a magnetic dipole field is attached to the central star with the mean strength of the magnetic field at the stellar surface $B_{\rm s}$. The magnetic dipole field rotating in a vacuum will emit energy at rate

$$L_{\rm mag} = \frac{2}{3c^3} B_{\rm s}^2 R_{\rm s}^2 \Omega^4, \qquad (1.2.3)$$

where c is the light speed. Here, we assume that the magnetic moment is parallel to the spin axis. From equation (1.2.2) and (1.2.3), the magnetic field strength $B_{\rm s}$ is estimated as

$$B_{\rm s} = \sqrt{\frac{3}{8\pi^2}\frac{Ic^3}{R^6} P\dot{P}} \simeq 3.2\times 10^{19} I_{45}^{\frac{1}{2}} R_{\rm s,6}^{-3} \sqrt{P\dot{P}}\ G, \qquad (1.2.4)$$

where $R_{\rm s,6} \equiv R_{\rm s}/(10^6$ cm$)$. Fig. 1.8 shows the period (P) versus period derivative ($\dot{P}$) for radio pulsars (crosses), Anomalous X-ray Pulsars (red squares), and Soft Gamma-ray Repeaters (blue diamonds). Contours show the magnetic field strength given by equation (1.2.4). The Anomalous X-ray pulsars (AXPs) also originate from the magnetars. They are less active than the SGRs. Since the SGRs have the long rotation period ($P \sim 5 - 12$ sec) and smaller spin down age ($P/\dot{P} \sim 10^3 - 10^5$ yrs), the estimated magnetic field strength is $\sim 10^{15}$ G, which is stronger than that of the radio pulsars. Thus they are called *Magnetars*.

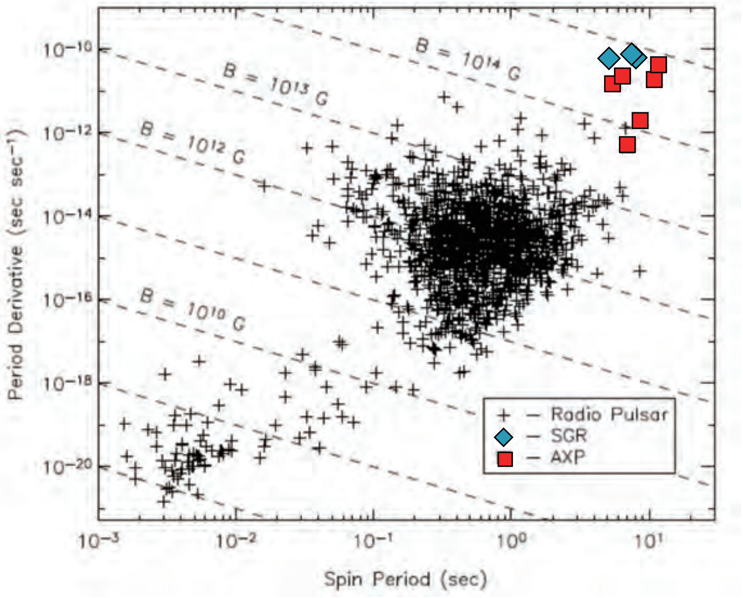

Figure 1.8: Period P versus period derivative $\dot{P}$ for radio pulsars (crosses), Anomalous X-ray Pulsars (red squares), and Soft Gamma-ray Repeaters (blue diamonds). Contours show the magnetic field strength given by equation (1.2.4) (Woods & Thompson 2006).

The corresponding magnetic energy stored inside the magnetar is

$$E_{\rm mag} = \frac{4\pi R_s^3}{3}\frac{B^2}{8\pi} \sim 2\times 10^{47}\left(\frac{R_s}{10\ {\rm km}}\right)^3\left(\frac{B}{10^{15}\ {\rm G}}\right)^2\ {\rm erg}. \tag{1.2.5}$$

Although the rotation energy $E_{\rm rot}$ given by equation (1.2.2) is less than the observed energy of the giant flare, the magnetic energy is comparable or larger if the magnetic field strength inside the magnetar is larger than that on the surface of the magnetar. The magnetic field strength inside the magnetar is in principle as strong as 3×10^{17} G (Thompson & Duncan 1993). Since the rotational energy corresponding to the rotation period $\sim 5-12$ sec can not explain the observed energy of the giant flares, it is considered that the dissipation of the magnetic energy is responsible for the flares.

Another evidence for the magnetar with the ultra-strong magnetic field is the observation of the proton-cyclotron resonance feature (Strohmayer & Ibrahim 2000; Ibrahim et al. 2002, 2003). Strohmayer & Ibrahim (2000) presented the evidence of 6.4 keV and ~ 13 keV emission lines during a burst from the SGR 1900+14. The harmonic relationship between these lines is suggestive of cyclotron emission. Ibrahim et al. (2003) reported the evidence of the cyclotron resonance feature from the precursor of the SGR outburst (see Fig. 1.9). The features consist of the 5.0 keV absorption line with its second and third

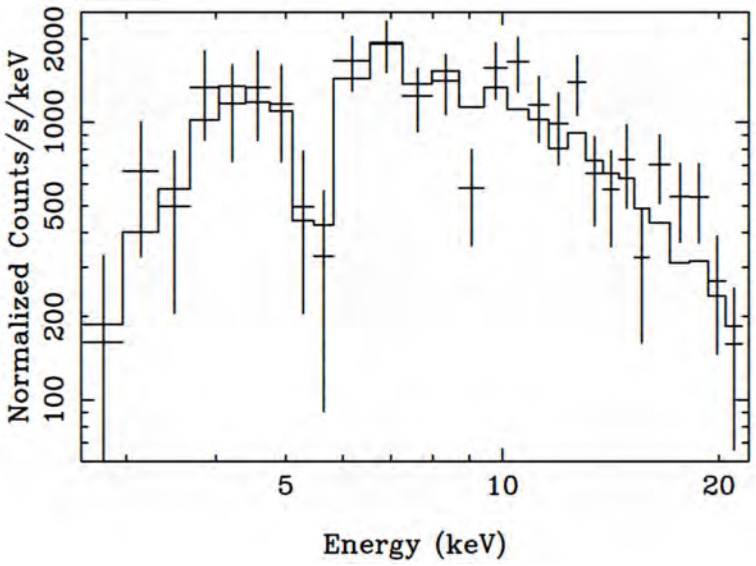

Figure 1.9: The spectrum of the burst from SGR 1806-20 on 50405.3704 (MJD). The line absorption feature of the proton-cyclotron resonance is shown around 5 keV (Ibrahim et al. 2003).

harmonics (11.2 and 17.5 keV). If the resonant lines correspond to the proton cyclotron lines, the implied surface field strength is $\sim 10^{15}$ G.

1.2.2 The Magnetar Model of the SGR Outbursts

To explain the SGR activity, a variety of models were proposed such as the accretion onto the magnetized neutron star (Livio & Taam 1987; Katz et al. 1994) and accretion onto a quark star (Alcock et al. 1986). These models were excluded by observations for optical/IR counterparts. The counterparts have been identified for five magnetars (including AXPs). Since all the counterparts are very faint (the ratio of the X-ray to IR fluxes is larger than a few thousands), the presence of the normal stars is excluded (see Mereghetti 2008, for review). van Paradijs et al. (1995) and Ghosh et al. (1997) proposed the model that the fossil disk, which is formed at the core collapse of the massive star, accretes to the standard neutron star with magnetic field strength of $\sim 10^{13}$ G.

Duncan & Thompson (1992) and Thompson & Duncan (1993) proposed another model of the SGR flares which is similar to that for the solar flares. When the massive star collapses, the entropy decreases with radius since the outgoing shocks weaken. Such a entropy gradient in radial direction results in convectively unstable state (Bethe et al. 1987; Mayle & Wilson 1988). Since the relativistic electrons can transport the charge

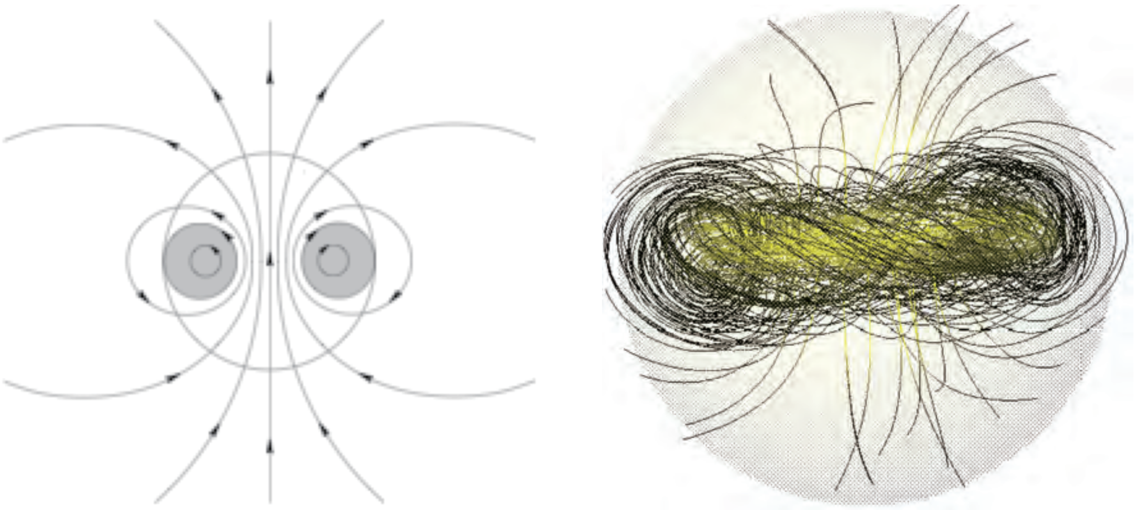

Figure 1.10: Left: Schematic picture of the stable configuration of the magnetic field. Solid curves show the poloidal magnetic fields, while the shaded area shows the toroidal magnetic fields. Right: Magnetic field configuration inside the magnetar. A transparent sphere shows the surface of the star (Braithwaite & Spruit 2006).

current, the magnetic Reynolds number is large ($\sim 10^{17}$) enough to attain the ideal MHD condition. The convective motion and the low resistivity suggest that the magnetic fields are twisted and amplified by the dynamo mechanism. Also the differential rotation inside the magnetar can twist and amplify the magnetic fields. The amplified magnetic field strength is up to 3×10^{17} G (Thompson & Duncan 1993).

Such a strong magnetic field thrusts the Lorentz force on the crust of the magnetar (Thompson et al. 2002). The Lorentz force is balanced with the rigidity of the crust. When the critical twist is accumulated, the magnetic twist is injected into the magnetar magnetosphere by cracking the crust ('crustquake'). The large scale twist injection of the magnetic flux into the magnetosphere increases the torque and it results in the increase in the spin-down rate. Braithwaite & Nordlund (2006) studied the evolution of the magnetic fields in stellar interior after the star is formed. Inside the star, a tori of the twisted magnetic fields is created. The field configuration outside the star is approximately dipole (see Fig. 1.10). Interestingly these properties are independent of the initial field configurations. Braithwaite & Spruit (2006) calculated the Maxwell stress exerted on the crust. They found that the large stresses are built up in the crust, which will lead to crustquake.

The resulting crustquake will eject hot plasma into the magnetar magnetosphere (active region). The Alfvén waves propagating along the field lines heat the plasma. Also the

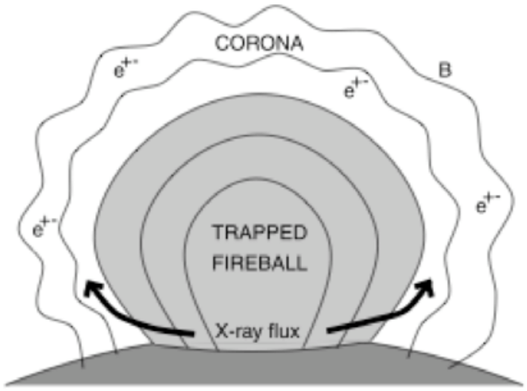

Figure 1.11: Schematic picture of the formation of a trapped fireball on the surface of the magnetar (Thompson & Duncan 2001).

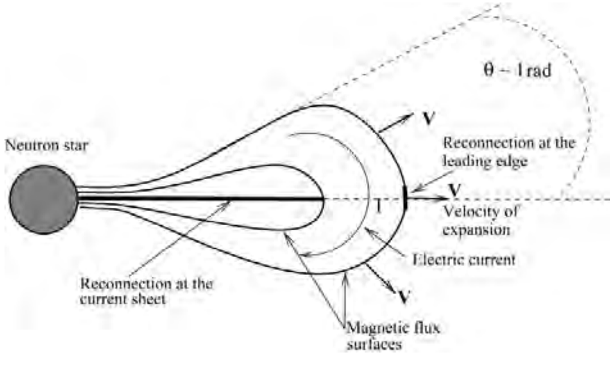

Figure 1.12: Evolution of the expanding magnetic loops (Lyutikov 2006). Solid curves show the magnetic field lines. A current sheet is formed inside the magnetic loops.

induced electric field by the twist motion can accelerate particles. Such accelerated particles emit high energy photons. The interaction between the high energy photons and the magnetic fields leads to the pair cascade. The generated leptons are trapped by the strong magnetic fields. The active region on the magnetar surface quickly becomes optically thick (namely, "trapped fireball", see Fig. 1.11) (Thompson & Duncan 1995). Beloborodov & Thompson (2007) performed 1-dimensional electrostatic particle simulations by including the effect of the pair creation and the external gravity. The leptons are accelerated by the induced electric field, resulting in the avalanches of the pair creation. The hot plasma in magnetosphere persists in dynamic equilibrium. Since the plasma density increases through the pair creation process, the density level exceeds the Goldreich-Julian density (see Goldreich & Julian 1969, for the definition of the Goldreich-Julian density). Plasma can shield the electric field $\boldsymbol{E} = -\boldsymbol{v} \times \boldsymbol{B}/c$ induced by the crustal motions. Since the magnetic field and plasma are well coupled each other, the magnetic fields in the magnetar magnetosphere is twisted by the crustal motion.

The twisted magnetic fields in the magnetar magnetosphere will expand by the enhanced magnetic pressure (see Fig. 1.12). Such expanding magnetic loops driven by the twist injection at the footpoints of them were originally proposed as the model of the solar flares (Barnes & Sturrock 1972; Forbes & Priest 1982; Forbes & Priest 1983; Forbes & Priest 1984; Mikic et al. 1988). Mikic et al. (1988) carried out 3-dimensional non-relativistic magnetohydrodynamical (MHD) simulations of the expanding magnetic loops as a model of solar flares. The left panel of Fig. 1.13 shows the initial condition of their

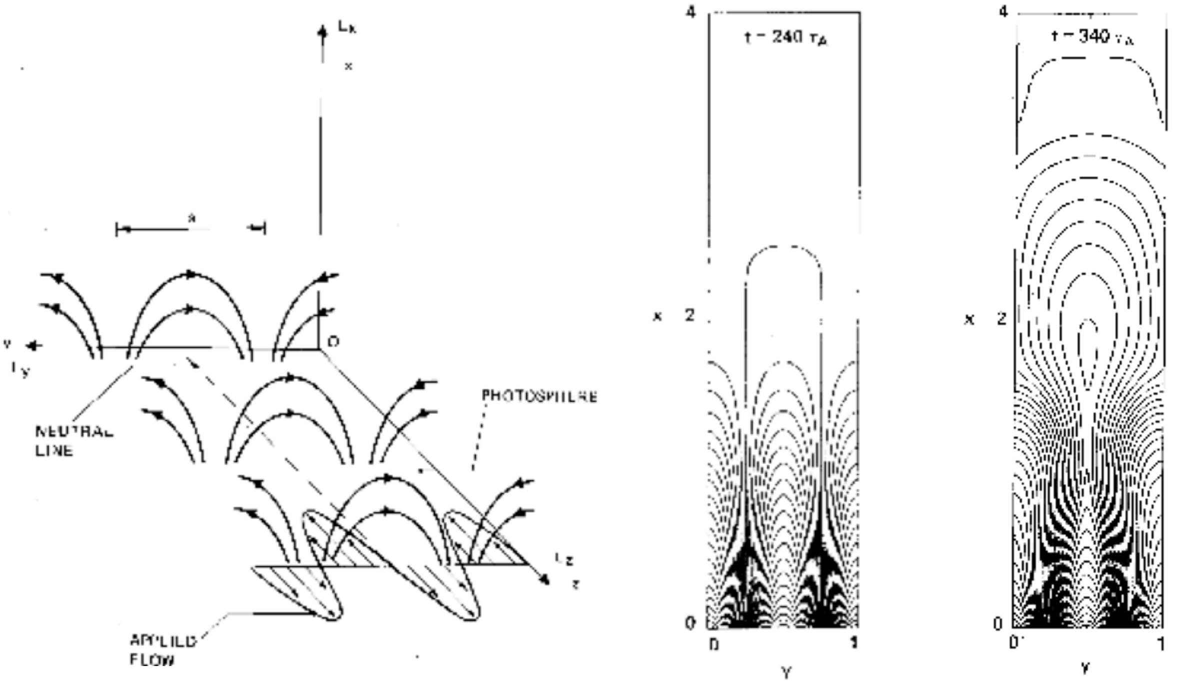

Figure 1.13: Left: Schematic picture of the twist motion at the footpoints of magnetic loops. Right: Result of the non-relativistic MHD simulation of the expanding magnetic loops. A magnetic reconnection takes place inside the magnetic loops (Mikic et al. 1988).

simulations. The centre and right panels show the magnetic field lines obtained by MHD simulations. By the twist injection at the footpoints of the magnetic loops, the magnetic field lines are twisted because the magnetic fields are frozen in. The toroidal (Z component of the) magnetic fields are created inside the magnetic loops. The magnetic loops then expand in the vertical (X) direction. A current sheet is created inside the elongated magnetic loops. The magnetic reconnection taking place in the current sheet can liberate the magnetic energy stored inside the magnetic loops (see § 1.3 for the magnetic reconnection). In these processes, the twist injection increases the magnetic energy contained inside the magnetic loops (free energy). The accumulated energy is converted into the kinetic and thermal energies by the magnetic reconnection inside the current sheet. Similar models are proposed for flares observed in the protostars (Hayashi et al. 1996), jets from the X-ray binaries (Kato et al. 2004), and jets from the Active Galactic Nuclei (AGNs) (Meier et al. 2001).

In the magnetar and neutron star magnetosphere, the magnetic energy is dominant to other energies such as the plasma rest mass energy and the thermal energy. Thus it is plausible to ignore the plasma inertia and the pressure. This approximation is called the force-free approximation (Uchida 1997a; Uchida 1997b, see Appendix A.1).

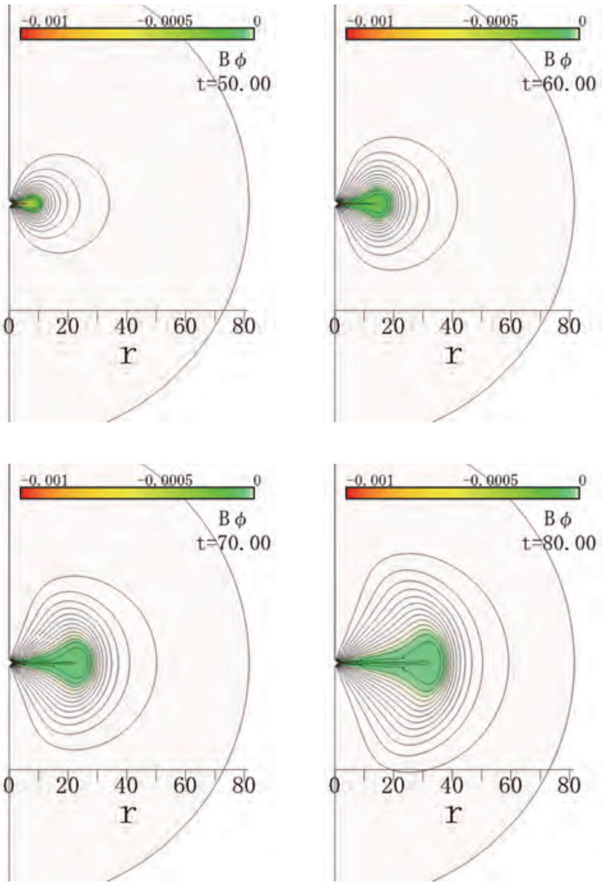

Figure 1.14: Resuls of the relativistic force-free simulations of the expanding magnetic loops. Curves show the magnetic field lines and color shows the radial velocity (Asano 2007).

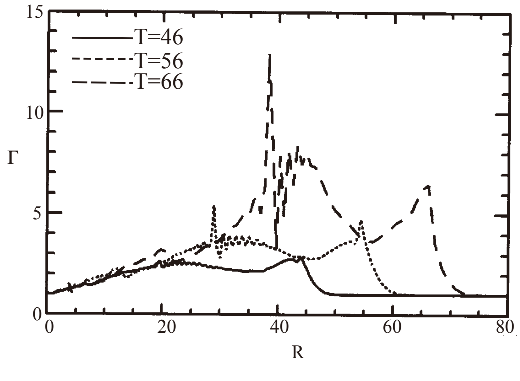

Figure 1.15: Plasma drift velocity of the expanding magnetic loops on the equatorial plane. Solid curve shows the distribution at $t = 46\tau_c$, while dotted and dot-dashed ones are at $t = 56\tau_c, 66\tau_c$, respectively. Here τ_c is the light crossing time $\tau_c \equiv R_s/c$ and R_s is the stellar radius. The velocity profile indicates that the magnetic loops expand self-similarly (Asano 2007).

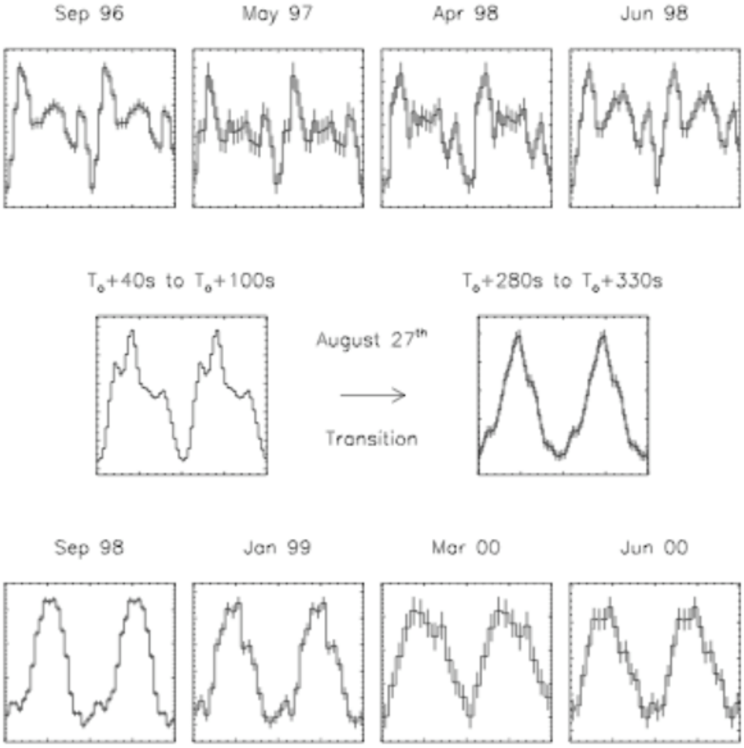

Figure 1.16: Evolution of the pulse profile of SGR 1900+14 over 3.8 years. All the panels show the pulse profile per 2 cycles and vertical axis shows the photon count rates with arbitrary unit. The giant bursts occurred on August 27, 1998 (Woods et al. 2001).

The force-free approximation is applied to study the dynamics in the neutron star magnetosphere (Komissarov 2002; Asano et al. 2005; Spitkovsky 2006). Spitkovsky (2005) applied 2-dimensional relativistic force-free code to study the evolution of the magnetic loops by imposing the twist motion at the footpoint of them. When the critical twist is accumulated, the magnetic loops expand relativistically. Asano (2007) carried out 2-dimensional relativistic force-free simulations of expanding magnetic loops. Fig. 1.14 shows the time evolution of the expanding magnetic loops. Color contours show the toroidal (azimuthal) magnetic field and curves show the magnetic field lines. Fig. 1.15 shows the Lorentz factor defined by the drift velocity $\boldsymbol{v}_d = c(\boldsymbol{E} \times \boldsymbol{B})/B^2$ at the equatorial plane. They showed that the maximum Lorentz factor exceeds 10. These results indicate that the magnetic loops expand *self-similarly*.

Inside the expanding magnetic loops, a thin current sheet is formed, which is similar to that found in the previous study of the solar flares. Lyutikov (2006) proposed that the magnetic reconnection taking place inside the current sheet is responsible for the magnetar flares. When the magnetic reconnection takes place, topology of the magnetic field lines is drastically changes and liberates the magnetic energy.

Woods et al. (2001) studied the evolution of the pulse profile of SGR 1900+14 before and after the giant flare occurred on August 27, 1998. Fig. 1.16 shows the pulse profile per 2 cycles of SGR 1900+14. The vertical axis shows the photon count rates in arbitrary unit. At the time of the giant flare on August 27, 1998, the pulse profile of the persistent emission changed dramatically from a complex, multi-peak morphology to a simple sinusoidal morphology. The complex profile of the pulse profile can be explained by the formation of the trapped fireball. The simple sinusoidal profile of the light curves radiated by the dipole fields is modified by the formation of the fireball. The reconfiguration of the magnetic field topology (magnetic reconnection) inside the fireball can be responsible for the simplification of the pulse profile by evaporating the fireball.

1.3 Magnetic Reconnection

A model of the magnetic reconnection was originally proposed by Sweet (1958) and Parker (1957) (called Sweet-Parker model) to explain the solar flares. Petschek (1964) proposed a model of the magnetic reconnection including the slow shocks attached to the dissipation region (Petschek 1964). The latter model can liberate the magnetic energy faster than the Sweet-Parker model. Although these models are originally based on the non-relativistic magnetohydrodynamics, it has also been studied as the energy conversion mechanism in the high energy astrophysical objects, such as the rotation-powered pulsars (Coroniti 1990; Lyubarsky & Kirk 2001), the magnetohydrodynamic acceleration of the relativistic jets (Meier et al. 2001), Gamma-ray bursts (Drenkhahn & Spruit 2002; Drenkhahn 2002) and SGR flares (Woods et al. 2001; Lyutikov 2006).

In this section, the conventional Sweet-Parker type magnetic reconnection model and the recent studies of the relativistic magnetic reconnection are reviewed.

1.3.1 Non-relativistic Sweet-Parker Magnetic Reconnection

Let us consider the steady state magnetic reconnection in Cartesian coordinate. The neutral sheet is located on the $Y = 0$ plane. All the physical properties are independent of Z (2-dimensional). The electric resistivity is applicable within the region of $|X| < \delta$ and $|Y| < L$ (see Fig. 1.17). The ideal MHD condition is applied outside the diffusion region. The diffusion region is lying between the oppositely directed magnetic fields with the strength B_0. The plasma density ρ and magnetic fields $\boldsymbol{B}$ are assumed to be uniform in the inflow and outflow regions. We also assume that the plasma pressure p is negligible compared to the magnetic pressure. The subscripts i, o, and d denotes inflow, outflow, and dissipation regions, respectively.

From the Ampere's law, the charge current inside the dissipation region is estimated as

$$j_z = \frac{cB_\mathrm{i}}{4\pi\delta}. \tag{1.3.1}$$

From the Gauss's law, the magnetic field in the outflow region is given by

$$B_\mathrm{o} = \frac{\delta}{L} B_\mathrm{i}. \tag{1.3.2}$$

Next, let us estimate the outflow velocity from the magnetic reconnection. The equation of motion between the neutral point and the outflow region is approximately given by

$$\rho(\boldsymbol{v} \cdot \nabla)\boldsymbol{v} \simeq \frac{1}{c}\boldsymbol{j} \times \boldsymbol{B}. \tag{1.3.3}$$

Here we ignore the pressure term. Substituting equations (1.3.1) and (1.3.2) into equation (1.3.3), and replacing ∇ by $1/L$, we obtain

$$v_\mathrm{o} \simeq \frac{B_\mathrm{i}}{\sqrt{4\pi\rho_\mathrm{o}}}. \tag{1.3.4}$$

When we assume the incompressibility, i.e., $\rho_\mathrm{i} = \rho_\mathrm{o}$, we obtain

$$v_\mathrm{o} \simeq \frac{B_\mathrm{i}}{\sqrt{4\pi\rho_\mathrm{i}}} \equiv v_A, \tag{1.3.5}$$

where v_A is the Alfvén velocity of the inflow region. Thus the outflow is accelerated up to the Alfvén velocity of the inflow.

The Z-component of the electric field in the inflow region and dissipation region is written as

$$E_\mathrm{i} = \frac{1}{c} v_\mathrm{i} B_\mathrm{i}, \tag{1.3.6}$$

and

$$E_\mathrm{d} = \eta j, \tag{1.3.7}$$

respectively. Here η is the magnetic diffusivity. Since the electric field should be uniform ($\nabla \times \boldsymbol{E} = 0$ from Faraday's law), we obtain

$$v_\mathrm{i} = \frac{c^2\eta}{4\pi\delta}, \tag{1.3.8}$$

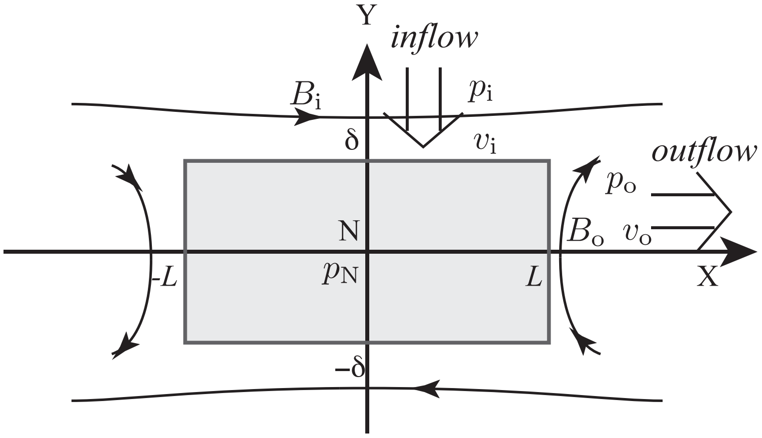

Figure 1.17: Schematic picture of the magnetic reconnection. Solid curves show the magnetic field lines and grey area shows the diffusion region.

from equations (1.3.1), (1.3.6), and (1.3.7).

By assuming the incompressibility, the continuity equation can be written as

$$v_\mathrm{i} L = v_\mathrm{o} \delta. \tag{1.3.9}$$

Substituting equation (1.3.9) into equation (1.3.8), we obtain

$$v_\mathrm{i} = v_A R_M^{-1/2}, \tag{1.3.10}$$

where R_M is the magnetic Reynolds number defined as

$$R_M \equiv \frac{4\pi v_A L}{\eta c^2}. \tag{1.3.11}$$

Since the magnetic Reynolds number is large ($\sim 10^4 - 10^5$), the inflow velocity (reconnection rate) is much smaller than the Alfvén velocity. Thus the Sweet-Parker type magnetic reconnection is considered as the 'slow' process.

1.3.2 Relativistic Sweet-Parker Magnetic Reconnection

In the previous subsection, we showed that the outflow is accelerated up to the Alfvén velocity of the inflow. When the magnetic field energy is much larger than that of rest mass in the inflow region, the outflow is expected to be ultra-relativistic (see Appendix A.3.2, for the definition of the Alfvén velocity in the relativistic MHD). Blackman & Field (1994) and Lyutikov & Uzdensky (2003) studied the Sweet-Parker type relativistic magnetic reconnection for the relativistic plasma. They concluded that the outflow speed

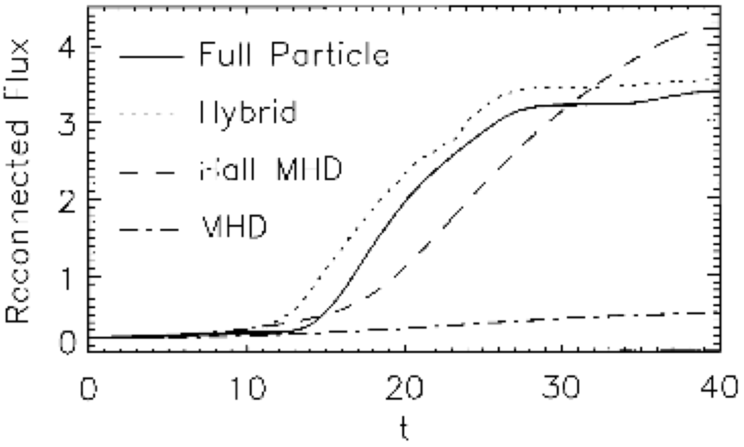

Figure 1.18: Time history of the reconnected magnetic flux from full particle, hybrid, hall MHD, and MHD simulations (Birn et al. 2001).

becomes ultra-relativistic. They also concluded that the reconnection rate is enhanced due to the Lorentz contraction. In their treatment, the pressure term is ignored as the conventional manner. Lyubarsky (2005) pointed out the importance of increase in inertia due to the larger thermal energy. The larger thermal energy contributes to the plasma inertia (see Appendix A.1). The pressure balance across the current sheet demands the following equation

$$p_{\rm d} = \frac{B_{\rm i}^2}{8\pi}, \tag{1.3.12}$$

where $p_{\rm d}$ is the gas pressure inside the diffusion region. For the larger magnetic fields ($B_{\rm i}^2/(8\pi) >> \rho c^2$, hereafter we call ‘relativistic’), the thermal energy density also exceeds that of rest mass. The larger thermal energy contributes to the plasma inertia. He concluded that the outflow velocity is only mildly relativistic (Lorentz factor $\gamma \sim 1$) and the reconnection rate is not enhanced ($v_{\rm i}/v_{\rm o} \simeq \delta/L$). The possibility of the faster outflow from the relativistic magnetic reconnection is under discussion.

1.3.3 Numerical Approaches to the Magnetic Reconnection

A number of numerical simulations on the non-relativistic magnetic reconnection have been performed in MHD (Ugai & Tsuda 1977; Sato & Hayashi 1979; Biskamp 1986; Birn & Hesse 2001). Also a number of Particle-In-Cell (PIC) simulations have been performed, which can appropriately treat the effect of the finite Larmor radius and non-thermal particles (Horiuchi & Sato 1997; Hesse et al. 1999; Drake et al. 2003; Hoshino et al. 2001). In the non-relativistic simulations, the outflow is accelerated up to the

Alfvén velocity, but the inflow speed (reconnection rate) depends on models. Birn et al. (2001) showed that inflow velocity is smaller for MHD simulations than for the Hall MHD, Hybrid, and PIC simulations. They concluded that the Hall term (which originates from the difference in the inertia between the electrons and ions) is important to explain the larger reconnection rate (smaller R_M). Horiuchi & Sato (1997) and Hesse et al. (1999) performed PIC simulations and showed that the reconnection rate is independent of the mass ratio between the electrons and ions. Hesse et al. (1999) reported that the off-diagonal term of the pressure tensor mainly contributes to a larger reconnection rate.

In the relativistic regime, many authors have performed PIC simulations in 2D (Zenitani & Hoshino 2001; Jaroschek et al. 2004; Zenitani & Hoshino 2007; Karlický 2008; Lyubarsky & Liverts 2008) and in 3-D (Zenitani & Hoshino 2005; Zenitani & Hoshino 2008). Zenitani & Hoshino (2001) showed that the reconnection rate $cE_z/(B_0V_\mathrm{o})$, where E_z and B_0 are the electric fields induced by the magnetic reconnection and the magnetic field strength of the inflow, respectively, is about 0.3, while Jaroschek et al. (2004) showed that it is about 1.5 since additional electric fields are generated by the multiple current sheet interaction. The shape of the reconnection region indicates that it is Sweet-Parker type (Zenitani & Hoshino 2007, see Fig. 1.19). They showed that the outflow velocity does not become ultra-relativistic, as predicted by Lyubarsky (2005). But the reason of the slower outflow (compared to the Alfvén velocity) is not understood.

Watanabe & Yokoyama (2006) performed 2-dimensional relativistic resistive MHD simulations. Color contours in Fig. 1.20 show the density, while the curves and the arrows show the magnetic field lines and the velocity field, respectively. Since an anomalous resistivity is implemented in their model, the structure of the magnetic reconnection is similar to the Petschek type. Four slow shocks stem from the diffusion region. The magnetic energy is converted to the plasma energy not only in the diffusion region but also at the shocks. Such structures are observed in non-relativistic MHD simulations (Scholer 1989; Yan et al. 1992; Yokoyama & Shibata 1994). The shock structure and the outflow velocity is consistent with the analytical model for the relativistic reconnection (Lyubarsky 2005).

Finally, we would like to discuss the energetic particle generation in the magnetic reconnection. Around the $X-$point, magnetic energy is converted into that of the electric fields. The electric field can accelerate particles. Such non-thermal particles have been observed in the earth magnetosphere (see, e.g., Christon et al. 1988). Larrabee et al. (2003) showed that the leptons are accelerated by the induced electric field. In their

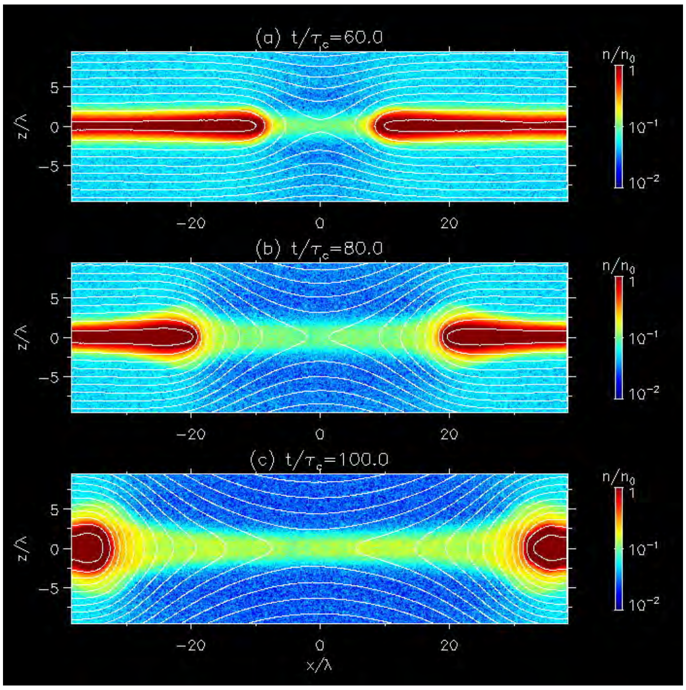

Figure 1.19: Relativistic magnetic reconnection by 2-D PIC simulation (Zenitani & Hoshino 2007). Color contours show the density, while the curves do the magnetic field lines.

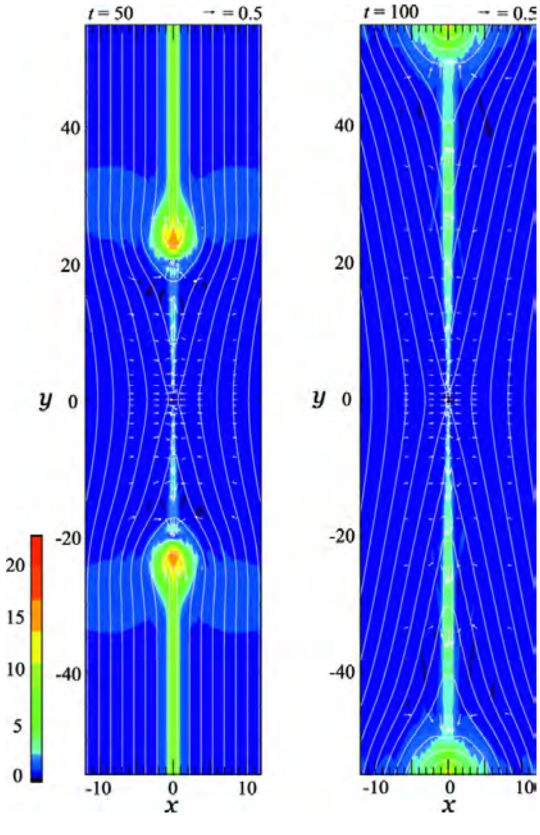

Figure 1.20: Relativistic magnetic reconnection by 2-D Relativistic Resistive MHD simulation (Watanabe & Yokoyama 2006). Color contours show the density, while the curves and arrows do the magnetic field lines and velocity fields, respectively.

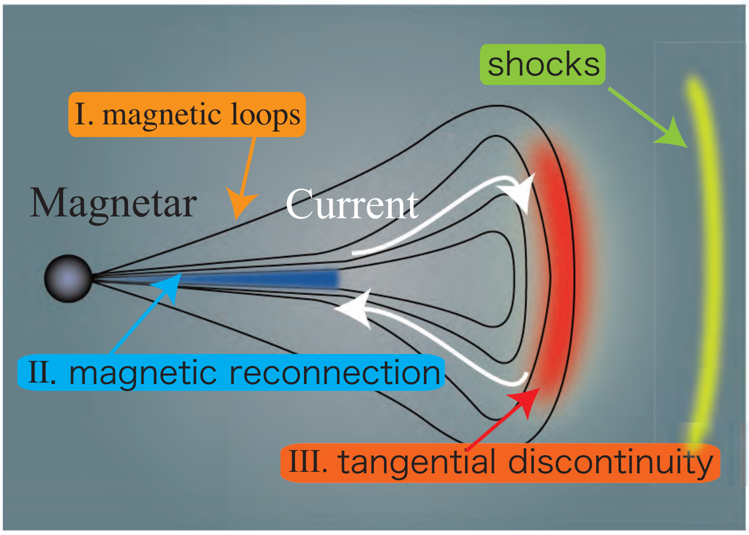

Figure 1.21: Schematic picture of the expanding magnetic loops. A current sheet is created inside the magnetic loops.

model, the particle energy spectra is approximately written as $dN/d\gamma \propto \exp(-\gamma/\gamma_0)/\gamma$, where γ_0 is the cutoff energy. Lyubarsky & Liverts (2008) performed 2-dimensional PIC simulations and confirmed that the particle energy spectra obeys the former function. Zenitani & Hoshino (2001) performed 2-dimensional PIC simulations and showed that the particle distribution function around the diffusion region can be fitted by power-law function with index of -1. The radiation from the accelerated particles can be responsible for the observed nonthermal spectra.

1.4 Purpose of This Paper

In this thesis, first, we derive self-similar solutions of relativistically expanding magnetic loops for the purpose of studying the dynamics of the expanding magnetic loops (chapter 2, region I in Fig. 1.21). Azimuthal magnetic fields are taken into account. We neglect stellar rotation and assume axisymmetry and a purely radial flow. The self-similar parameter depends on the radial distance r from the central star and the time t. The physical properties of the magnetic loops, such as the internal structure and the energetics are discussed.

In Chapter 3, we concentrate on the current sheet inside the magnetic loops (region II in Fig. 1.21) and study the relativistic magnetic reconnection by extending the Sweet-

Parker model. The treatment is based on the relativistic MHD. The magnetic fields are assumed to reconnect steadily in a small thin rectangular box named dissipation region. Applying the conservation laws of mass and energy to the dissipation region, we obtain the relation between the inflow and the outflow. In our model, we include the enthalpy decrease due to the expansion inside the dissipation region as well as the pressure gradient force. Then we derive the condition for the relativistic outflow from the magnetic reconnection.

Because the size of the dissipation region and the inflow velocity cannot be determined in MHD analysis, we perform 2-dimensional PIC simulations (chapter 4) to verify the analytic model discussed in Chapter 3. We assume collisionless and pair plasma. We show that the outflow velocity is smaller than the Alvén velocity of the inflow for the larger magnetic field energy, while the plasma pressure increases in proportion to the magnetic field energy.

Chapter 5 is devoted for summary and discussion.

Chapter 2

Relativistic Expansion of Magnetic Loops at the Self-similar Stage

Assuming relativistic force-free dynamics, Lyutikov & Blandford (2003) obtained self-similar solutions of the spherically expanding magnetic shell. Prendergast (2005) found self-similar solutions of the relativistic force-free field. In these studies of force-free dynamics, gas pressure and inertial terms are neglected. In the framework of the relativistic magnetohydrodynamics (MHD), Lyutikov (2002) found self-similar solutions of the spherically expanding magnetic shells. Low (1982) obtained non-relativistic self-similar MHD solutions of the expanding magnetic loops in solar flares or supernovae explosion by assuming axisymmetry. Subsequently, Low (1984) extended his model to the case including toroidal magnetic fields and applied it to solar coronal mass ejections (CMEs). The latter model was employed by Stone et al. (1992) as a test problem to check the validity and accuracy of axisymmetric MHD codes. In magnetar flares, the magnetic loops may be twisted by the shear motion at the footpoints of the loops. The shear motion generates Alfvén waves propagating along the field lines. Such twisted magnetic loops expand by the enhanced magnetic pressure by the toroidal magnetic fields. Thus we should include the toroidal magnetic field to study the evolution of magnetic loops during magnetar flares. Also the relativistic effects should be included. The characteristic wave speed in the magnetar magnetosphere approaches the light speed because of the strong magnetic fields. Thus our aim is to obtain relativistic self-similar MHD solutions of expanding magnetic loops taking into account the toroidal magnetic fields by extending the non-relativistic solutions found by Low (1982).

This chapter is organized as follows; in § 2.1, we present the relativistic ideal MHD equations and introduce a self-similar parameter which depends on both radial distance from the centre of the star and time. In § 2.2, we obtain self-similar solutions. The physical properties of these solutions are discussed in § 2.3. We summarize the results in § 2.4.

2.1 Self-similar MHD Equations

In the following, we take the light speed as unity. The complete set of relativistic ideal MHD equations is

$$\frac{\partial}{\partial t}(\gamma\rho) + \nabla\cdot(\gamma\rho\boldsymbol{v}) = 0, \tag{2.1.1}$$

$$\rho\gamma\left[\frac{\partial}{\partial t} + (\boldsymbol{v}\cdot\nabla)\right](\xi\gamma\boldsymbol{v}) = -\nabla p + \rho_e\boldsymbol{E} + \boldsymbol{j}\times\boldsymbol{B} - \frac{GM\rho\gamma}{r^2}\boldsymbol{e}_r, \tag{2.1.2}$$

$$\left[\frac{\partial}{\partial t} + (\boldsymbol{v}\cdot\nabla)\right]\left(\ln\frac{p}{\rho^\Gamma}\right) = 0, \tag{2.1.3}$$

$$\nabla\cdot\boldsymbol{E} = 4\pi\rho_e, \tag{2.1.4}$$

$$\nabla\cdot\boldsymbol{B} = 0, \tag{2.1.5}$$

$$\frac{\partial\boldsymbol{B}}{\partial t} + \nabla\times\boldsymbol{E} = 0, \tag{2.1.6}$$

$$\frac{\partial\boldsymbol{E}}{\partial t} = \nabla\times\boldsymbol{B} - 4\pi\boldsymbol{j}, \tag{2.1.7}$$

$$\boldsymbol{E} = -\boldsymbol{v}\times\boldsymbol{B}, \tag{2.1.8}$$

where $\boldsymbol{E}, \boldsymbol{B}, \boldsymbol{j}, \boldsymbol{v}, \gamma, \rho_e, \rho, p, \Gamma$ are the electric field, the magnetic field, the current density, the velocity, the Lorentz factor, the charge density, the mass density, the pressure and the specific heat ratio, respectively. The vector $\boldsymbol{e}_r$ is a unit vector in the radial direction. We include the gravity by a point mass M as an external force. Here G is the gravitational constant, and r is the distance from the centre of the star. The relativistic specific enthalpy ξ is defined as

$$\xi = \frac{\epsilon + p}{\rho} = 1 + \frac{\Gamma}{\Gamma - 1}\frac{p}{\rho}, \tag{2.1.9}$$

where ϵ is the energy density of matter including the photon energy coupled with the plasma. In SGR outbursts, since the luminosity much exceeds the Eddington luminosity, radiation energy density can exceed the thermal energy of the plasma. In the following pressure p includes the contribution from the radiation pressure.

In this chapter, we consider relativistic self-similar expansions of magnetic loops which started expansion at $t = t_{\rm s}$ by loss of dynamical equilibrium and entered into a self-similar stage at $t = t_0 > t_{\rm s}$. We do not consider the evolution of the loops before $t = t_0$.

For simplicity, we ignore the stellar rotation and assume axisymmetry. We can express the axisymmetric magnetic field in terms of two scalar functions $\tilde{A}$ and B as

$$\boldsymbol{B} = \frac{1}{r\sin\theta}\left(\frac{1}{r}\frac{\partial\tilde{A}}{\partial\theta}, -\frac{\partial\tilde{A}}{\partial r}, B\right), \tag{2.1.10}$$

in the polar coordinates (r, θ, ϕ). The scalar function $\tilde{A}(t, r, \theta)$, which corresponds to the vector potential, denotes the magnetic flux. The contours of $\tilde{A}$ coincide with magnetic field lines projected on to the $r - \theta$ plane.

We further assume that the fluid flow is purely radial;

$$\boldsymbol{v} = v(t, r, \theta)\,\boldsymbol{e}_r. \tag{2.1.11}$$

Equations (2.1.1), (2.1.2), (2.1.3), and (2.1.6) are then expressed as

$$\frac{\partial(\rho\gamma)}{\partial t} + \frac{1}{r^2}\frac{\partial(r^2\rho\gamma v)}{\partial r} = 0, \tag{2.1.12}$$

$$\begin{aligned}\rho\gamma\left[\frac{\partial}{\partial t} + v\frac{\partial}{\partial r}\right](\xi\gamma v) = &-\frac{\partial p}{\partial r} - \frac{GM\rho\gamma}{r^2} \\ &- \frac{1}{4\pi r^2\sin^2\theta}\left\{\frac{\partial\tilde{A}}{\partial r}\left[\left(\hat{\mathcal{L}}_{(r,\theta)}\tilde{A}\right) + \frac{\partial}{\partial t}\left(v\frac{\partial\tilde{A}}{\partial r}\right)\right] + B\left[\frac{\partial B}{\partial r} + \frac{\partial(vB)}{\partial t}\right]\right\},\end{aligned} \tag{2.1.13}$$

$$4\pi r^2\sin^2\theta\frac{\partial p}{\partial\theta} + (1 - v^2)B\frac{\partial B}{\partial\theta} + \frac{\partial\tilde{A}}{\partial\theta}\left[\left(\hat{\mathcal{L}}_{(r,\theta)}\tilde{A}\right) + \frac{\partial}{\partial t}\left(v\frac{\partial\tilde{A}}{\partial r}\right)\right] - vB^2\frac{\partial v}{\partial\theta} = 0, \tag{2.1.14}$$

$$(1 - v^2)\frac{\partial\tilde{A}}{\partial r}\frac{\partial B}{\partial\theta} - \frac{\partial\tilde{A}}{\partial\theta}\left[\frac{\partial B}{\partial r} + \frac{\partial(vB)}{\partial t}\right] - vB\frac{\partial\tilde{A}}{\partial r}\frac{\partial v}{\partial\theta} = 0, \tag{2.1.15}$$

$$\left[\frac{\partial}{\partial t} + v\frac{\partial}{\partial r}\right]\left(\ln\frac{p}{\rho^\Gamma}\right) = 0, \tag{2.1.16}$$

$$\frac{\partial\tilde{A}}{\partial t} + v\frac{\partial\tilde{A}}{\partial r} = 0, \tag{2.1.17}$$

$$\frac{\partial B}{\partial t} + \frac{\partial(vB)}{\partial r} = 0, \tag{2.1.18}$$

where we used the MHD condition given by (2.1.8) and introduced the operator

$$\hat{\mathcal{L}}_{(r,\theta)} \equiv \frac{\partial^2}{\partial r^2} + \frac{\sin\theta}{r^2}\frac{\partial}{\partial\theta}\left(\frac{1}{\sin\theta}\frac{\partial}{\partial\theta}\right). \tag{2.1.19}$$

Since our aim is to obtain self-similar solutions of these relativistic MHD equations, we assume that the time evolution is governed by the self-similar variable:

$$\eta = \frac{r}{Z(t)}, \tag{2.1.20}$$

where $Z(t)$ is an arbitrary function of time. We further assume that the flux function $\tilde{A}$ depends on time t and the radial distance r through the self-similar variable η, as

$$\tilde{A}(t,r,\theta) = \tilde{A}(\eta,\theta). \tag{2.1.21}$$

When equation (2.1.21) is satisfied, the radial velocity v has a form

$$v = \eta \dot{Z}, \tag{2.1.22}$$

from equation (2.1.17). Here dot denotes the time derivative. Equation (2.1.22) implies that the radial velocity v does not depend on the polar angle θ. It then follows from equations (2.1.12) and (2.1.18) that

$$\rho(t,r,\theta)\gamma(t,r) = Z^{-3}(t)D(\eta,\theta), \tag{2.1.23}$$

$$B(t,r,\theta) = Z^{-1}(t)Q(\eta,\theta), \tag{2.1.24}$$

where Q and D are arbitrary functions of η and θ. These relations indicate that the magnetic flux and the total mass are conserved. Next we take the pressure p as $p(t,r,\theta) = Z^l P(\eta,\theta)$. Substituting this equation into equations (2.1.14) and (2.1.16), we obtain

$$\begin{aligned} 4\pi\eta^2 Z^{l+4} \sin^2\theta \frac{\partial P}{\partial \theta} &+ (1-\eta^2\dot{Z}^2) Q \frac{\partial Q}{\partial \theta} \\ &+ \frac{\partial \tilde{A}}{\partial \theta}\left[\hat{\mathcal{L}}_{(\eta,\theta)}\tilde{A} + \left(\eta Z\ddot{Z} - 2\eta\dot{Z}^2\right)\frac{\partial \tilde{A}}{\partial \eta} - \eta^2\dot{Z}^2\frac{\partial^2 \tilde{A}}{\partial \eta^2}\right] = 0, \end{aligned} \tag{2.1.25}$$

$$\frac{\Gamma\eta^2 Z\ddot{Z}}{1-\eta^2\dot{Z}^2} + (3\Gamma + l) = 0, \tag{2.1.26}$$

where we introduced an operator $\hat{\mathcal{L}}_{(\eta,\theta)}$:

$$\hat{\mathcal{L}}_{(\eta,\theta)} \equiv \frac{\partial^2}{\partial \eta^2} + \frac{\sin\theta}{\eta^2}\frac{\partial}{\partial\theta}\left(\frac{1}{\sin\theta}\frac{\partial}{\partial\theta}\right) = \frac{1}{Z^2}\hat{\mathcal{L}}_{(r,\theta)}. \tag{2.1.27}$$

To satisfy these equations, p, Z and Γ should have forms

$$p(t,r,\theta) = Z^{-4}P(\eta,\theta), \tag{2.1.28}$$

$$Z(t) = t, \tag{2.1.29}$$

and

$$\Gamma = \frac{4}{3}. \tag{2.1.30}$$

This adiabatic index corresponds to the radiation pressure dominant plasma. Thus our model can describe the evolution of a fireball confined by magnetic fields.

Equations (2.1.23) and (2.1.28) indicate that the magnetic loops expand adiabatically. By using equations (2.1.22), (2.1.23), (2.1.24), (2.1.28), (2.1.29) and (2.1.30), equations (2.1.13), (2.1.15) and (2.1.25) are expressed as

$$\begin{aligned} D(\eta,\theta) = \frac{\eta^2}{GM}\Bigg\{ &\frac{4\eta P}{1-\eta^2} - \frac{\partial P}{\partial \eta} \\ &-\frac{1}{4\pi\eta^2\sin^2\theta}\left[\frac{\partial \tilde{A}}{\partial \eta}\left(\hat{\mathcal{L}}_{(\eta,\theta)}\tilde{A} - \frac{\partial}{\partial \eta}\left(\eta^2\frac{\partial \tilde{A}}{\partial \eta}\right)\right) + Q\frac{\partial}{\partial \eta}\left(Q(1-\eta^2)\right)\right]\Bigg\}, \end{aligned} \tag{2.1.31}$$

$$(1-\eta^2)\frac{\partial \tilde{A}}{\partial \eta}\frac{\partial Q}{\partial \theta} - \frac{\partial \tilde{A}}{\partial \theta}\frac{\partial}{\partial \eta}\left[(1-\eta^2)Q\right] = 0, \tag{2.1.32}$$

$$4\pi\eta^2\sin^2\theta\frac{\partial P}{\partial \theta} + \frac{\partial \tilde{A}}{\partial \theta}\left[\hat{\mathcal{L}}_{(\eta,\theta)}\tilde{A} - \frac{\partial}{\partial \eta}\left(\eta^2\frac{\partial \tilde{A}}{\partial \eta}\right)\right] + (1-\eta^2)Q\frac{\partial Q}{\partial \theta} = 0. \tag{2.1.33}$$

From equation (2.1.32), a formal solution of Q is obtained as

$$Q(\eta,\theta) = \frac{\mathcal{G}(\tilde{A})}{1-\eta^2}, \tag{2.1.34}$$

where $\mathcal{G}$ is an arbitrary function.

Self-similar solutions can be constructed as follows. First we prescribe an arbitrary function $\tilde{A}(\eta,\theta)$ (or $Q(\eta,\theta)$). Then, equation (2.1.32) determines the function $Q(\eta,\theta)$ (or $\tilde{A}(\eta,\theta)$). Functions $\tilde{A}$ and Q determine the pressure $P(\eta,\theta)$ according to equation (2.1.33). Finally, the density function $D(\eta,\theta)$ is obtained by equation (2.1.31).

Note that from the equation (2.1.22) and (2.1.29), the radial velocity has a simple form as

$$v = \frac{r}{t}. \tag{2.1.35}$$

Since the time derivative of the velocity becomes zero, i.e., $D\boldsymbol{v}/Dt = 0$, equations (2.1.31)-(2.1.33) describe the freely expanding solution. This means that there is a reference frame that all forces balance. By substituting equations (2.1.23), (2.1.24), (2.1.28), (2.1.29), and (2.1.35) into the equations of motion (2.1.2), we obtain

$$\frac{\Gamma}{\Gamma-1}\frac{\gamma^2 v^2 p}{r}\boldsymbol{e}_r - \nabla p + \rho_e \boldsymbol{E} + \boldsymbol{j}\times\boldsymbol{B} - \frac{GM\rho\gamma}{r^2}\boldsymbol{e}_r = 0. \tag{2.1.36}$$

The first term on the left hand side comes from the inertia. For convenience, we call this term as a thermal inertial term throughout this chapter. When we neglect the terms of order $(v/c)^2$, equation (2.1.36) reduces to the equations of the force balance in non-relativistic MHD.

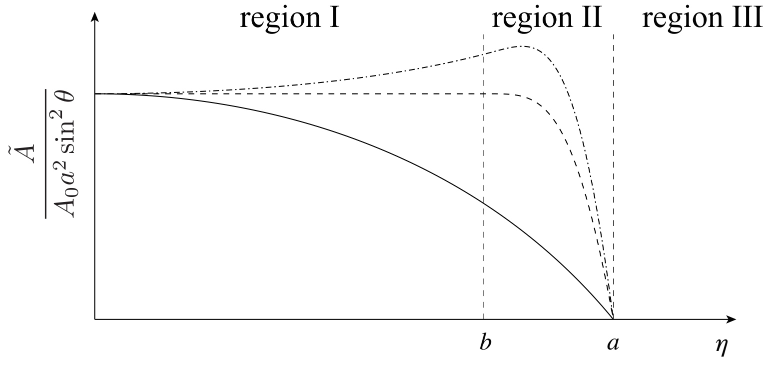

Figure 2.1: The flux function $\tilde{A}$ as a function of η for the dipolar solution (solid curve), the shell solution (dashed curve), and the flux rope solution (dot-dashed curve). The parameters a and b denote the outer and inner boundaries of the shell, respectively.

2.2 Self-similar solutions

In the previous section, we derived relativistic self-similar MHD equations, (2.1.31), (2.1.32) and (2.1.33). In this section, we obtain solutions of these equations by imposing appropriate boundary conditions. As mentioned in the previous section, the toroidal magnetic field, the pressure, and the gas density are calculated by assigning the flux function $\tilde{A}(\eta, \theta)$. In the following, we introduce three kinds of flux functions and obtain explicit forms of other variables.

2.2.1 Construction of Solutions

We assume that the expanding magnetic loops have a spherical outer boundary at $r = R(t)$.

A simple solution of the expanding magnetic loops is that the poloidal magnetic field is dipolar near the surface of the star (Low 1982). The magnetic field should be tangential to the spherical surface $r = R(t)$ at all time. Such a solution can be constructed by

$$\tilde{A}(\eta, \theta) = A_0 \frac{a^2 - \eta^2}{\sqrt{1-\eta^2}} \sin^2\theta, \tag{2.2.1}$$

where A_0 and a are constants. The radius $R(t)$ where $\tilde{A} = 0$ is given by

$$R(t) = at. \tag{2.2.2}$$

We hereafter call the solution constructed from equation (2.2.1) as *dipolar solution.*

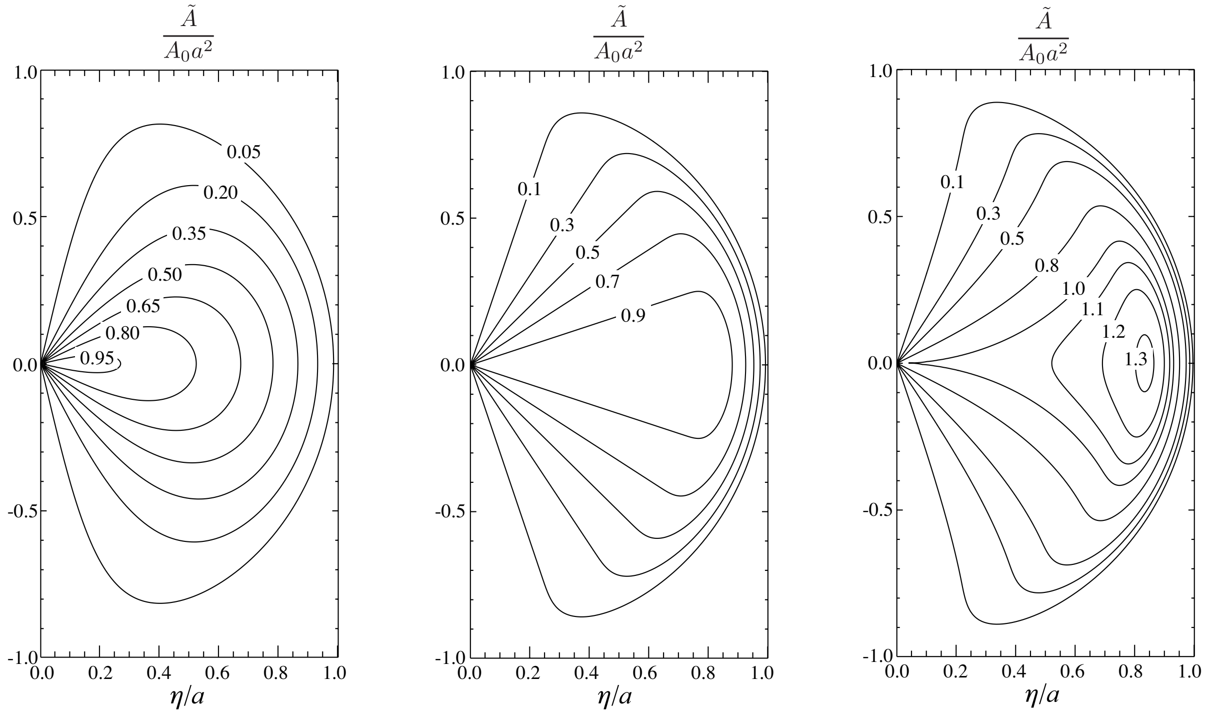

Figure 2.2: Contour plots of the magnetic flux $\tilde{A}$ which constructs the dipolar, shell, and flux rope solutions from left to right, respectively. The parameters are taken as $a = 0.8$, $b/a = 0.7$, and $k = \pi/[4(a-b)]$.

Solid curve in Fig. 2.1 shows the flux function $\tilde{A}$ as a function of η for the dipolar solution. Contour plots of $\tilde{A}$ for dipolar solution is shown in the left panel of Fig. 2.2.

When the flux function is given by equation (2.2.1), the magnetic flux crossing the annulus at the equatorial plane $\theta = \pi/2$ decreases with radius (see Fig. 2.1). In actual MHD explosion, the magnetic flux can be swept up into a thin shell just behind the loop top. The shell boundaries are assumed to be at $r = bt$ and $r = at$ (region II, see Fig. 2.1). Such a self-similar field can be constructed by

$$\tilde{A}(\eta,\theta) = \begin{cases} A_0 a^2 \sin^2\theta, & (\text{region I} : \eta \leqq b), \\ A_0 a^2 \Lambda(\eta)\sin^2\theta, & (\text{region II} : b < \eta \leqq a), \end{cases} \tag{2.2.3}$$

where

$$\Lambda(\eta) = 1 - \frac{\sin^4 T(\eta)}{\sin^4 T(a)}, \tag{2.2.4}$$

$$T(\eta) = k(\eta - b), \tag{2.2.5}$$

and a, b and k are constants (Low 1982). The flux functions in region I ($\eta \leqq b$) and region II ($b < \eta \leqq a$) are connected smoothly at $\eta = b$. The loop boundary locates at $r = at$, where $\tilde{A} = 0$.

The flux function for this solution is shown by a dashed curve in Fig. 2.1. It can be easily shown that the magnetic field lines projected on to the $r-\theta$ plane are all radial in region I. We call the solution constructed from equation (2.2.3) as *shell solution.* The middle panel of Fig. 2.2 shows the contours of $\tilde{A}$ for the shell solution.

Another solution is that we call *flux rope solution.* As the magnetic loops expand, a current sheet is formed inside the magnetic loops. It is suggested that the magnetic reconnection taking place in the current sheet is responsible for the SGR flares (Woods et al. 2001; Lyutikov 2006). When the magnetic reconnection takes place, flux ropes (namely plasmoids) are formed inside magnetic loops. The flux function should then have a local maximum inside the flux rope. Such a solution can be constructed by

$$\tilde{A}(\eta,\theta) = \begin{cases} \dfrac{A_0 a^2}{\sqrt{1-\eta^2}} \sin^2\theta, & (\text{region I} : \eta \leqq b), \\ \dfrac{A_0 a^2}{\sqrt{1-\eta^2}} \Lambda(\eta) \sin^2\theta, & (\text{region II} : b < \eta \leqq a), \end{cases} \tag{2.2.6}$$

where A_0, a are constants and $\Lambda(\eta)$ is given by equation (2.2.4). This function is shown by a dot-dashed curve in Fig. 2.1. It has a local maximum in the domain $b < \eta < a$ (see Fig. 2.1). The contours of $\tilde{A}$ for the flux rope solution is shown in the right panel of Fig. 2.2. Flux ropes appear behind the shell.

2.2.2 Dipolar Solutions

Dipolar solutions are constructed by the flux function specified by equation (2.2.1). The azimuthal magnetic fields can be obtained by substituting equation (2.2.1) into equation (2.1.32) as

$$Q(\eta,\theta) = \sum_n Q_{0,n} \frac{(a^2-\eta^2)^{\frac{n}{2}}}{(1-\eta^2)^{1+\frac{n}{4}}} \sin^n\theta, \tag{2.2.7}$$

where $Q_{0,n}$ are constants. Note that the solutions (2.2.1) and (2.2.7) satisfy the formal solution given by equation (2.1.34). Substituting equations (2.2.1) and (2.2.7) into equation (2.1.33), we obtain the pressure function P:

$$P(\eta,\theta) = P_0(\eta) + P_A(\eta,\theta) + P_Q(\eta,\theta), \tag{2.2.8}$$

where $P_0(\eta)$ is an arbitrary function arisen from the integration and P_A and P_Q are given by

$$P_A(\eta,\theta) = \frac{A_0^2}{4\pi\eta^4} \frac{a^2-\eta^2}{(1-\eta^2)^2} (2a^2 - 3a^2\eta^2 - \eta^4 + 2\eta^6) \sin^2\theta, \tag{2.2.9}$$

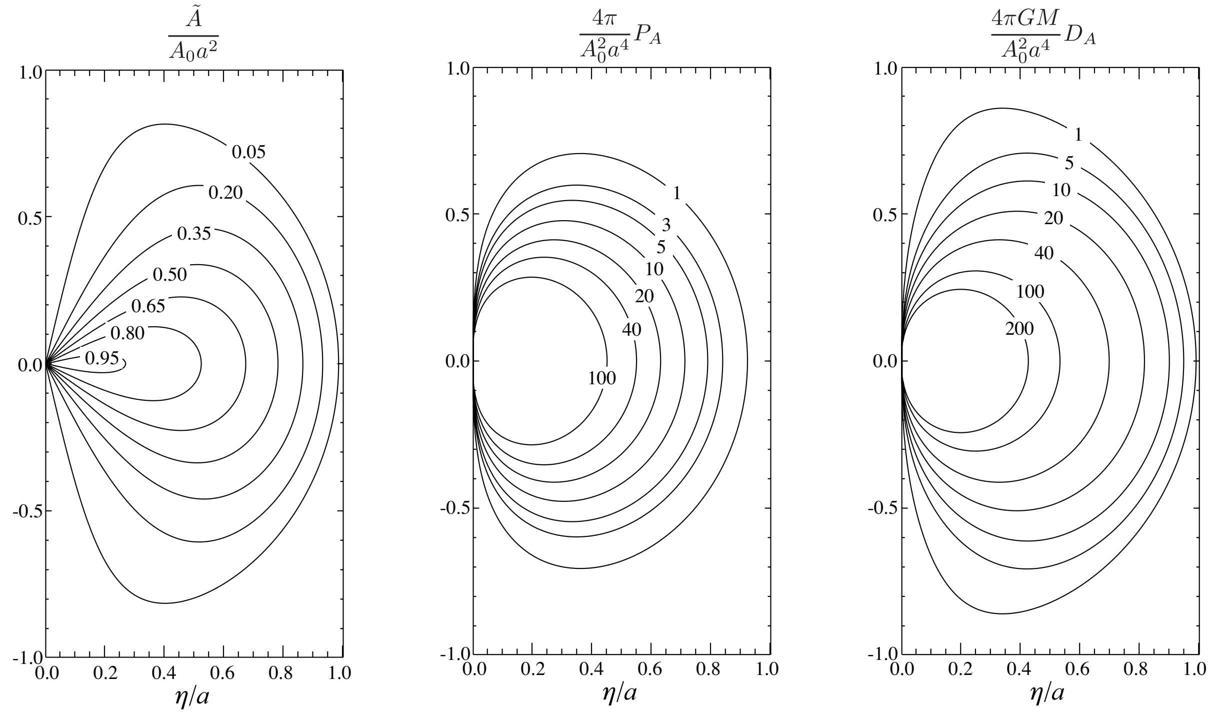

Figure 2.3: Contour plots of the magnetic flux $\tilde{A}$ (left), the poloidal part of the pressure P_A (centre), and that of the gas density D_A(right) for the dipolar solution in $\eta/a - \theta$ plane when $a = 0.8$.

$$P_Q(\eta,\theta) \;=\; \begin{cases} -\displaystyle\sum_{m+n\neq 2} \frac{nQ_{0,m}Q_{0,n}}{4\pi(m+n-2)} \frac{(a^2-\eta^2)^{\frac{m+n}{2}}}{\eta^2(1-\eta^2)^{1+\frac{m+n}{4}}} \sin^{m+n-2}\theta, & \text{for} \quad m+n \neq 2, \\ -\displaystyle\sum_{m+n=2} \frac{nQ_{0,m}Q_{0,n}}{4\pi} \frac{a^2-\eta^2}{\eta^2(1-\eta^2)^{\frac{3}{2}}} \log(\sin\theta), & \text{for} \quad m+n = 2. \end{cases} \tag{2.2.10}$$

Substituting equations (2.2.1), (2.2.7), (2.2.8), (2.2.9), and (2.2.10) into (2.1.31), the density function D can be determined as

$$D(\eta,\theta) = D_0(\eta) + D_A(\eta,\theta) + D_Q(\eta,\theta), \tag{2.2.11}$$

where

$$D_0(\eta) = \frac{\eta^2}{GM}\left(\frac{4\eta P_0}{1-\eta^2} - \frac{dP_0}{d\eta}\right), \tag{2.2.12}$$

$$D_A(\eta,\theta) = \frac{A_0^2}{4\pi GM\eta^3}\frac{(a^2-\eta^2)}{(1-\eta^2)^3}\left[a^2(8-12\eta^2+3\eta^4) - \eta^6(5-6\eta^2)\right]\sin^2\theta, \tag{2.2.13}$$

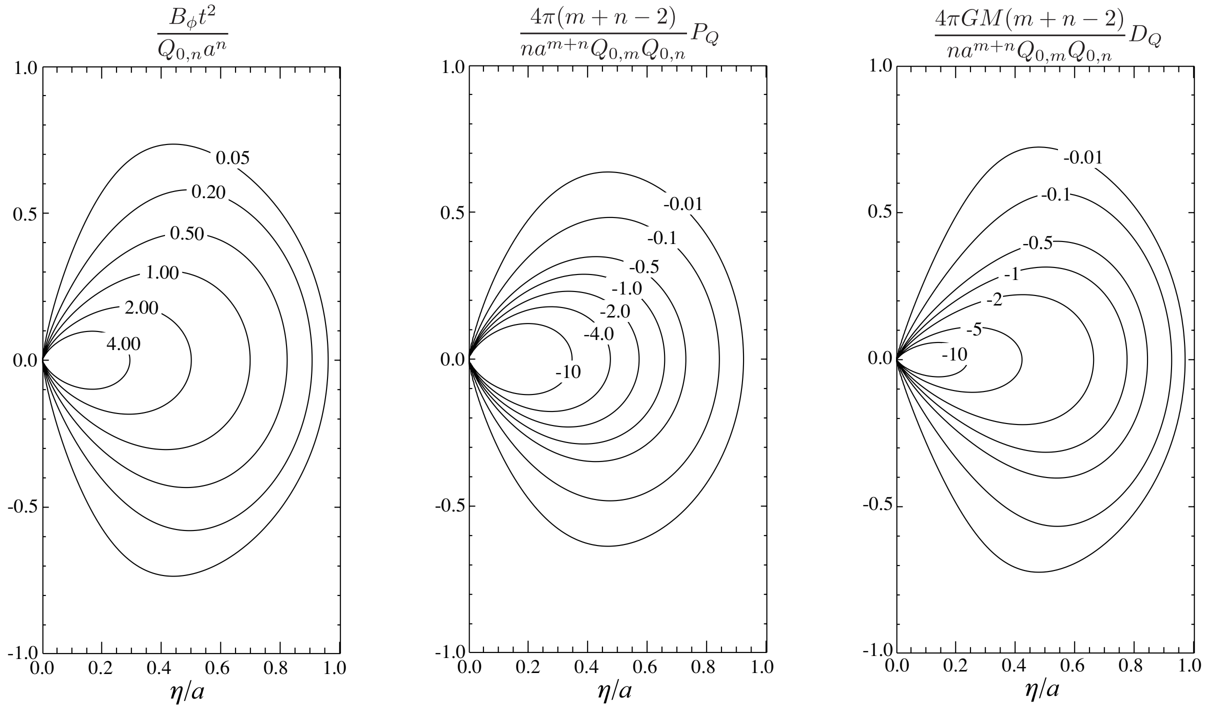

Figure 2.4: Contour plots of the toroidal magnetic field (left), the toroidal part of the pressure P_Q (centre), and that of the density D_Q(right) for the dipolar solution in $\eta/a-\theta$ plane when $a=0.8$ and $m=n=4$.

$$D_Q(\eta,\theta)=\begin{cases} -\displaystyle\sum_{m+n\neq 2}\frac{nQ_{0,m}Q_{0,n}}{4\pi GM(m+n-2)}\frac{(a^2-\eta^2)^{\frac{m+n-2}{2}}(2a^2-a^2\eta^2-\eta^4)}{\eta(1-\eta^2)^{2+\frac{m+n}{4}}}\sin^{(m+n-2)}\theta, \\ \hfill \text{for}\quad m+n\neq 2, \\ -\displaystyle\sum_{m+n=2}\frac{nQ_{0,m}Q_{0,n}}{8\pi GM}\frac{-\eta^2(2-a^2-\eta^2)+2(2a^2-a^2\eta^2-\eta^4)\log(\sin\theta)}{\eta(1-\eta^2)^{\frac{5}{2}}}, \\ \hfill \text{for}\quad m+n=2. \end{cases} \tag{2.2.14}$$

The parameters m and n correspond to the Fourier modes in the θ direction. These parameters should be determined by the boundary condition on the surface of the central star where magnetic twist is injected.

Equation (2.2.8) and (2.2.11) indicate that the solution consists of three parts, P_0, P_A and P_Q (or D_0, D_A and D_Q). The arbitrary function $P_0(\eta)$ describes an isotropic pressure in the region $r<R(t)$. The isotropic density profile $D_0(\eta)$ is related to P_0 through equation (2.2.12). This equation is similar to that in non-relativistic model (Low 1982). In the non-relativistic model, gravity is supported by the gradient of $P_0(\eta)$. In the relativistic case, relativistic correction of the plasma inertia cannot be ignored. This effect is included in the first term in the right hand side of equation (2.2.12). Other functions P_A

and P_Q (or D_A and D_Q) come from the interaction with the electromagnetic force. Note that the plasma pressure P_Q, which balances with the electromagnetic force produced by the toroidal magnetic field, is always negative. This suggests that the pressure is smaller for larger toroidal magnetic fields.

Fig. 2.3 shows the contour plots of the magnetic flux $\tilde{A}$ (left), the poloidal part of the pressure P_A (centre), and that of the gas density D_A (right), while Fig. 2.4 shows the contour plots of the toroidal magnetic field B_ϕ (left), the toroidal part of the pressure P_Q (centre), and that of the gas density D_Q (right) in the $\eta/a - \theta$ plane for $m = n = 4$ and $a = 0.8$.

The magnetic field is explicitly expressed as

$$\begin{aligned} B_r &= \frac{2A_0}{r^2} \frac{a^2 - (r/t)^2}{\sqrt{1 - (r/t)^2}} \cos\theta, && (2.2.15) \\ B_\theta &= \frac{A_0}{t^2} \frac{2 - a^2 - (r/t)^2}{[1 - (r/t)^2]^{\frac{3}{2}}} \sin\theta, && (2.2.16) \\ B_\phi &= \sum_n \frac{Q_{0,n}}{rt} \frac{[a^2 - (r/t)^2]^{\frac{n}{2}}}{[1 - (r/t)^2]^{1+\frac{n}{4}}} \sin^{n-1}\theta \boldsymbol{e}_\phi, && (2.2.17) \end{aligned}$$

where $\boldsymbol{e}_r$, $\boldsymbol{e}_\theta$, and $\boldsymbol{e}_\phi$ are unit vectors in r, θ, and ϕ directions in the polar coordinate, respectively. Note that B_r and B_ϕ are zero at $r = R(t)$ but B_θ is not zero and it depends on time when $a \neq 1$. We will discuss the physical meaning of this result later in §2.2.3.

In later stage, the magnetic field becomes stationary,

$$\lim_{t\to\infty} \boldsymbol{B} = \frac{2A_0 a^2}{r^2} \cos\theta \boldsymbol{e}_r, \tag{2.2.18}$$

and the magnetic field becomes radial. In the limit $t \gg r$, the pressure and the gas density inside the magnetic loop are given by

$$\lim_{t\to\infty} p = \frac{A_0^2 a^4}{2\pi r^4} \sin^2\theta + \frac{1}{r^4} \left(P_0 \eta^4\right)\big|_{\eta=0}, \tag{2.2.19}$$

$$\lim_{t\to\infty} \rho = \frac{2A_0^2 a^4}{\pi G M r^3} \sin^2\theta + \frac{1}{r^3} \left(D_0 \eta^3\right)\big|_{\eta=0}. \tag{2.2.20}$$

Since the toroidal magnetic field tends to be zero in this limit, the pressure and density do not depend on the amplitude of the toroidal magnetic fields.

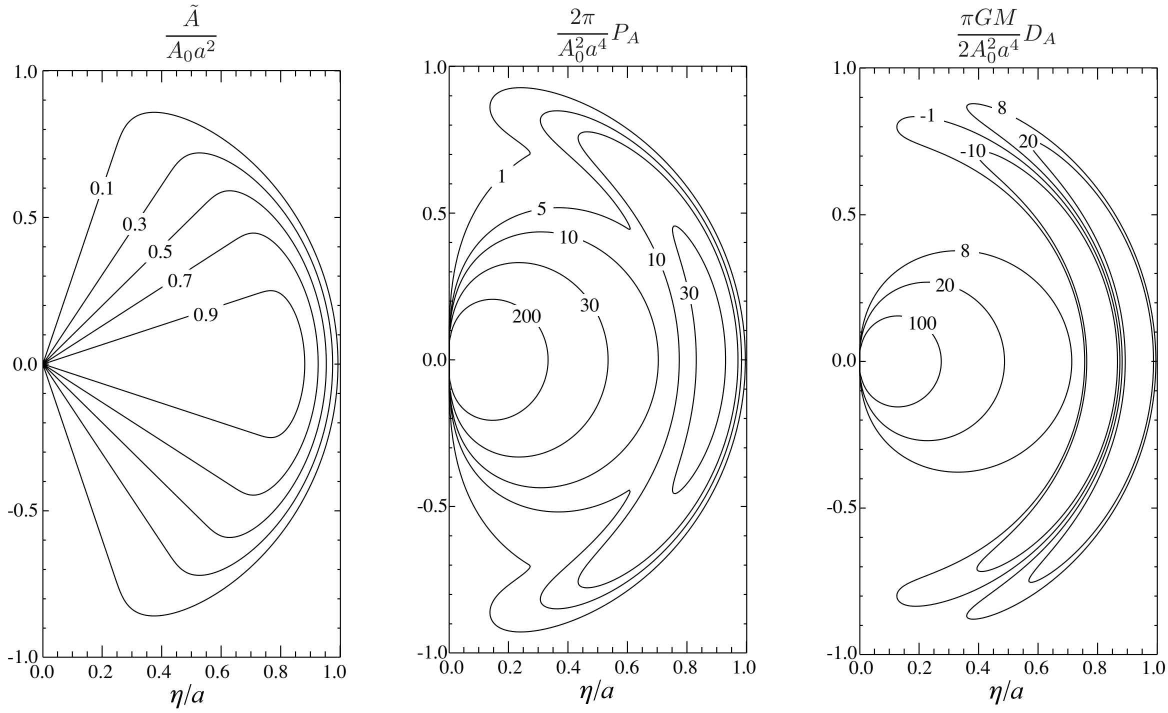

Figure 2.5: Contour plots of the magnetic flux $\tilde{A}$ (left), the poloidal part of the pressure P_A (centre), and that of the gas density D_A (right) for the shell solution in $\eta/a - \theta$ plane when $a = 0.8$ and $b = 0.75a$.

2.2.3 Shell Solutions

Shell solutions are constructed from the flux function (2.2.3). By substituting equation (2.2.3) into equation (2.1.32), the function Q can be obtained as

$$Q^I(\eta, \theta) = Q_0^I \frac{f(\theta)}{1 - \eta^2}, \tag{2.2.21}$$

$$Q^{II}(\eta, \theta) = \sum_n \frac{Q_{0,n}^{II}}{1 - \eta^2} \left[\sin^4 T(a) - \sin^4 T(\eta)\right]^{\frac{n}{2}} \sin^n \theta, \tag{2.2.22}$$

where $f(\theta)$ is an arbitrary function of θ, and Q_0^I and $Q_{0,n}^{II}$ are constants. The subscripts I and II mean that the function is defined in region I and in region II, respectively. The arbitrary function $f(\theta)$ can be determined by applying the boundary condition that magnetic field should be connected smoothly at $\eta = b$,

$$Q^I(\eta = b, \theta) = Q^{II}(\eta = b, \theta). \tag{2.2.23}$$

By using the boundary condition, the function f is given by

$$f(\theta) = \sum_n \sin^n \theta. \tag{2.2.24}$$

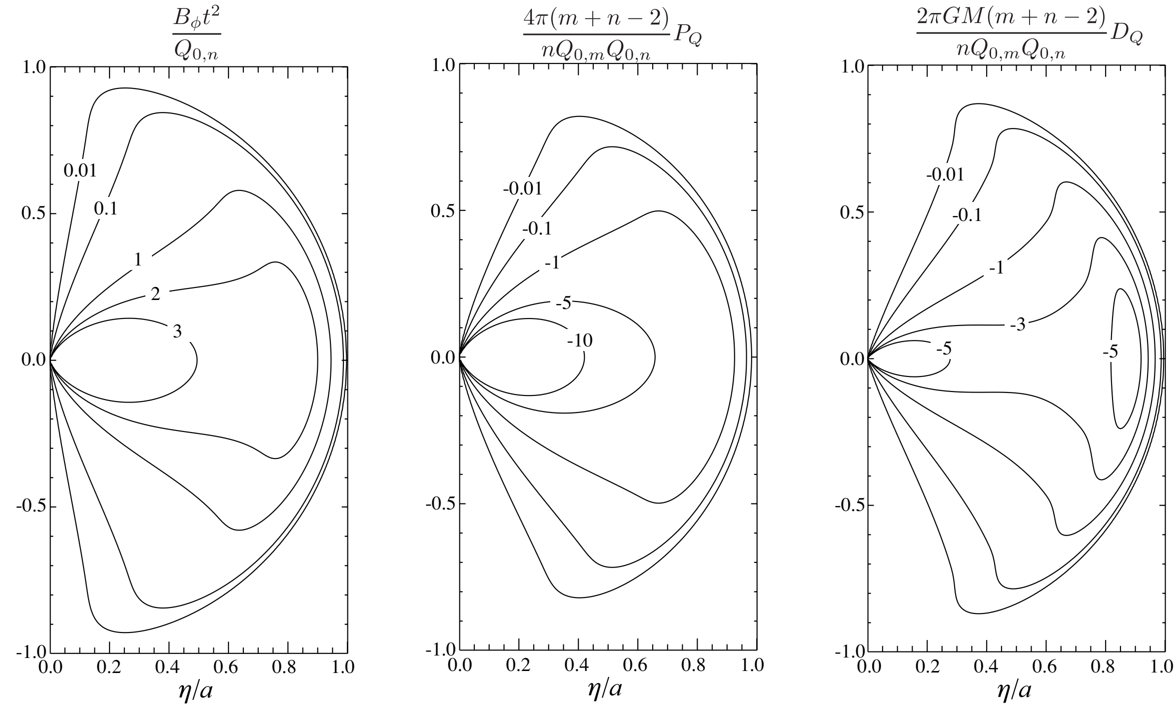

Figure 2.6: Contour plots of the toroidal magnetic field B_ϕ (left), the toroidal part of the pressure P_Q (centre), and that of the gas density D_Q (right) for the shell solution in $\eta/a-\theta$ plane when $a=0.8, b=0.75a$, and $n=m=4$.

and the function Q^I is obtained as

$$Q^I(\eta,\theta)=\sum_n Q^I_{0,n}\frac{\sin^n\theta}{1-\eta^2}. \tag{2.2.25}$$

The constants $Q^I_{0,n}$ and $Q^{II}_{0,n}$ should be related by

$$Q_{0,n}\equiv Q^I_{0,n}=Q^{II}_{0,n}\sin^{2n}T(a). \tag{2.2.26}$$

from the boundary condition (2.2.23). Substituting equations (2.2.3), (2.2.22), (2.2.25) and (2.2.26) into equation (2.1.33), we obtain the pressure function $P(\eta,\theta)$. The density function $D(\eta,\theta)$ is obtained from equation (2.1.31). The functions Q, P, and D obtained in region I and region II are given in appendix B.1.

The pressure and the gas density consist of three parts, the isotropic part P_0 and parts representing the interaction with the electromagnetic force by the poloidal and toroidal components of the magnetic field, P_A and P_Q, similarly to the dipolar solutions (see equations (B.1.2) and (B.1.9), for the pressure and equations (B.1.5) and (B.1.13) for the gas density).

Fig. 2.5 shows the contour plots of the magnetic flux $\tilde{A}$ (left), the poloidal part of the pressure P_A (centre), and that of the gas density D_A (right) in $\eta/a-\theta$ plane. Fig. 2.6 shows

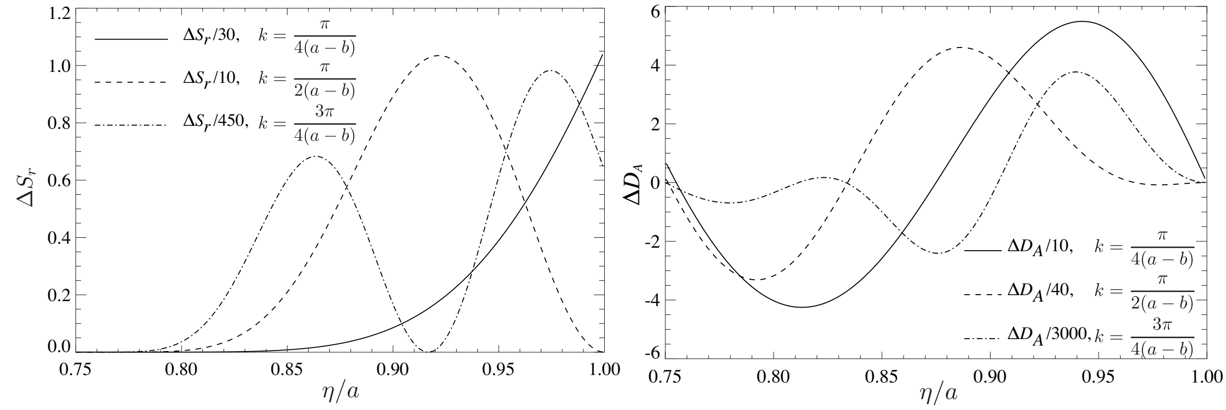

Figure 2.7: Distributions of the Poynting flux $\Delta S_r \equiv \pi r^4 S_r/(A_0^2 a^4 \sin^2\theta)$ (left) and $\Delta D_A \equiv D_A \pi G M \eta^3(1-\eta^2)/[2A_0^2 a^4 \sin^2\theta]$ (right) for the shell solutions, where $\boldsymbol{S}_r$ is the Poynting flux in the radial direction. Solid curves show for $k=\pi/[4(a-b)]$, while dashed and dot-dashed ones for $k=\pi/[2(a-b)]$, and $k=3\pi/[4(a-b)]$, respectively. Here we take $Q_{0,n}=0$.

contour plots of the toroidal magnetic field B_ϕ (left), the toroidal part of the pressure P_Q (centre), and that of the gas density D_Q (right) in $\eta/a-\theta$ plane. The parameters are taken to be $a=0.8$, $b=0.75a$, and $m=n=4$ in both figures. A shell structure appears behind the loop top.

The pressure P_Q is always negative (see equations (B.1.4) and (B.1.11) and the middle panel of Fig. 2.6) and its amplitudes is proportional to that of the toroidal magnetic fields, $Q_{0,n}$. This indicates that the pressure is smaller for a larger toroidal magnetic field.

The magnetic field is explicitly given by

$$B_r^I = \frac{2A_0a^2}{r^2}\cos\theta, \tag{2.2.27}$$

$$B_\phi^I = \sum_n Q_{0,n}\frac{t}{r(t^2-r^2)}\sin^{n-1}\theta, \tag{2.2.28}$$

$$B_r^{II} = \frac{2A_0a^2}{r^2}\Lambda\left(r/t\right)\cos\theta, \tag{2.2.29}$$

$$B_\theta^{II} = \frac{4A_0a^2}{rt}k\frac{\sin^3 T(r/t)\cos T(r/t)}{\sin^4 T(a)}\sin\theta, \tag{2.2.30}$$

$$B_\phi^{II} = \sum_n Q_{0,n}\Lambda^{\frac{n}{2}}\left(r/t\right)\frac{t\sin^{n-1}\theta}{r(t^2-r^2)}. \tag{2.2.31}$$

Similarly to the dipolar solution, the shell solutions have the parameter m which corresponds to the Fourier modes in the polar angle θ. These modes and the corresponding amplitude $Q_{0,m}$ of the toroidal magnetic fields should be determined by the boundary condition at the surface of the central star where the magnetic twist is injected.

In contrast to the dipolar solution, the magnetic field lines do not cross the equatorial plane in region I (see the left panel in Fig. 2.5). Note that in the limit that $t \gg r$, the magnetic fields and plasma distribution approach those of the dipolar solution, given by (2.2.18), (2.2.19) and (2.2.20).

At the boundary $r = R(t)$, the field components B_r and B_ϕ are exactly zero, but B_θ is not zero. Since the Poynting flux $\boldsymbol{S} = (\boldsymbol{E} \times \boldsymbol{B})/(4\pi)$ is not zero at $r = R(t)$, the energy flux will be transmitted to the region outside the boundary at $r = R(t)$. When $\cos T(a) = 0$, since the magnetic field vanishes at $r = R(t)$, the energy is not transferred to $r > R(t)$. This happens when the constant k is given by

$$k = \frac{(2l+1)}{2} \frac{\pi}{a-b}, \tag{2.2.32}$$

where l is an integer number.

Fig. 2.7 shows the distributions of the Poynting flux $\Delta S_r = r^4 \pi S_r/(A_0^2 a^4 \sin^2\theta)$ (left panel) and $\Delta D_A \equiv D_A \pi G M \eta^3 (1-\eta^2)/[2A_0^2 a^4 \sin^2\theta]$ (right panel) for $a = 0.8$, $b/a = 0.75$, and $B_\phi = 0$ for shell solutions. Solid curve denotes that for $k = \pi/[4(a-b)]$, while dashed and dot-dashed ones do for $k = \pi/[2(a-b)]$ and $k = 3\pi/[4(a-b)]$, respectively. When k satisfies equation (2.2.32), $B_\theta(t, r = at, \theta) = 0$ and thus $S_r(t, r = at, \theta) = 0$. Electromagnetic energy is not transmitted ahead of the loop top. When k does not satisfy equation (2.2.32), the Poynting flux S_r at $r = at$ is not zero and the electromagnetic energy is transmitted to $r > at$. The physical interpretation of the condition given in equation (2.2.32) is as follows.

Let us consider the MHD waves propagating inside the magnetic loops. The MHD waves consist of the forward wave $B_{\rm for}$ and the reflected wave $B_{\rm ref}$ ($B_{\rm for}$ and $B_{\rm ref}$ are the magnetic fields in the poloidal plane). When the wave $B_{\rm leak}^{III}$ is transmitted to region III (see Fig. 2.8), the electromagnetic energy can be converted to the kinetic and thermal energies in region III. The magnetic field B_θ given in equation (2.2.30) can be expressed by the superposition of the forward and reflected waves. When the density enhancement appears ahead of the magnetic loop in region II, the forward waves can be partially reflected by it. The condition for the perfect reflection should be determined by the wavelength λ and the thickness of the density enhancement $d \sim (a-b)t$. This situation is analogous to the enhancement of the reflection rate by coating a glass with dielectric medium. The reflection rate becomes maximum when the width of the dielectric medium d satisfies $d = (2l+1)\lambda/4$. When $\lambda = 2\pi/k$, this condition coincides with equation (2.2.32). Note that the parameter k in equation (2.2.32) is not exactly the wave number

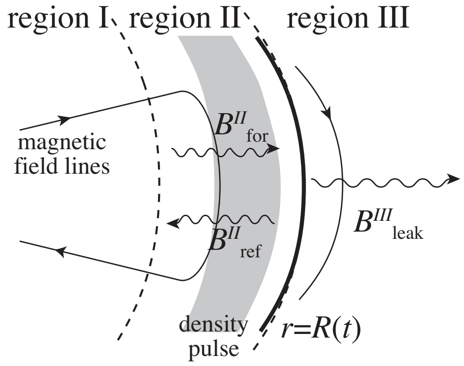

Figure 2.8: Schematic picture of the propagating waves. The forward wave $B_{\rm for}$ and the reflected waves $B_{\rm ref}$ propagate inside the loops. Solid curves show the loop top at $r = R(t)$, while the thin curves show the magnetic field lines. The superposition of these waves determines B_θ in region II. The leak wave $B_{\rm leak}$ appears ahead of the loop top in region III.

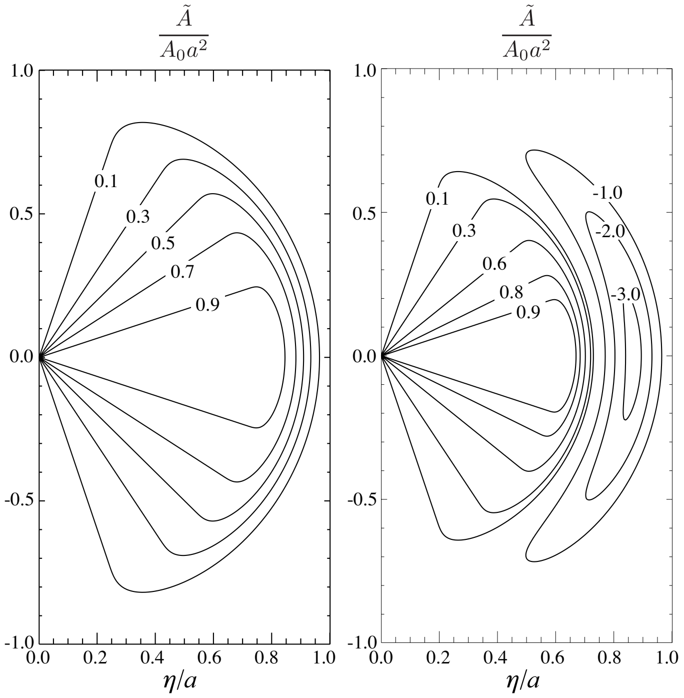

Figure 2.9: Contour plots of the flux function $\tilde{A}/(A_0a^2)$ of the shell solution for $k = \pi/[2(a-b)]$ (left panel) and $k = 3\pi/[4(a-b)]$ (right panel).

but it determines the profile of the magnetic fields (see equations (2.2.3), (2.2.4), and (2.2.5) for the definition of k). When the condition (2.2.32) is satisfied, the MHD waves propagating in the $+r$ direction are totally reflected by the density enhancement produced by the loop expansion. For the dipolar solution, the magnetic energy is transmitted to $r > R(t)$ because the density enhancement does not appear (see the right panels of Fig. 2.3 and Fig. 2.4).

When $k > \pi/[2(a-b)]$, the magnetic shell recedes from $\eta \sim a$ to the region $b < \eta < a$, and a flux rope appears around $\eta = a$ ahead of the magnetic shell. Fig. 2.9 shows the contour plots of the magnetic flux $\tilde{A}$ of the shell solutions for $k = \pi/[2(a-b)]$ (left panel) and $k = 3\pi/[4(a-b)]$ (right panel).

2.2.4 Flux Rope Solutions

Flux rope solutions which include flux ropes inside the expanding magnetic loops are constructed by the flux function (2.2.6).

By substituting equation (2.2.6) into equation (2.1.32), the function Q can be written

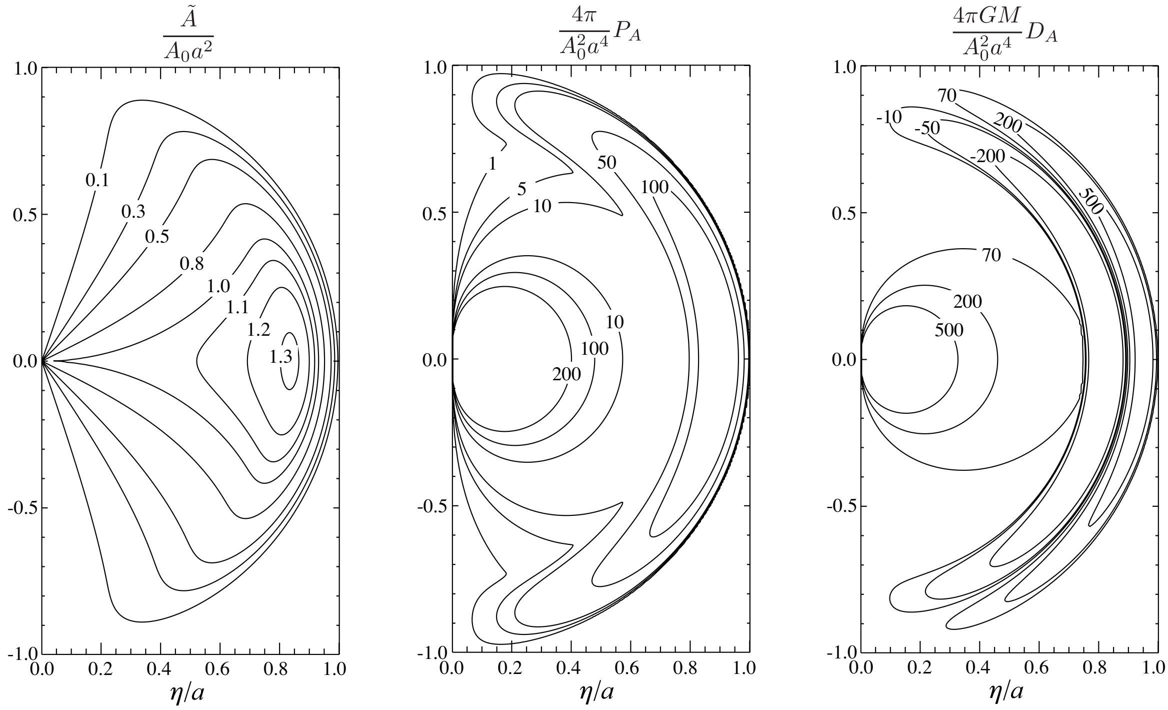

Figure 2.10: Contour plots of the magnetic flux $\tilde{A}$ (left), the poloidal part of the pressure P_A (centre), and that of the gas density D_A (right) for the flux rope solution in $\eta/a - \theta$ plane when $a = 0.8, b = 0.75a$.

as

$$Q^I(\eta, \theta) = \sum_n \frac{Q_{0,n}}{(1 - \eta^2)^{1+\frac{n}{4}}} \sin^n \theta, \tag{2.2.33}$$

$$Q^{II}(\eta, \theta) = \sum_n \frac{Q_{0,n}}{(1 - \eta^2)^{1+\frac{n}{4}}} \Lambda^{\frac{n}{2}}(\eta) \sin^n \theta, \tag{2.2.34}$$

where $Q_{0,n}$ is a constant and subscripts I and II denote region I and region II, respectively. The pressure and density functions (i.e., P and D) can be obtained by substituting equations (2.2.6), (2.2.33), (2.2.34) into equations (2.1.31) and (2.1.33). The functions P and D obtained in region I and region II are given in appendix B.2.

The pressure and the gas density consist of three parts, the isotropic part P_0 and parts representing the interaction with the electromagnetic force by the poloidal and toroidal magnetic fields, P_A and P_Q (see equations (B.2.1) and (B.2.7) for the pressure and equations (B.2.4) and (B.2.10) for the gas density).

Fig. 2.10 shows the contour plots of the magnetic flux $\tilde{A}$ (left), the poloidal part of the pressure P_A (centre), and that of the gas density D_A (right) in $\eta/a - \theta$ plane. Fig. 2.11 shows contour plots of the toroidal magnetic field B_ϕ (left), the toroidal part of the pressure P_Q (centre), and that of the gas density D_Q (right) in $\eta/a - \theta$ plane. The parameters are taken to be $a = 0.8$, $b = 0.75a$, and $m = n = 4$ in both figures. The flux ropes exist behind the loop top (see the left panel of Fig. 2.10).

The magnetic fields in region I and II are explicitly given by

$$B_r^I = \frac{2A_0a^2}{r^2\sqrt{1-(r/t)^2}}\cos\theta, \tag{2.2.35}$$

$$B_\theta^I = -\frac{A_0a^2}{t^2[1-(r/t)^2]^{\frac{3}{2}}}\sin\theta, \tag{2.2.36}$$

$$B_\phi^I = \sum_n \frac{Q_{0,n}}{rt[1-(r/t)^2]^{1+\frac{n}{4}}}(r/t)\sin^{n-1}\theta, \tag{2.2.37}$$

$$B_r^{II} = \frac{2A_0a^2}{r^2}\frac{\Lambda(r/t)}{\sqrt{1-(r/t)^2}}\cos\theta, \tag{2.2.38}$$

$$\begin{aligned} B_\theta^{II} = & \frac{A_0a^2}{t^2}\frac{1}{\left[1-(r/t)^2\right]^{\frac{3}{2}}} \\ & \left\{4\frac{tk}{r}\left[1-(r/t)^2\right]\frac{\sin^3(T(r/t))\cos(T(r/t))}{\sin^4(T(a))} - \Lambda(r/t)\right\}\sin\theta, \end{aligned} \tag{2.2.39}$$

$$B_\phi^{II} = \sum_n \frac{Q_{0,n}}{rt}\frac{\Lambda^{\frac{n}{2}}(r/t)}{\left[1-(r/t)^2\right]^{1+\frac{n}{4}}}\sin^{n-1}\theta. \tag{2.2.40}$$

Here the subscripts I and II denote the magnetic fields in region I and region II, respectively. Similarly to the dipolar and shell solutions, the parameter m represents the Fourier modes which specify where the magnetic twist is injected.

In the limit that $t \gg r$, the flux rope solution reduces to the dipolar solution given by equation (2.2.18), (2.2.19) and (2.2.20). In this limit, the magnetic field becomes stationary and radial.

Note that the field component B_r and B_θ are exactly zero but B_θ is not zero at $r = R(t)$ unless the condition (2.2.32) is satisfied. The electromagnetic energy is transmitted to $r > R(t)$ unless the condition (2.2.32) is satisfied as discussed in the previous subsection. When equation (2.2.32) is satisfied, the Poynting flux is totally reflected at $r = R(t)$ and the electromagnetic energy is not transmitted to $r \geqq R(t)$.

2.3 Physical Properties

Here we discuss physical properties of the three solutions we derived in § 2.2. In this section, we organize our discussion into four parts. First we consider the energetics. Second we show the shell and flux rope structures derived in § 2.2.3 and § 2.2.4 inside

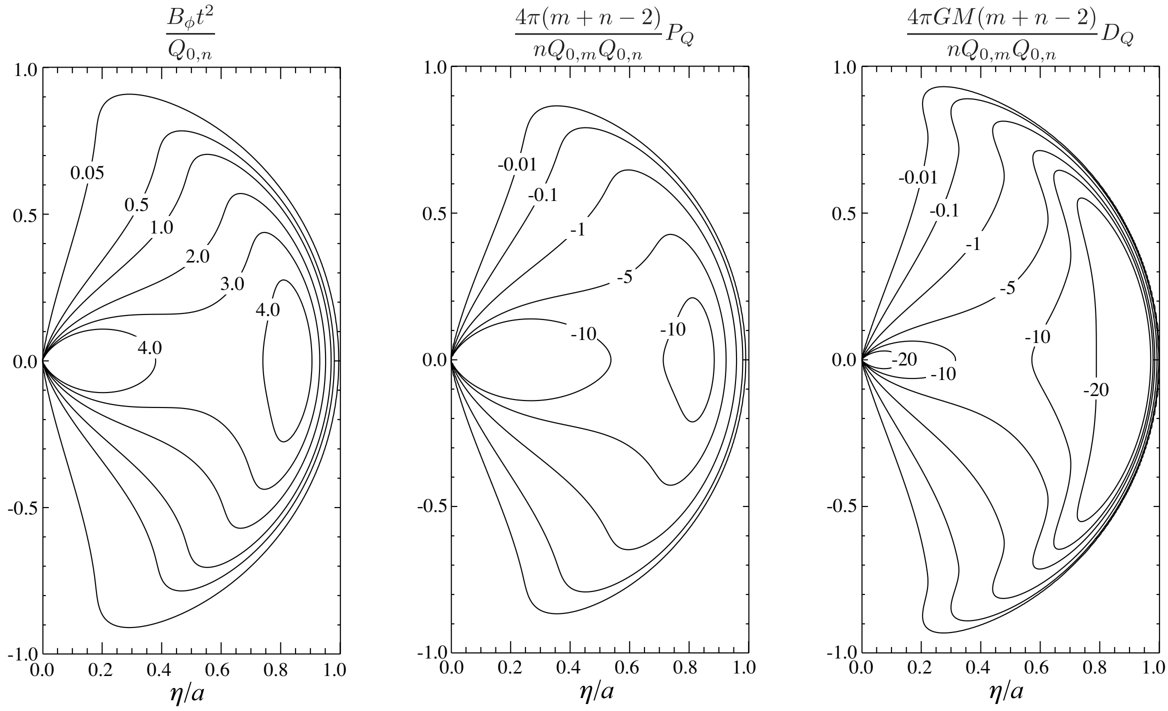

Figure 2.11: Contour plots of the toroidal magnetic field B_ϕ (left), the toroidal part of the pressure P_Q (centre), and that of the gas density D_Q (right) for the flux rope solution in $\eta/a-\theta$ plane when $a=0.8, b=0.75a$, and $n=m=4$.

the magnetic loops. Third we study the relativistic effects, especially the role of the displacement current. Finally, we apply our solutions to SGR flares.

2.3.1 Energetics

First let us consider the dipolar solution without the toroidal magnetic field (i.e., $Q_{0,n}=0$) for simplicity. Total energy $\mathcal{E}$ contained inside the expanding magnetic loops is given as

$$\mathcal{E}=K+U_{\rm in}+U_{\rm th}+U_{\rm E}+U_{\rm M}+W, \tag{2.3.1}$$

where

$$K=\int_V dV\rho\gamma^2, \tag{2.3.2}$$

$$U_{\rm in}=\int_V dV\frac{\Gamma}{\Gamma-1}\gamma^2v^2p, \tag{2.3.3}$$

$$U_{\rm th}=\int_V dV\frac{p}{\Gamma-1}, \tag{2.3.4}$$

$$U_{\rm E}=\int_V dV\frac{\boldsymbol{E}^2}{8\pi}, \tag{2.3.5}$$

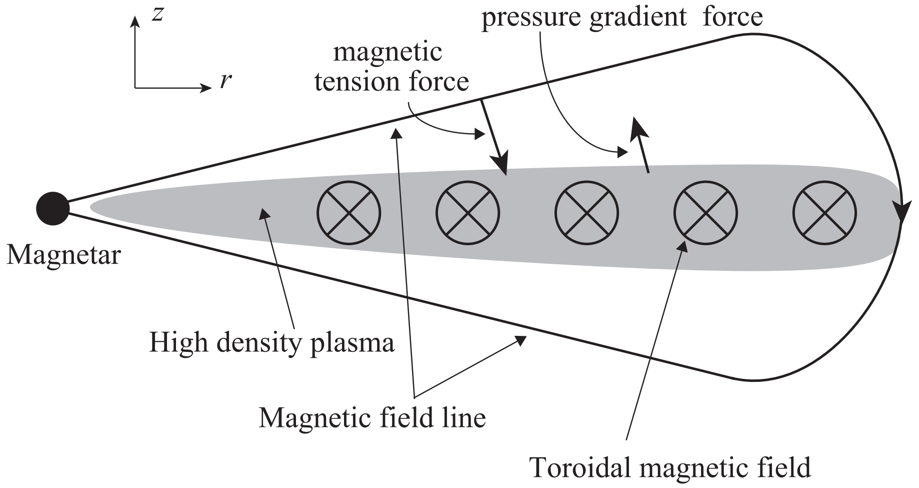

Figure 2.12: A schematic picture showing an expanding magnetic loop. Toroidal magnetic field is created inside the magnetic loop due to the twist injection from the surface of the magnetar. The magnetic pressure gradient force plus the pressure gradient force balances with the magnetic tension force by the poloidal magnetic field.

$$U_{\mathrm{M}} = \int_V dV \frac{\boldsymbol{B}^2}{8\pi}, \tag{2.3.6}$$

$$W = -\int_V dV \frac{GM\gamma\rho}{r}, \tag{2.3.7}$$

are kinetic, thermal inertial, thermal, electric, magnetic, and gravitational potential energies, respectively. Since the solutions we derived describe the freely expanding magnetic loops, i.e., $Dv/Dt = 0$, the total kinetic energy K given by

$$K = \int_V \rho\gamma^2 dV = \int_0^a d\eta \int_0^{2\pi} d\theta \int_0^{\pi} d\phi \ \frac{\eta^2 D(\eta,\theta)}{\sqrt{1-\eta^2}} \sin\theta, \tag{2.3.8}$$

does not change with time. Here the total kinetic energy is integrated inside the spherical surface of $r = R(t)$. Other energies can be evaluated by carrying out the integration directly. The non-kinetic part of the total energy $\mathcal{E}' \equiv U_{\mathrm{in}} + U_{\mathrm{th}} + U_{\mathrm{E}} + U_{\mathrm{M}} + W$ contained inside $r = R(t)$ is then given as

$$\mathcal{E}' = \frac{4A_0^2 a^3}{3t}. \tag{2.3.9}$$

Since the thermal, gravitational potential, and magnetic energies contain infinity due to the divergence of p, ρ, and B_r at $r = 0$ (see equations (2.2.9), (2.2.13), and (2.2.15), respectively), we renormalized the infinite parts of U_{th}, U_{M}, and W to zero (see Low 1982).

The non-kinetic part of the total energy $\mathcal{E}'$ depends on the amplitude of the poloidal magnetic field A_0, but is independent of the isotropic component (i.e., P_0 and D_0). The isotropic component does not contribute to the total energy because the thermal energy of the isotropic plasma cancels with that of the gravitational potential energy.

The energy $\mathcal{E}'$ diverges at $t = 0$ because we assumed a point mass at the origin. In magnetars, since the magnetar has a finite radius R_s, the self-similar expansion will take place when $r > r_0 > R_s$ and $t > t_0$. Let us denote the total energy and the non kinetic part of the total energy inside the spherical surface of $r_0 \equiv R(t_0)$ as $\mathcal{E}_0$ and $\mathcal{E}'_0$, respectively. The expansion takes place when $\mathcal{E}_0 > \mathcal{E}'_0$. Since the total kinetic energy $K = \mathcal{E}_0 - \mathcal{E}'_0$ does not change with time and $\mathcal{E}'(t)$ given in equation (2.3.9) decreases with time for the dipolar solution, $\mathcal{E}(t) = \mathcal{E}'(t) + K < \mathcal{E}'_0 + K = \mathcal{E}_0$. The released energy $\mathcal{E}_0 - \mathcal{E}(t)$ is carried away to $r > R(t)$. This can be confirmed by integrating the energy conservation equation inside the spherical surface $r = R(t)$ as

$$\int_{V(t)} \frac{\partial}{\partial t}\left[(\rho + 4p)\gamma^2 - p + \frac{\boldsymbol{E}^2 + \boldsymbol{B}^2}{8\pi} - \frac{GM\rho\gamma}{r}\right] d^3\boldsymbol{r} + \int_{V(t)} \nabla \cdot \left[(\rho + 4p)\gamma^2 \boldsymbol{v} + \frac{\boldsymbol{E}\times\boldsymbol{B}}{4\pi} - \frac{GM\rho\gamma}{r}\boldsymbol{v}\right] d^3\boldsymbol{r} = 0. \quad (2.3.10)$$

Since this integration is cumbersome, we do not show the details of the calculation. We have to point out that the integration with the volume V cannot be exchanged with the time derivative in the first term since the volume V changes with time.

Next let us consider the case $Q_{0,n} \neq 0$. Since the integration of equations (2.3.2)-(2.3.7) is complex, we evaluate the total energy inside the closed boundary by a different method. Note that equation (2.1.36), which represents equations of motion in the self-similar space, indicates that the self-similar equations we derived are closely related to the static relativistic MHD solutions except the existence of the thermal inertial term and the electric field. We can derive the virial theorem for the relativistic self-similar MHD (see appendix E);

$$3(\Gamma - 1)U_{\rm th} + U_{\rm in} + U_{\rm M} + U_{\rm E} + W = \mathcal{H} + \mathcal{S}, \quad (2.3.11)$$

where

$$\mathcal{H} = \int p\boldsymbol{r} \cdot d\boldsymbol{\mathcal{A}} - \frac{1}{8\pi}\int \left\{2\left[(\boldsymbol{r}\cdot\boldsymbol{E})(\boldsymbol{E}\cdot d\boldsymbol{\mathcal{A}}) + (\boldsymbol{r}\cdot\boldsymbol{B})(\boldsymbol{B}\cdot d\boldsymbol{\mathcal{A}})\right] - (\boldsymbol{E}^2 + \boldsymbol{B}^2)(\boldsymbol{r}\cdot d\boldsymbol{\mathcal{A}})\right\}, \quad (2.3.12)$$

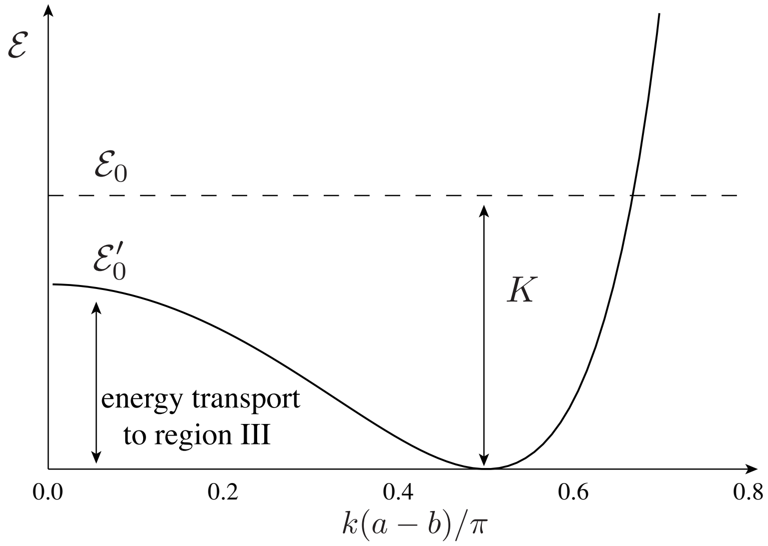

Figure 2.13: k dependence of the non kinetic part of the total energy $\mathcal{E}'$ (solid curve) for the shell and flux rope solutions.

and

$$\mathcal{S} = \int dV \frac{\partial}{\partial t}\left(\boldsymbol{r}\cdot\frac{\boldsymbol{E}\times\boldsymbol{B}}{4\pi}\right). \tag{2.3.13}$$

Here $\boldsymbol{\mathcal{A}}$ is the surface enclosing the volume V. The non-kinetic part of the total energy $\mathcal{E}'$ can be written from equation (2.3.11) as

$$\mathcal{E}' = -(3\Gamma-4)U_{\mathrm{th}} + \mathcal{H} + \mathcal{S}. \tag{2.3.14}$$

We can evaluate $\mathcal{E}'$ inside the expanding spherical surface of $r = R(t)$ by using the fact that $p = \rho = B_r = B_\phi = 0$ at $r = R(t)$ as

$$\mathcal{E}' = \begin{cases} \dfrac{4A_0^2a^3}{3t}, & \text{(dipolar solution)},\\ \dfrac{16A_0^2a^5k^2(1-a^2)\cot^2 T(a)}{3t}, & \text{(shell solution)},\\ \dfrac{16A_0^2a^5k^2\cot^2 T(a)}{3t}, & \text{(flux rope solution)}, \end{cases} \tag{2.3.15}$$

In all solutions, the non-kinetic part of the total energy does not depend on the toroidal magnetic field because the toroidal magnetic field does not change the dynamics of the expanding magnetic loops in the self-similar stage. This can be understood from the fact that when we take $Q_{0,n} = 0$, the solutions we derived satisfy equations (2.1.31), (2.1.32) and (2.1.33) without any modification on the poloidal magnetic field. To understand this reason, let us consider the equation of motion in the θ direction. Since $\boldsymbol{v} = v\boldsymbol{e}_r$, the force balance should be attained in the θ direction (see Fig. 2.12). The pressure P_Q is smaller

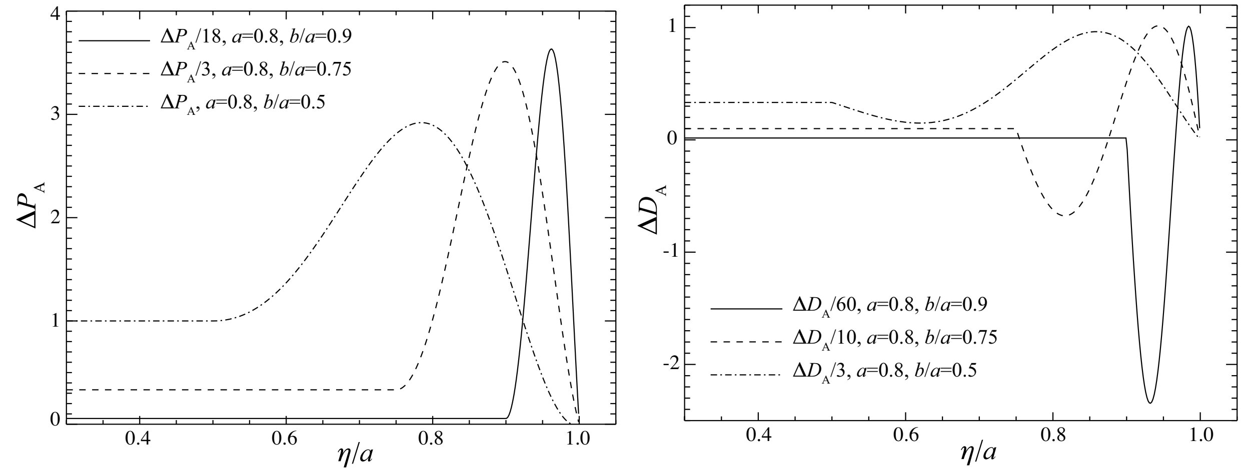

Figure 2.14: The pressure enhancement ΔP_A (left) and the density enhancement ΔD_A (right) for the shell solution are shown as a function of η/a. Solid curve is for $b = 9a/10$, while the dashed and dot-dashed ones are for $b = 3a/4$ and $b = a/2$, respectively. Other parameters are fixed at $a = 0.8$ and $k = \pi/[4(a - b)]$.

for larger toroidal magnetic fields because P_Q is proportional to $-Q_{0,n}^2$ (see equations (2.2.10) for the dipolar solution, (B.1.4) and (B.1.11) for the shell solution, and (B.2.3) and (B.2.9) for the flux rope solution). For larger toroidal magnetic fields, the magnetic pressure gradient force by the toroidal magnetic field balances with the magnetic tension force from the poloidal magnetic field. As a result, the existence of the toroidal magnetic field modifies the plasma distribution, but does not change the dynamics.

Fig. 2.13 shows the k dependence of $\mathcal{E}_0'$ for the shell and flux rope solutions (note that both solutions have the same k dependence). When the condition (2.2.32) is satisfied, the total energy contained inside the magnetic loops is equal to K and conserved for the shell and flux rope solutions because the energy flux is zero at $r = R(t)$. When (2.2.32) is not satisfied, the total energy is larger than K by $\mathcal{E}'$ (see equation (2.2.32)). The excess energy is carried away to the region III ($r > R(t)$) to attain the free expansion, i.e., $Dv/Dt = 0$.

2.3.2 Shell and Flux Rope Structures

Let us examine the density and pressure distribution for the shell solution derived in § 2.2.3. We define the density and pressure enhancements as

$$\Delta P_A = \left[\frac{2\pi\eta^4}{A_0^2 a^4 \sin^2\theta}\right] P_A, \tag{2.3.16}$$

$$\Delta D_A = \left[\frac{\pi G M \eta^3 (1-\eta^2)}{2A_0^2 a^4 \sin^2\theta}\right] D_A, \tag{2.3.17}$$

$$\Delta P_Q = \left[\frac{4\pi(m+n-2)\eta^2(1-\eta^2)}{nQ_{0,m}Q_{0,n}\sin^{m+n-2}\theta}\right] P_Q, \tag{2.3.18}$$

$$\Delta D_Q = \left[\frac{2\pi GM(m+n-2)\eta(1-\eta^2)^2}{nQ_{0,m}Q_{0,n}\sin^{m+n-2}\theta}\right] D_Q, \tag{2.3.19}$$

These functions are normalized to be unity in region I, where the poloidal magnetic field lines are radial for the shell solution. In Fig. 2.14, the pressure and density enhancements, ΔP_A and ΔD_A are plotted for $b = a/2$, $3a/4$, $9a/10$ when $a = 0.8$ and $k = \pi/[4(a-b)]$. In all three cases, the pressure and density pulses appear at the top of the magnetic loops. Their amplitudes are larger for a thinner shell. The peak of the pressure enhancement appears behind that of the density enhancement. This structure comes from the requirement for the force balance with the gravity. As mentioned in § 2.3.1, this relativistic self-similar solution is similar to the static solution in which the force balance is attained. As plasma is swept up into the shell, the density increases inside the shell. To support the gravity by this excess density, the pressure gradient appears behind the density enhancement. The density decrease behind the pressure enhancement also comes from the requirement for the force balance. Since the decrease of the density enables the buoyancy force to push the plasma in the radial direction, this buoyancy force maintains the pressure pulse. These structures are identical to those in non-relativistic solution (Low 1982).

Fig. 2.15 plots ΔP_Q and ΔD_Q for $b = a/2$, $3a/4$, $9a/10$ when $a = 0.8$ and $k = \pi/[4(a-b)]$. As mentioned in § 2.2, the Lorentz force exerted by the toroidal magnetic fields always reduces the pressure. A local minimum of the density enhancement ΔD_Q locates behind a local maximum of $d\Delta P_Q/d\eta$. This structure also comes from the force balance. Pressure gradient force balances with the buoyancy force in the rarefied region.

Next we examine the structure of the flux rope solution derived in § 2.2.4. We define the normalized toroidal magnetic field strength as

$$\Delta B_\phi(\eta) = \frac{B_\phi t^2}{Q_{0,n}\sin^{n-1}\theta}. \tag{2.3.20}$$

Solid curve in Fig. 2.16 shows ΔB_ϕ as a function of η for $b = 0.95a$, while the dash and dot-dashed ones show that for $b = 0.8a$ and $b = 0.65a$, respectively. Other parameters are fixed at $a = 0.8$ and $k = \pi/[4(a-b)]$. The toroidal magnetic field has a peak inside the flux rope. Its amplitude is larger for a larger a and a thinner shell. The shell structure also appears behind the loop top (see Fig. 2.10 and 2.11). Solid curve in Fig. 2.17 shows ΔB_ϕ^2, which corresponds to the magnetic pressure by the toroidal magnetic field, as a function

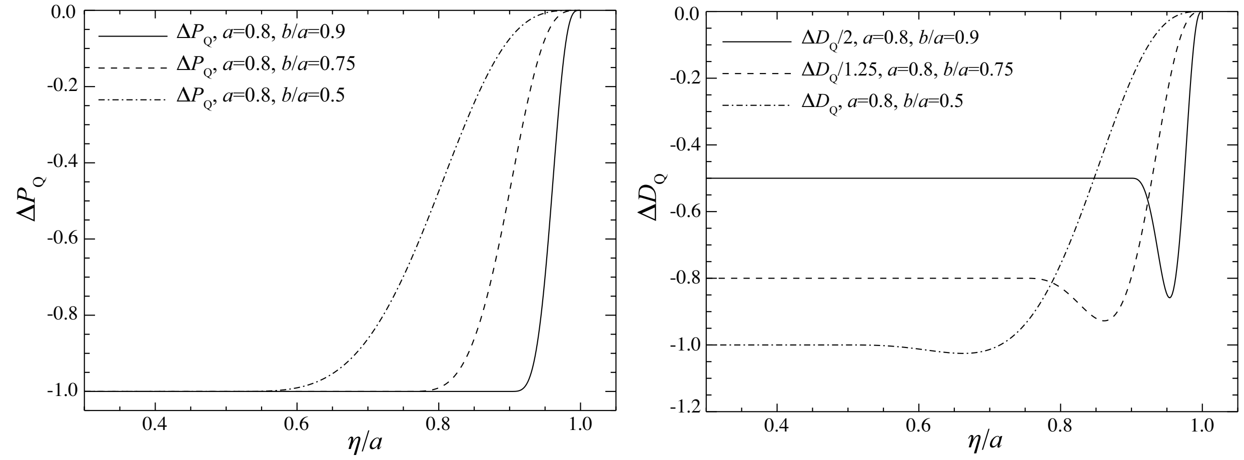

Figure 2.15: The pressure decrement ΔP_Q (left) and the density decrement ΔD_Q (right) by the azimuthal field are shown as a function of η/a for the shell solution. Solid curve is for $b = 9a/10$, while dashed and dot-dashed curves are for $b = 3a/4$ and $b = a/2$, respectively. Other parameters are fixed at $a = 0.8$ and $k = \pi/[4(a-b)]$.

of η for $a = 0.8$, $b = 0.95a$, and $k = \pi/[4(a-b)]$. Dashed and dot-dashed curves show ΔP_Q and ΔD_Q, respectively. Plasma density decreases inside the shell. The decrement of the plasma density leads to the buoyancy force which balances with the pressure gradient force in front of the shell. Behind the shell, the pressure gradient force balances with that of the magnetic pressure. This effect is more prominent for the flux rope solution than for the shell solution since the magnetic pressure is enhanced inside the flux rope.

2.3.3 The Role of the Displacement Current

We showed that P_Q is always negative. On the other hand, P_A can have either positive or negative values. In this subsection, we obtain the condition for $P_A < 0$.

First let us consider the dipolar solution derived in § 2.2.2. The condition that P_A given by equation (2.2.9) is positive in $0 \leqq \eta \leqq a$ is given by

$$2a^2 - 3a^2\eta^2 - \eta^4 + 2\eta^6 \geqq 0. \tag{2.3.21}$$

The critical value a_* for $P_A > 0$ in $0 \leqq \eta \leqq a$ is

$$a_* = \frac{\sqrt{69 + 11\sqrt{33}}}{12} \simeq 0.958. \tag{2.3.22}$$

When $a > a_*$, P_A has negative values in the domain $0 \leqq \eta \leqq a$. Since a denotes the expansion speed of the magnetic loops at $r = R(t)$, the above condition indicates that P_A can be negative for faster expansion.

Next let us calculate the azimuthal component of the current density,

$$j_\phi = j_{\rm rot} + j_{\rm disp}, \tag{2.3.23}$$

where

$$j_{\rm rot} \equiv \frac{(\nabla \times \boldsymbol{B})_\phi}{4\pi} = \frac{A_0 a^2}{4\pi r^3} \frac{2a^2 - 5a^2\eta^2 + 5\eta^4 - 2\eta^6}{(1-\eta^2)^{\frac{5}{2}}} \sin\theta, \tag{2.3.24}$$

$$j_{\rm disp} \equiv -\frac{1}{4\pi}\frac{\partial E_\phi}{\partial t} = -\frac{A_0 a^2}{4\pi r^3} \frac{\eta^4 \left(6 - 3a^2 - 5\eta^2 + 2\eta^4\right)}{(1-\eta^2)^{\frac{5}{2}}} \sin\theta, \tag{2.3.25}$$

and

$$j_\phi = \frac{A_0 a^2}{4\pi r^3} \frac{2a^2 - 3a^2\eta^2 - \eta^4 + 2\eta^6}{(1-\eta^2)^{\frac{3}{2}}} \sin\theta. \tag{2.3.26}$$

The current $j_{\rm rot}$ is always positive, while $j_{\rm disp}$ has negative values for a larger a in $0 \leqq \eta \leqq a$. The displacement current $j_{\rm disp}$ cannot be ignored for a larger a and it reduces the azimuthal current j_ϕ. Thus the current j_ϕ changes its sign for a larger a. Remember that the pressure P is determined by the θ component of the equation of motion given by

$$(-\nabla p + \boldsymbol{j} \times \boldsymbol{B} + \rho_e \boldsymbol{E})_\theta = 0. \tag{2.3.27}$$

According to the definition of P_A and P_Q, the poloidal component of equation (2.3.27) is given by

$$\frac{1}{t^4 r}\frac{\partial P_A}{\partial \theta} = j_\phi B_r. \tag{2.3.28}$$

Since both $\partial P_A/\partial\theta$ and $j_\phi B_r$ depend on θ by $\sin\theta\cos\theta$, and $B_r/\cos\theta$ is positive, the sign of P_A is determined by that of $j_\phi/\sin\theta$. Thus P_A can be negative when the displacement current $j_{\rm disp}$ dominates the current $j_{\rm rot}$. The condition that $j_\phi \leqq 0$ coincides with the condition that $P_A \leqq 0$ (i.e. $a \geqq a_*$, where a_* is given by equation (2.3.22)).

Next let us consider the shell and flux rope solutions. Since these solutions are more complex, the equation $P_A = 0$ is solved numerically. Instead of using parameters a and b, we introduce the following parameters,

$$V_{\rm max} = a, \tag{2.3.29}$$

$$\Delta = \frac{a-b}{a}. \tag{2.3.30}$$

These parameters denote the maximum speed of the expanding loops and thickness of the shell behind the loop top, respectively. Fig. 2.18 is a diagram showing whether the solution that $P_A = 0$ exists for the shell and flux rope solutions in the parameter space of $V_{\rm max}$ and Δ for $k = \pi/[4(a-b)]$. Solutions where $P_A = 0$ exist in the shaded area for the shell

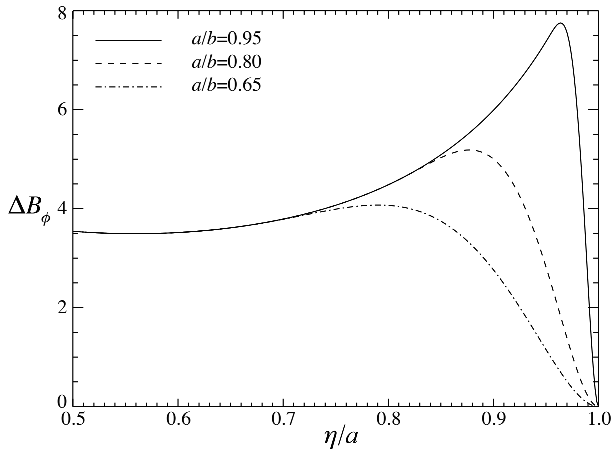

Figure 2.16: Distribution of ΔB_ϕ for the flux rope solution as a function of η/a for $a = 0.8$. Solid curve is for $b/a = 0.95$, while dashed and dot-dashed ones are for $b/a = 0.8$ and $b/a = 0.65$, respectively.

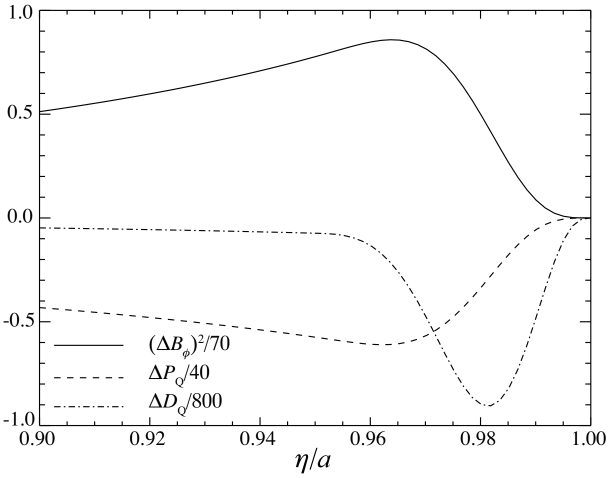

Figure 2.17: Distribution of ΔB_ϕ^2 for the flux rope solution as a function of η/a for $a = 0.8$ and $b/a = 0.95$ (solid curve). Dashed and dot-dashed ones denote ΔP_Q and ΔD_Q, respectively.

solution and in the grey area for the flux rope solution. Similarly to the dipolar solution, the effect of the displacement current is more prominent for a larger $V_{\max}$. Generally, P_A is smaller for a larger $V_{\max}$ and thicker shells in parallel that the displacement current becomes important for larger $V_{\max}$ and Δ. For the flux rope solution, the displacement current is important not only in region II but in region I (right bottom region in Fig. 2.18). In this case, P_A is negative for $b \geqq 0.817$.

2.3.4 Application to SGR Explosions

SGR flares can be triggered by energy injection into magnetic loops at the surface of a strongly magnetized neutron star (e.g., Lyutikov 2006). When sufficiently large energy is injected, the magnetic loops will become dynamically unstable, and expand relativistically. Magnetic energy release in the expanding magnetic loops can be the origin of SGR flares. The expanding magnetic loops will also produce magnetosonic waves propagating ahead of the loops. High energy particles can be produced in the magnetic reconnection inside the loops, and in shock fronts formed ahead of the loops.

We did not solve the structure of the region ahead of the magnetic loops ($r > R(t)$). When the outer region is a vacuum, electromagnetic waves will be emitted from the boundary at $r = R(t)$. When the plasma density is much larger than the Goldreich-Julian density (Goldreich & Julian 1969) and the wave frequency is much smaller than the plasma frequency, the outer plasma can be studied by using MHD equations. It will be our future work to connect the self-similar solutions inside $r = R(t)$ and the solutions in $r \geqq R(t)$.

Now let us estimate the energy for the SGR explosion based on the self-similar solutions. Let us take the field strength to be 10^{15} Gauss (Kouveliotou et al. 1998; Ibrahim et al. 2002; Ibrahim et al. 2003) at the stellar radius $R_s = 10^6$ cm. This leads to

$$\frac{2A_0 a^2}{R_s^2} = 10^{15} \text{ Gauss}. \tag{2.3.31}$$

By assuming that the self-similar expansion begins when $t_0 = R_s/a$, the released energy from the expanding magnetic loops can be estimated from equation (2.3.15) as

$$\mathcal{E}' = \begin{cases} 6 \times 10^{46} \text{ erg}, & \text{(dipolar solution)}, \\ 2 \times 10^{47} \Delta^{-2} \text{ erg}, & \text{(shell solution)}, \\ 8 \times 10^{47} \Delta^{-2} \text{ erg}, & \text{(flux rope solution)}. \end{cases} \tag{2.3.32}$$

Here we take $a = V_{\max} \simeq 0.9$ and $k = \pi/[4(a-b)]$. These results agree with the observed energy of SGR giant flares (Hurley et al. 2005; Palmer et al. 2005; Terasawa et al. 2005). Note that the total energy contained in the expanding magnetic loops is more energetic for thinner shells. The non-kinetic part of the total energy $\mathcal{E}'$ is inversely proportional to the square of the shell thickness. When some fraction of the kinetic energy K is converted to the electromagnetic energy, the released energy can be larger than that estimated by equation (2.3.32).

2.4 Summary & Discussions

By extending the self-similar solutions derived by Low (1982), we derived self-similar solutions of relativistically expanding magnetic loops taking into account the toroidal magnetic fields. The dipolar solution derived in § 2.2.2 gives us an insight into the relativistic expansion of the magnetic loops because of its simplicity. However, the shell and flux rope solutions derived in § 2.2.3, 2.2.4 have more physically interesting properties such as an enhanced magnetic pressure at the shells and flux rope structures. Such configurations might be more probable for SGR flares.

The equations of motion in the self-similar stage are similar to those of the static equilibrium state except the existence of the relativistic thermal inertial term and the electric field. This fact allows us to evaluate the non-kinetic part of the total energy in the magnetic loops by using the virial theorem. The magnetic loops with shell or flux rope

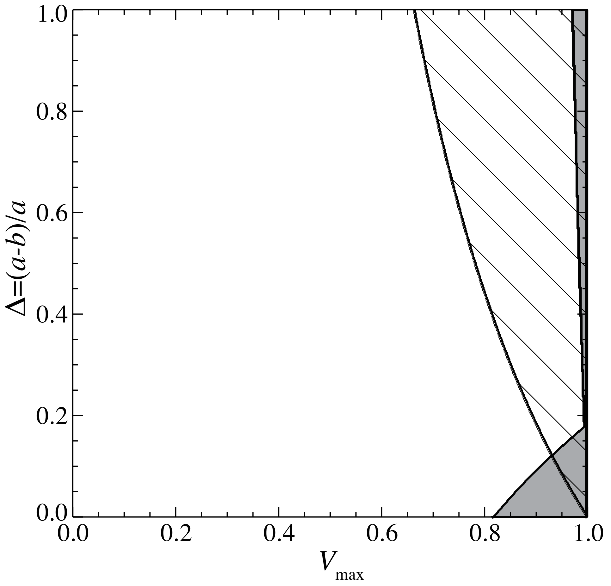

Figure 2.18: The diagram showing where the solution $P_A = 0$ exists in the parameter space $V_{\rm max}$ and $\Delta = (a-b)/a$ when $k = \pi/[4(a-b)]$ for the shell solution (the shaded area) and for the flux the rope solution (grey area).

structures carry more energy than the simple dipole solution. The energy is comparable to the observed energy of the SGR giant flares.

In relativistically expanding magnetic loops, the effect of the displacement current becomes important. In dipolar solution, the displacement current becomes larger than the real current $\nabla \times \boldsymbol{B}/(4\pi)$ for faster expansion speed ($V_{\rm max} > a_*$). This effect reduces the toroidal current and weakens the magnetic tension force. To balance the reduced magnetic tension force, the pressure decreases.

We found that the energy is transferred to $r > R(t)$ in dipolar solutions. In the shell and flux rope solutions, the energy is transferred to $r > R(t)$ unless condition (2.2.32) is satisfied. The condition can be interpreted as that for the total reflection of the MHD waves in the shell. Dipolar solutions always have leakage (transmission of Poynting flux to the region $r \geqq R(t)$) because $B_\theta \neq 0$ at $r = R(t)$. The shell and flux rope solutions have perfectly reflecting solutions in which the total energy in $r < R(t)$ is conserved. It means that the solutions are energy eigenstates of the system. The eigenstates can be obtained by adjusting the parameter k.

In this chapter, we obtained solutions for freely expanding magnetic loops, i.e., $Dv/Dt = 0$. We assumed that the magnetic loops have sufficiently large energy to drive the expansion. When the flux function $\tilde{A}$ increases with time, the toroidal magnetic fields will also increase time. The toroidal magnetic fields will then affect the dynamics through the magnetic pressure. Such solutions can describe the accelerating magnetic loops.

Magnetic fields can be expressed as the sum of the Fourier modes in the polar angle. The modes and their amplitudes should be determined at the boundary where the magnetic twist is injected on the surface of the star. It is not shown but we can construct more complex solutions that the poloidal magnetic fields are expressed by the sum of the Fourier modes, i.e., $\tilde{A} \propto \sin^n \theta$. In actual explosion, the opening angle of the expanding magnetic loops depends on the location at which the magnetic twist is injected on the surface of the central star. Such a solution may be expressed as the sum of the Fourier modes for the poloidal and toroidal magnetic fields. We should note that SGR flares are not necessarily axisymmetric. Models including the non-axisymmetrically expanding magnetic loops will be a subject of future works.

Chapter 3

Requirement for the Relativistic Outflow from Relativistic Magnetic Reconnection

Until recent years, there are few theoretical studies on the relativistic magnetic reconnection (Blackman & Field 1994; Lyutikov & Uzdensky 2003; Lyubarsky 2005). Lyubarsky (2005) studied the steady state Sweet-Parker type relativistic magnetic reconnection model. They concluded that the reconnection rate becomes closer to unity by the effect of the Lorentz contraction and that the outflow is accelerated in proportion to the magnetization parameter of the inflow. In their treatment, all the magnetic energy is assumed to be converted to the outflow kinetic energy; They ignored the gas pressure enhancement in the outflow region. Lyubarsky (2005) pointed out the importance of the increase in the inertia by the gas pressure. In relativistic magnetic reconnection, the ratio of thermal to rest mass energy densities is larger than unity to achieve the pressure balance across the current sheet. By this enhanced gas pressure, plasma inertia increases through the relativistic effect. He concluded that the outflow speed is only mildly relativistic at most in contrast to former results. The reconnection rate is almost equal to the inverse of the aspect ratio of the dissipation region δ/L, where δ and L are the size of dissipation region along the inflow and outflow directions, respectively.

Now let us reconsider the effects of gas pressure inside the current sheet. The pressure equilibrium across the current sheet implies

$$p_{\mathrm{N}} = \frac{B_{x,\mathrm{i}}^2}{8\pi}, \tag{3.0.1}$$

where p_{N} is the gas pressure at the neutral point and $B_{x,\mathrm{i}}$ is the magnetic field in the inflow region which reconnects in the diffusion region. When the magnetic energy density

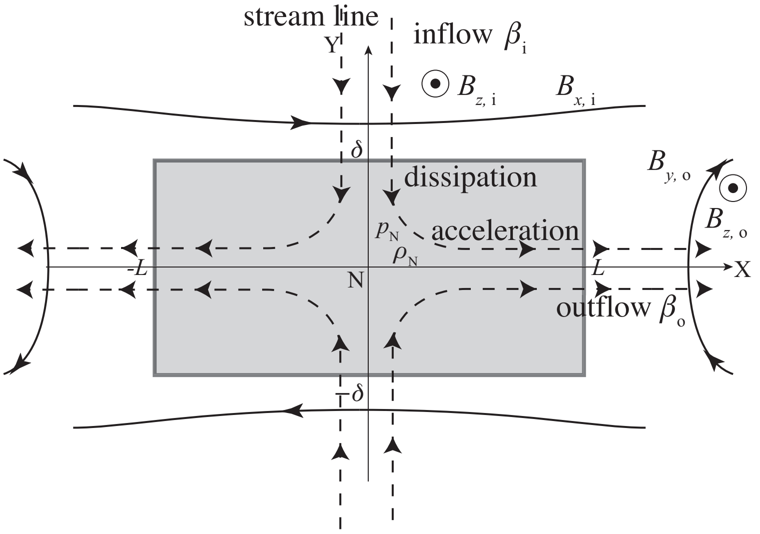

Figure 3.1: Schematic picture of the Sweet-Parker magnetic reconnection in $X-Y$ plane. The electric resistivity is non-zero only in the shaded region. Solid curves depict magnetic field lines. Stream lines are shown by dashed curves.

exceeds the rest mass energy density in the inflow region, also the thermal energy density $p_{\rm N}/(\Gamma-1)$, where Γ is the specific heat ratio, exceeds the rest mass energy density. This gas pressure has two effects. First, the enhanced thermal energy leads to the increase in the inertia. It becomes harder to accelerate plasma for a larger thermal energy. Second, the expansion due to the enhanced gas pressure accelerates the plasma. In addition, the expansion leads to decrease in the inertia since enthalpy decreases. Lyubarsky (2005) estimated the outflow velocity by including the pressure gradient force, but the effect of the enthalpy decrease was ignored. When the plasma expands, the plasma enthalpy, in turn, the inertia should decrease. Our question is which effect is more efficient. In other words, we would like to answer whether relativistically hot plasma can be accelerated by the gas pressure gradient force, or, can not be accelerated because of the enhanced inertia. It depends on the pressure gradient between the neutral point and the outflow region. If the gas pressure in the outflow region is much smaller than that at the neutral point, plasma will be accelerated to relativistic speed by the pressure gradient force and decrease in the inertia.

This chapter is organized as follows: In § 3.1, we present the basic equations and the model. The results are shown in § 3.2. Lastly, we summarize and discuss our results in § 3.3.

3.1 Basic Equations and Model

We consider a steady state reconnection in the Cartesian coordinates, $(X,\ Y,\ Z)$. Let the neutral sheet be located on the plane of $Y = 0$. All the physical variables are assumed to be independent of Z for simplicity. The electric resistivity is assumed to be applicable only within the diffusion region of $|X| \leq L$ and $|Y| \leq \delta$ (see, Fig. 3.1). Thus, the ideal relativistic MHD equations are applied outside the diffusion region. The X-component of the magnetic field, the reconnection field, is positive ($B_x > 0$) in the upper half space ($Y > 0$), while it is negative in the lower half space. The Z-component of magnetic field, the guide field, is positive everywhere ($B_z > 0$). We assume the point symmetry around the origin and reflection symmetry with respect to $X = 0$. Thus only the first quadrant is considered in the following.

A plasma element flows across the diffusion region along the stream line as shown by the dashed curves in Fig. 3.1. The flow velocity is assumed to be constant at $v_{\rm i} = c\beta_{\rm i}$ in the inflow region, where $\beta_{\rm i}$ is the inflow velocity in unit of c. The inflow is assumed to be cold and the thermal pressure is neglected. The magnetic energy is converted to the thermal energy through the reconnection in the diffusion region. Subsequently, the plasma is accelerated by the gas pressure gradient and electromagnetic forces to flow out in the X-direction. The outflow velocity is assumed to be constant as $v_{\rm o} = c\beta_{\rm o}$ in the outflow region. The plasma is assumed to be an ideal gas of which specific heat ratio is Γ. The proper density (ρ), proper gas pressure (p), and magnetic field in observer frame ($\boldsymbol{B}$) are assumed to be uniform in the inflow and outflow regions. All the variables with the subscript i denote the values in the inflow region, while those with the subscripts o and N do the values in the outflow region and the neutral point, respectively.

From the mass conservation, we obtain

$$\rho_{\rm i}\gamma_{\rm i}\beta_{\rm i}L = \rho_{\rm o}\gamma_{\rm o}\beta_{\rm o}\delta, \tag{3.1.1}$$

where γ denotes the Lorentz factor,

$$\gamma = (1-\beta^2)^{-1/2}. \tag{3.1.2}$$

The energy conservation gives

$$\rho_{\rm i}c^2\gamma_{\rm i}^2\beta_{\rm i}L\left(1+\sigma_{\rm i}\right) = \rho_{\rm o}c^2\gamma_{\rm o}^2\beta_{\rm o}\delta\left(1+\alpha_{\rm o}+\sigma_{\rm o}\right), \tag{3.1.3}$$

where

$$\alpha \equiv \frac{\Gamma}{\Gamma-1}\frac{p}{\rho c^2}, \tag{3.1.4}$$

and

$$\sigma = \frac{|\boldsymbol{B}|^2}{4\pi\rho c^2\gamma^2}. \tag{3.1.5}$$

Here we assume that the thermal pressure is small and can be ignored in the inflow region. The symbol α denotes the ratio of the thermal enthalpy and rest mass energy. The symbol σ denotes the magnetization parameter and $\boldsymbol{B}$ does the magnetic field vector in the observer frame. From equations (3.1.1) and (3.1.3), we obtain

$$(1+\sigma_{\mathrm{i}})\,\gamma_{\mathrm{i}} = (1+\alpha_{\mathrm{o}}+\sigma_{\mathrm{o}})\,\gamma_{\mathrm{o}}. \tag{3.1.6}$$

This equation is equivalent to the Bernoulli's theorem and means that the specific enthalpy remains constant between the inflow and outflow. The enthalpy is the product of the Lorentz factor and inertia. The inertia includes thermal and magnetic energies as well as that of the rest mass, since we are dealing with relativistic plasma. For an ultra-relativistic outflow ($\gamma_{\mathrm{o}} \gg 1$), the inertia in the outflow region should be much smaller than the specific enthalpy of the inflow.

We obtain

$$\beta_{\mathrm{i}} B_{z,\mathrm{i}} L = \beta_{\mathrm{o}} B_{z,\mathrm{o}} \delta, \tag{3.1.7}$$

from the Z-component of the induction equation and

$$\beta_{\mathrm{i}} B_{x,\mathrm{i}} = \beta_{\mathrm{o}} B_{y,\mathrm{o}}. \tag{3.1.8}$$

from the X- and Y-component of the Faraday's law.

When the inflow (β_{i}, $B_{x,\mathrm{i}}$, $B_{z,\mathrm{i}}$, and ρ_{i}) and the size of the diffusion region (L and δ) are given, equations (3.1.1), (3.1.6), (3.1.7), and (3.1.8) give us four independent relations for five unknowns, β_{o}, $B_{x,\mathrm{o}}$, $B_{z,\mathrm{o}}$, ρ_{o}, and p_{o}. An independent relation is required to determine the outflow. A simple solution to close the equation is to ignore the thermal pressure in the outflow region by setting $p_{\mathrm{o}} = 0$ (Blackman & Field 1994; Lyutikov & Uzdensky 2003) However, as Lyubarsky (2005) pointed out, we cannot ignore the increase in inertia due to the enhanced thermal energy. Instead, Lyubarsky (2005) used the momentum equation between the neutral point and the outflow region to close the system. He estimated that the pressure gradient between the neutral point and the outflow region is at most $\delta p = p_{\mathrm{N}} - p_{\mathrm{o}} \sim B_{x,\mathrm{i}}^2/8\pi$. Since $p_{\mathrm{N}} = B_{\mathrm{i}}^2/(8\pi)$ from the pressure balance condition across the current sheet (see equation (3.0.1)), this approximation is in parallel to $p_{\mathrm{o}} \sim 0$. The thermal energy is used for acceleration by the expansion. When plasma expands, the plasma enthalpy, in turn, the plasma inertia should decreases. This effect was not included in his treatment.

In this chapter, we study the case when $0 \leq p_{\rm o} \leq p_{\rm N}$ by including the effect of decreasing in the enthalpy. For this purpose, we use the entropy conservation equation instead of the momentum conservation equation. The entropy is a natural variable to use since it describes the amount of the thermal energy and is independent of the other field variables such as the pressure and magnetic field strength. The entropy never decreases. It increases by the magnetic energy release into the thermal energy but will be nearly constant during the subsequent expansion phase. Thus we assumed that the magnetic energy release is prompt and the entropy is conserved between the neutral point and the outflow region. The assumption that the magnetic energy is promptly converted into the thermal energy is plausible by considering the pressure balance across the current sheet given in equation (3.0.1). When the entropy is constant along the stream line after the prompt energy conversion, the plasma is accelerated by the pressure gradient and the inertia decrease. Note that one can derive the energy conservation equation from the entropy and momentum conservation equations. While the difference between the momentum equation and the energy conservation equation vanishes for an ultra-relativistic flow, the entropy conservation equation is quite different from the energy conservation equation. Furthermore we need to evaluate an average Lorentz force to integrate the momentum equation. The evaluation can be replaced by the constancy of the outflow entropy. The constancy of the outflow entropy is physics oriented while the average Lorentz force is only order of magnitude estimate.

If we have one more relation, we can determine the inflow velocity, i.e., the reconnection rate. Blackman & Field (1994) and Lyutikov & Uzdensky (2003) imposed the incompressibility, $\rho_{\rm i} = \rho_{\rm o}$ to evaluate the reconnection rate. The incompressibility is a good approximation when the flow is subsonic. However, it is not a good approximation for a relativistic flow since the sound speed is limited at $c/\sqrt{3}$ (see, e.g., Landau & Lifshitz 1959; Mihalas & Mihalas 1984, or Appendix A.3.1) and the flow should be supersonic. On the other hand, Lyubarsky (2005) evaluated the reconnection rate applying $\gamma_{\rm o} = 1$ for the outflow. This evaluation is based on his result that the outflow is non-relativistic or semi-relativistic at most. The outflow velocity is slow in his model since he neglected the decrease in the enthalpy due to the expansion. At this moment, we have no alternative idea to fix the reconnection rate and the inflow velocity (reconnection rate) is left as a free parameter.

We assume that the density of the plasma in the neutral sheet is the same as that of the inflow,

$$\rho_{\rm N} = \rho_{\rm i}. \tag{3.1.9}$$

In other words, the magnetic energy release is so prompt that the plasma does not have time to expand in the neutral sheet. We assume that the plasma evolves adiabatically after the prompt heating by magnetic energy release. We then obtain the closure relation,

$$\frac{p_{\rm N}}{\rho_{\rm N}^{\Gamma}} = \frac{p_{\rm o}}{\rho_{\rm o}^{\Gamma}}. \tag{3.1.10}$$

Note that we do not assume incompressibility between the neutral sheet and the outflow region. We rewrite the second term in the right hand side of equation (3.1.6) as

$$\alpha_{\rm o} = \frac{\Gamma\gamma_{\rm i}^2}{2(\Gamma-1)}\sigma_{\rm i}x^{\Gamma-1}\cos^2\theta_{\rm i}, \tag{3.1.11}$$

where

$$x \equiv \frac{\rho_{\rm o}}{\rho_{\rm i}} = \frac{\gamma_{\rm i}\beta_{\rm i}L}{\gamma_{\rm o}\beta_{\rm o}\delta}, \tag{3.1.12}$$

and

$$\tan\theta_{\rm i} = \frac{B_{z,{\rm i}}}{B_{x,{\rm i}}}, \tag{3.1.13}$$

using equations (3.0.1), (3.1.1), (3.1.9), and (3.1.10). The third term in the right hand side of the equation (3.1.6) is rewritten as

$$\sigma_{\rm o} = \sigma_{\rm i}x\cos^2\theta_{\rm i}\left[\left(\frac{\delta}{L}\right)^2 + \tan^2\theta_{\rm i}\right], \tag{3.1.14}$$

by using equations (3.1.1) and (3.1.8). Substituting equations (3.1.11) and (3.1.14) into equation (3.1.6), we obtain

$$(1+\sigma_{\rm i})\gamma_{\rm i} = h_{\rm o}\gamma_{\rm o}, \tag{3.1.15}$$

where

$$h_{\rm o} = 1 + \sigma_{\rm i}\cos^2\theta_{\rm i}\left\{2\gamma_{\rm i}^2x^{\frac{1}{3}} + \left[\left(\frac{\delta}{L}\right)^2 + \tan^2\theta_{\rm i}\right]x\right\}. \tag{3.1.16}$$

We assume $\Gamma = 4/3$ in the following. By prescribing the inflow velocity $\beta_{\rm i}$, magnetization parameter σ_i, pitch angle $\theta_{\rm i}$, aspect ratio L/δ, and energy conversion parameter f, the outflow velocity is given by solving equation (3.1.15) numerically with the bisection method. The other variables in the outflow region are obtained from equations (3.1.1), (3.1.8), (3.1.7), (3.1.11), and (3.1.14).

3.2 Results

3.2.1 Case of $B_{\mathrm{z}} = 0$ ($\theta_{\mathrm{i}} = 0$)

First, we consider the case in which the guide field (B_z) vanishes. The thick curves in Fig. 3.2 denote the specific momentum of the outflow $u_{\mathrm{o}} \equiv \gamma_{\mathrm{o}}\beta_{\mathrm{o}}$ as a function of the magnetization parameter of the inflow σ_{i}, for $\beta_{\mathrm{i}} = 10^{-6}$. The thin curves denote the ratio of the thermal enthalpy to the rest mass energy of the outflow, α_{o}. The solid curves are for the aspect ratio L/δ=10, while the dashed and dot-dashed ones are for L/δ=100 and 1000, respectively.

The specific momentum of the outflow increases with σ_{i}, when β_{i} and L/δ are fixed. It approaches to the saturation value in the limit of large σ_{i}, while it is proportional to $\sqrt{\sigma_{\mathrm{i}}}$ when σ_{i} is small. The slope, $d\ln u_{\mathrm{o}}/d\ln\sigma_{\mathrm{i}}$, is steep for the intermediate σ_{i}. The ratio of the thermal enthalpy to the rest mass energy of the outflow α_{o}, increases with increase in σ_{i} without saturation.

This result can be explained as follows. When α_{o} and $(\delta/L)^2$ are much smaller than unity ($\alpha_{\mathrm{i}} \ll 1$ and $(\delta/L)^2 \ll 1$), equation (3.1.15) reduces to equation (32) of Lyutikov & Uzdensky (2003)

$$(1+\sigma_{\mathrm{i}})\gamma_{\mathrm{i}} = \gamma_{\mathrm{o}}. \tag{3.2.1}$$

When β_{i} is negligibly small and σ_{i} is much smaller than unity, the outflow velocity is $\beta_{\mathrm{o}} \simeq \sqrt{2\sigma_{\mathrm{i}}} = \sqrt{2}\beta_{\mathrm{A}}$ where β_{A} is the Alfvén velocity in unit of c. This result is equivalent to that of the conventional Sweet-Parker reconnection model when $p_{\mathrm{o}} = p_{\mathrm{i}}$ (see, e.g., Priest & Forbes (2000)). When $\sigma_{\mathrm{i}} \gtrsim 1$, $\beta_{\mathrm{i}} \ll 1$, and $\alpha_{\mathrm{o}} \ll 1$, the outflow velocity is close to the light speed and the specific momentum is proportional to $u_{\mathrm{o}} \simeq \sigma_{\mathrm{i}} + 1$,

Next we consider the case that the outflow is hot, i.e., $\alpha_{\mathrm{o}} \gtrsim 1$. When the aspect ratio is much larger than unity ($(L/\delta)^2 \gg 1$) and the inflow velocity is negligibly small so that γ_{i} is very close to unity, the magnetization parameter σ_{i} should be appreciably larger than unity for the plasma to be hot (see, equation (3.1.6)). Then equation (3.1.15) can be rewritten as

$$1+\sigma_{\mathrm{i}} = 2\sigma_{\mathrm{i}}\left(\frac{u_{\mathrm{i}}L}{u_{\mathrm{o}}\delta}\right)^{\frac{1}{3}}\gamma_{\mathrm{i}}\gamma_{\mathrm{o}}. \tag{3.2.2}$$

The outflow velocity is obtained by taking $u_{\mathrm{i}} \simeq \beta_{\mathrm{i}}$ and $u_{\mathrm{o}} \simeq \gamma_o$. Then the specific momentum of the outflow is evaluated to be

$$u_{\mathrm{o}} \sim u_{\mathrm{o}}^{\mathrm{sat}} = \sqrt{\frac{1}{8}\frac{\delta}{L}\frac{1}{\beta_{\mathrm{i}}}}, \tag{3.2.3}$$

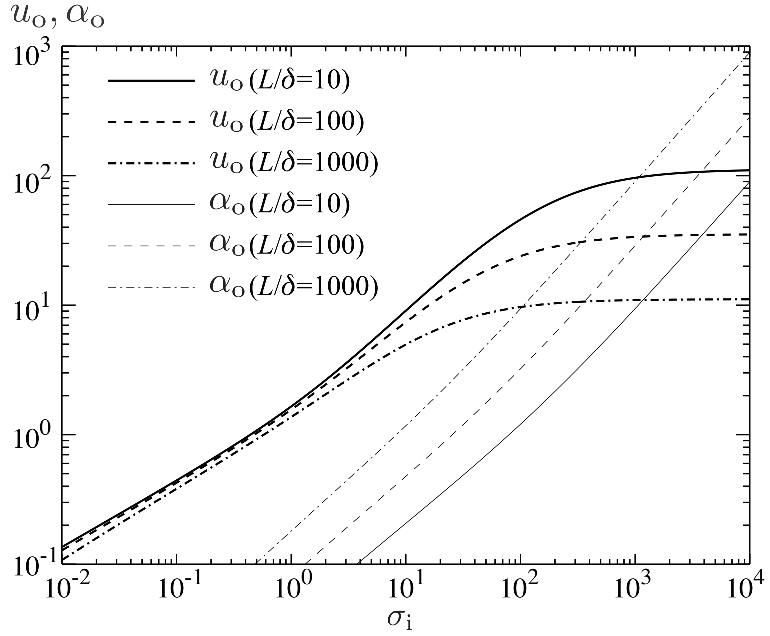

Figure 3.2: Specific momentum of the outflow $u_o \equiv \gamma_o\beta_o$ (thick curves) as a function of the magnetization parameter σ_i for $\beta_i = 10^{-6}$. The thin curves denote the ratio of the thermal enthalpy to rest mass energy in the outflow region, α_o. The solid curves are for L/δ=10, while the dashed and dot-dashed ones are for L/δ=100 and 1000, respectively.

by using $(1+\sigma_i)/\sigma_i \simeq 1$.

This equation indicates two important points. First, the saturated outflow velocity does not depend on σ_i. The increase in the magnetic energy is balanced with the increase in the thermal energy and the magnetic energy is not used for acceleration. Another important result is that the outflow velocity is reciprocal to the square root of the inflow velocity. This implies that the outflow velocity is smaller for a larger reconnection rate. This is the most remarkable difference between the non-relativistic and relativistic reconnections. Since the outflow velocity is nearly constant at the Alfvén velocity in the non-relativistic reconnection, the reconnection rate is larger for a larger inflow velocity. On the other hand, the outflow velocity is appreciably smaller than the Alfvén velocity for a relativistically hot plasma because of the large inertia (enthalpy). The Ohmic heating rate is larger for a larger reconnection rate. A hot relativistic plasma is hard to be accelerated and tends to be jammed in the diffusion region. Hence the outflow is hotter and slower when the reconnection rate is larger.

Note that this effect is more prominent when the aspect ratio is larger. When the aspect ratio is larger, the outflow is squeezed more and becomes denser and hotter.

The outflow velocity is relativistic only when the outflow is cold and hence the inflow velocity is quite small. Equation (3.2.3) gives us the condition for a relativistic outflow,

$$\beta_{\rm i} \ll \delta/L\,. \tag{3.2.4}$$

Next we derive the condition for the plasma to be relativistically hot, $\alpha_{\rm o} > 1$ in the outflow region. For this purpose, we consider the condition of $\alpha_{\rm o} = 1$, i.e., that the thermal to rest mass energy density is equal to unity. Substituting $\alpha_{\rm o} = 1$ into equations (3.1.15) and (3.1.16), we obtain

$$\sigma_{\rm i} = 2\frac{\gamma_o}{\gamma_i} - 1, \tag{3.2.5}$$

$$2\gamma_{\rm i}^2 \left(2\frac{\gamma_{\rm o}}{\gamma_{\rm i}} - 1\right)\left(\frac{u_{\rm i}L}{u_{\rm o}\delta}\right)^{\frac{1}{3}} - 1 = 0. \tag{3.2.6}$$

Here we assume $\theta_{\rm i} = 0$ and $(\delta/L)^2 \ll 1$. When the inflow is non-relativistic ($\gamma_{\rm i} \simeq 1$) and the outflow is ultra-relativistic ($u_{\rm o} \simeq \gamma_{\rm o}$), equation (3.2.6) has the solution,

$$u_{\rm o} = u_* = \sqrt{\frac{1}{64}\frac{\delta}{L}\frac{1}{\beta_{\rm i}}}. \tag{3.2.7}$$

Substituting equation (3.2.7) into (3.2.5), we obtain

$$\sigma_{\rm i} = \sigma_* = \sqrt{\frac{1}{16}\frac{\delta}{L}\frac{1}{\beta_{\rm i}}} - 1. \tag{3.2.8}$$

This approximation is valid when

$$\beta_{\rm i} < \beta_{i,\rm max} \equiv \frac{1}{64}\frac{\delta}{L}. \tag{3.2.9}$$

As $\sigma_{\rm i}$ increases, $\alpha_{\rm o}$ increases monotonically for fixed $\beta_{\rm i}$, L/δ, and $\theta_{\rm i}$ (see, Fig. 3.2). Thus the outflow is relativistically hot when $\sigma_{\rm i} > \sigma_*$. When $1 < \sigma_{\rm i} < \sigma_*$, the outflow has a relativistic speed ($u_{\rm o} > 1$) while the thermal energy is smaller than the rest mass energy (i.e., cold, $\alpha_{\rm o} < 1$).

Note that the saturated specific momentum is only three times larger than the critical specific momentum of the outflow u_*,

$$u_{\rm o}^{\rm sat} = 2\sqrt{2}u_*. \tag{3.2.10}$$

This indicates that the excess magnetic energy contributes not to further acceleration but to further heating when $\sigma_{\rm i}$ exceeds σ_*.

Next we examine dependence of the outflow velocity on the inflow velocity $u_{\rm i}$. Fig. 3.3 shows $u_{\rm o}$ (thick curves) and $\alpha_{\rm o}$ (thin curves) as a function of $\log u_{\rm i}$ for $\sigma_{\rm i} = 100$, and

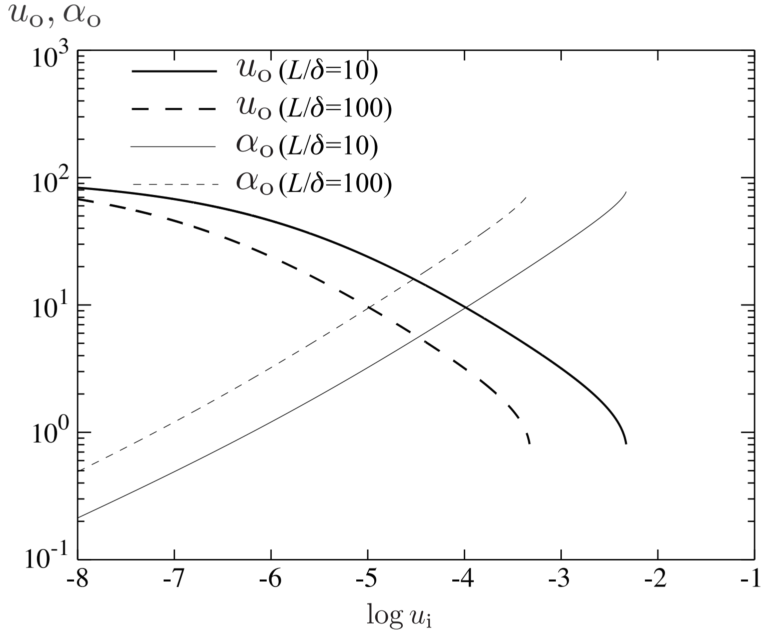

Figure 3.3: Dependence of the specific momentum of the outflow (thick curves) and α_o (thin curves) on the inflow velocity $\log u_i$ for $\sigma_i = 100$, and $\theta_i = 0$. Solid curves denote for $L/\delta = 10$, while dashed curves do for $L/\delta = 100$.

$\theta_i = 0$. The solid curves are for $L/\delta = 10$ while dashed curves are for $L/\delta = 100$. The outflow momentum is larger for a smaller inflow velocity when σ_i, L/δ, and θ_i are fixed. It is saturates at $u_o \simeq \sigma_i + 1$ in the limit of small u_i. The ratio of thermal to rest mass energy densities, α_o, increases monotonically with increasing u_i. This dependence of α_o on u_i is consistent with the discussion below equation (3.2.3).

Note that no solution exists when u_i is larger than a critical value. Equation (3.2.9) gives a rule of thumb for the existence of a solution. When the inflow velocity exceeds the critical value, the outflow is too hot to be accelerated. When the inflow has its maximum speed given by equation (3.2.9), the reconnection rate is given as

$$\frac{\beta_{i,\max}}{\beta_o} \simeq \frac{1}{64}\frac{\delta}{L}, \tag{3.2.11}$$

where we used $\gamma_o \simeq 1$ and $\beta_o \simeq 1$. This result is essentially the same as equation (6) of Lyubarsky (2005). As discussed in the paragraph below equation (3.2.3), the outflow velocity is smaller for a larger reconnection rate in relativistic reconnection ($\sigma_i \gg 1$). The plasma tends to get jammed in the diffusion region and the pressure gradient force is no more efficient ($p_N \simeq p_o$). Thus the results obtained by Lyubarsky (2005) corresponds to the case when the reconnection rate is large.

Note that the flow is roughly incompressible in this limit. Since the inflow and outflow

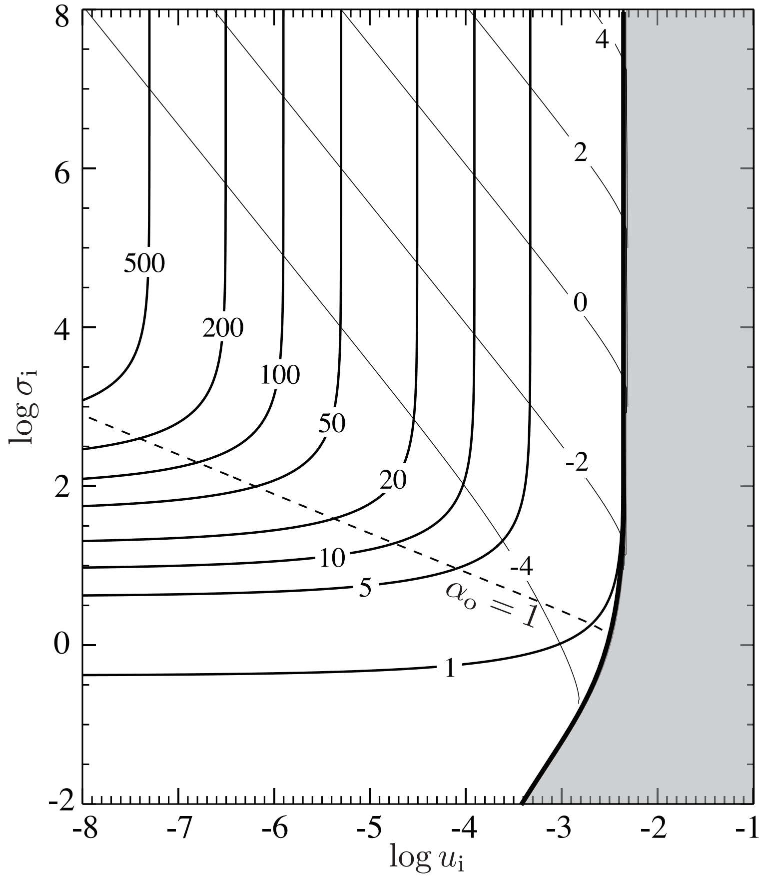

Figure 3.4: The contour plots of specific momentum of the outflow (thick solid curves) and $\log \sigma_{\rm o}$ (thin solid curves) are shown on $\log u_{\rm i}$-$\log \sigma_{\rm i}$ plane for $L/\delta = 10$, and $\theta_{\rm i} = 0$. The dashed curve denotes the contour of $\alpha_{\rm o} = 1$. Above the curve, plasma is relativistically hot in the outflow region. No solution exists in the grey area.

speeds are not ultra-relativistic and the sound speed is close to the light speed, i.e., $c_{\rm cs} \simeq c/\sqrt{3}$, the flow can roughly be treated as incompressible.

When $\beta_{\rm i} \sim \beta_{\rm i,max}$, the Ohm's law can approximately be written as

$$\boldsymbol{E} = \eta \boldsymbol{j}, \tag{3.2.12}$$

since the inflow and outflow speeds are non-relativistic or semi-relativistic at most. Here, η is the electric resistivity. The Z-component of the electric field outside the dissipation region is evaluated from the MHD condition,

$$E_z = \beta_{\rm i} B_{\rm i}. \tag{3.2.13}$$

The current density inside the dissipation region is evaluated as

$$j_{\rm z} \simeq \frac{c B_{\rm i}}{4\pi\delta}, \tag{3.2.14}$$

from the Ampere's law. Since the Z-component of the electric field is uniform in a steady state, we obtain

$$\beta_{\rm i} \simeq \frac{1}{8} R_{\rm M}^{-1/2}, \tag{3.2.15}$$

from equations (3.2.9), (3.2.12), (3.2.13), and (3.2.14). Here $R_{\rm M}$ is the magnetic Reynolds number defined by

$$R_{\rm M} = \frac{4\pi L}{\eta c}. \tag{3.2.16}$$

Equation (3.2.15) is essentially the same as (8) of Lyubarsky (2005).

Fig. 3.4 shows the specific momentum of the outflow (thick solid curves) and $\log \sigma_{\rm o}$ (thin solid curves) on $\log u_{\rm i} - \log \sigma_{\rm i}$ plane for $L/\delta = 10$, and $\theta_{\rm i} = 0$. The dashed curve denotes the contour of $\alpha_{\rm o} = 1$. Above the curve, plasma is relativistically hot in the outflow region. No solution exists in the grey area. When the outflow is cold, the specific momentum approaches $u_{\rm o} \simeq \sigma_{\rm i} + 1$ in the limit of small $u_{\rm i}$, as shown in equation (3.2.1). When the outflow is hot, the specific momentum saturates at $u^{\rm sat}$ in the limit of large $\sigma_{\rm i}$. Then the magnetization parameter in the outflow region can be estimated as

$$\frac{\sigma_{\rm o}}{\sigma_{\rm i}} \simeq 2\sqrt{2}\beta_{\rm i}^{\frac{3}{2}} \left(\frac{\delta}{L}\right)^{\frac{1}{2}}, \tag{3.2.17}$$

from equation (3.1.14) and (3.2.3). Here we assume $\gamma_{\rm i} \simeq 1$. The magnetic energy is converted to the plasma energy more efficiently when $\beta_{\rm i}$ is smaller and L/δ is larger.

3.2.2 Case of $B_{\rm z} \neq 0$ ($\theta_{\rm i} \neq 0$)

Next we consider the effects of the guide field ($B_{\rm z}$). The specific momentum of the outflow is shown as a function of $\sigma_{\rm i}$ for $\beta_{\rm i} = 10^{-6}$ and $L/\delta = 10$ in Fig. 3.5. The thick solid curve is for the case without guide field, $\theta_{\rm i} = 0$, while thin solid, dashed, and dot-dashed ones are for $\theta_{\rm i} = \pi/8$, $\pi/4$, and $3\pi/8$, respectively. As in the case of $B_{\rm z} = 0$, the specific momentum of the outflow is larger for a larger $\sigma_{\rm i}$ when $\beta_{\rm i}$, L/δ, and f are fixed. It saturates in the limit of large $\sigma_{\rm i}$. The saturation value of the specific momentum increases with $\theta_{\rm i}$, although it does not depend on $\theta_{\rm i}$ when $\sigma_{\rm i}$ is small. The saturation value of the specific momentum $u^{\rm sat}(\theta_{\rm i})$ can be obtained as

$$u_{\rm o}^{\rm sat}(\theta_{\rm i}) = \frac{1}{\cos\theta_{\rm i}^3}\sqrt{\frac{1}{8}\frac{\delta}{L}\frac{1}{\beta_{\rm i}}} \equiv \frac{u_{\rm o}^{\rm sat}(\theta_{\rm i}=0)}{\cos^3\theta_{\rm i}}. \tag{3.2.18}$$

from equation (3.1.15) and (3.1.16) by taking $\alpha_{\rm o} \gg 1, B_{z,{\rm o}}^2/(4\pi\rho_{\rm o}c^2\gamma_{\rm o}^2)$ and taking $u_{\rm i} \simeq \beta_{\rm i}$ and $u_{\rm o} \simeq \gamma_{\rm i}$. The outflow velocity is larger for a larger $\theta_{\rm i}$. This effect is due to expansion

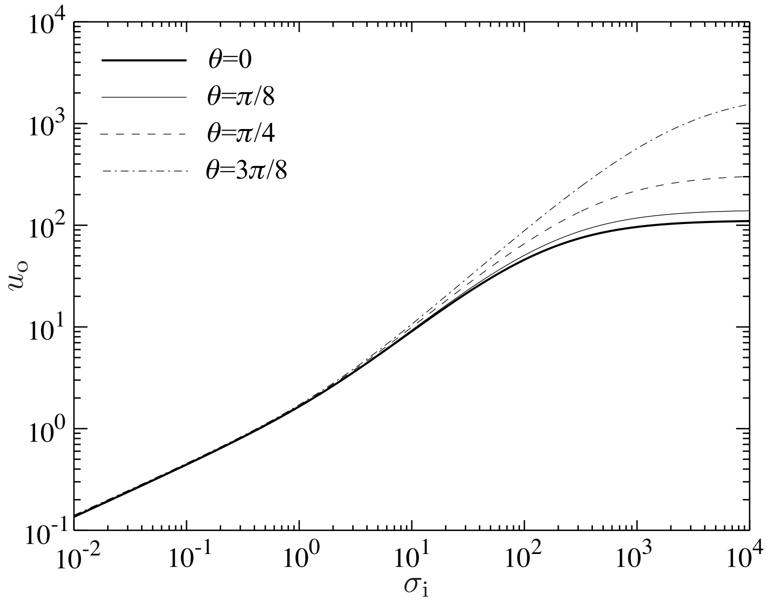

Figure 3.5: Dependence of the specific momentum of the outflow on σ_i and the inclination angle θ_i for $\beta_\mathrm{i} = 10^{-6}$ and $L/\delta = 10$. The thick solid curve is for $\theta_\mathrm{i} = 0$, while thin solid, dashed, and dot-dashed ones are for $\theta_\mathrm{i} = \pi/8$, $\pi/4$, and $3\pi/8$, respectively.

of the plasma during the reconnection; the magnetic energy of the guide field is used for acceleration through the magnetic pressure in our model. If we assume incompressibility, this effect will disappear. For a larger B_z, plasma can be treated as incompressible since fast magnetosonic wave speed exceeds the plasma bulk speed.

3.3 Summary & Discussions

We extended the Sweet-Parker type steady state magnetic reconnection into relativistic plasma. Our treatment is based on the conservation laws of mass and energy. We employed the entropy conservation between the neutral point and the outflow region to study the effects of the pressure gradient force and the decreasing in the inertia.

Our results can be summarized as follows,

- non-relativistic case ($\sigma_\mathrm{i} < 1$): $v_\mathrm{o} \sim \sqrt{2} v_\mathrm{A}$
- cold plasma ($1 < \sigma_\mathrm{i} < \sigma_*$): $u_\mathrm{o} \sim \sigma_\mathrm{i} + 1$
- hot plasma ($\sigma_\mathrm{i} > \sigma_*$): $u_\mathrm{o} \sim \beta_\mathrm{i}^{-\frac{1}{2}} \left(\frac{\delta}{L}\right)^{\frac{1}{2}}$

When the plasma is cold, the specific momentum of the outflow is given by $u_{\rm o} \sim \sigma_{\rm i} + 1$. This result coincides with equation (32) of Lyutikov & Uzdensky (2003). However, in contrast to their results, the reconnection rate should be much smaller to realize the cold outflow for large $\sigma_{\rm i}$. This conflict comes from the neglect of the thermal pressure of the outflow in their treatment. When one neglects the thermal pressure in the outflow region, the outflow is always cold and the faster reconnection could be realized. This assumption is not valid for a relativistic magnetic reconnection since a fast reconnection heats the plasma. Increase in the inertia due to the thermalization results in a slower outflow when $\sigma_{\rm i} \gg 1$. When the plasma is hot, the specific momentum of the outflow approaches a certain maximum value given by equation (3.2.3). The outflow speed becomes slower for a larger reconnection rate. The result by Lyubarsky (2005) that the outflow speed is sub-relativistic in the relativistically hot outflow can be reproduced when the reconnection rate is large.

We showed that the outflow is relativistically hot when $\sigma_{\rm i} > \sigma_*$. Can this thermal energy be converted to kinetic energy? Fig. 3.2 shows that the outflow speed increases when the aspect ratio L/δ decreases. The aspect ratio is taken as a free parameter in our model as well as in the conventional Sweet-Parker model. When the thermal energy inside the dissipation region becomes larger than that of the rest mass, the dissipation region expands in Y-direction by the excess thermal pressure. Then the aspect ratio becomes smaller. This leads to the decrease in plasma temperature, i.e., the decrease in the inertia. Zenitani & Hesse (2008a) showed that the magnetic reconnection is self-regulated so as to increase the reconnection rate by changing its aspect ratio. Since the energy flux flowing into the dissipation region is fixed in steady state and the momentum is conserved, the outflow velocity becomes larger (see, equation (3.2.3)). Another solution to convert the thermal energy to kinetic energy is to spread out the relativistically hot plasma adiabatically into a fan in the outflow region (Swisdak et al. 2008). This also leads to decrease in temperature, which enables the plasma to be accelerated.

In our treatment, we assumed that the plasma density around the neutral point is equal to that of the inflow (see, equation (3.1.9)). This assumption is plausible since the inflow velocity is much less than the fast magnetosonic wave speed of the inflow when $L/\delta \gg 1$ (see equation (3.2.9)) and hence the compression is weak. However, Zenitani & Hesse (2008a) showed that the plasma density inside the current sheet is a few times larger than that of the inflow. Thus we simply relax this condition as

$$\rho_{\rm N} = g\rho_{\rm i}, \tag{3.3.1}$$

where g is taken as a free parameter. By replacing equation (3.1.9) by (3.3.1), $\alpha_{\rm o}$ is rewritten as

$$\alpha_{\rm o} = \frac{\Gamma\gamma_{\rm i}^2}{2(\Gamma-1)g^\Gamma}\sigma_{\rm i} x^{\Gamma-1}\cos^2\theta_{\rm i}, \tag{3.3.2}$$

This equation indicates that the inertia is smaller for a larger g. Since the plasma entropy is smaller for a larger plasma density, plasma enthalpy also becomes smaller. This leads to the decrease in the inertia. By using relation (3.3.1), the saturated velocity (3.2.3) is replaced by

$$u^{\rm sat}(g) = \frac{g^2}{\cos^3\theta_{\rm i}}\sqrt{\frac{1}{8}\frac{\delta}{L}\frac{1}{\beta_{\rm i}}} \equiv g^2 u^{\rm sat}(g=1). \tag{3.3.3}$$

Here we took $\Gamma = 4/3$. Thus the outflow velocity is larger for a larger g.

Our treatment is based on the relativistic MHD, but it is interesting to compare our results with recent numerical works on particle dynamics in relativistic reconnection (Zenitani & Hoshino 2001; Jaroschek et al. 2004; Zenitani & Hoshino 2007; Karlický 2008; Lyubarsky & Liverts 2008). Zenitani & Hoshino (2007) showed that the evolution of the relativistic magnetic reconnection looks like the Sweet-Parker type. In their paper, the inflow and the outflow maximum velocity is about $0.4c$ and $0.9c$, respectively when $\sigma_i \simeq 40$. The aspect ratio L/δ is about 10. The inflow speed is still non-relativistic and the outflow velocity is much smaller than the inflow Alfvén velocity. Interestingly, the inflow velocity $\beta_{\rm i}$ is of order the inverse of the aspect ratio, δ/L (note that Zenitani & Hoshino (2007) showed the maximum inflow velocity). This result may indicate that the magnetic energy flowing into the dissipation region is mainly converted to the thermal energy. Then the outflow can not be accelerated up to ultra-relativistic speed (see, equation (3.2.3)). But we have to take care the effect of the non-thermal particles which are mainly generated around the X-point of the magnetic reconnection. Some part of the magnetic energy is carried away by the non-thermal particles and this effect can not be taken into account by MHD.

Chapter 4

Numerical Study of the Relativistic Magnetic Reconnection

In the previous chapter, the possibility of the relativistic outflow from the relativistic magnetic reconnection is discussed. In this chapter, we study the relativistic magnetic reconnection by using Particle-In-Cell (PIC) code.

4.1 Simulation Methods

4.1.1 Basic Equations

The simulation is performed by using 2-dimensional relativistic PIC code (see Birdsall & Langdon 2001, for details). In this code, we solve the following basic equations;

$$\frac{d}{dt}(m_i \gamma_i \boldsymbol{v}_i) = q_i \left(\boldsymbol{E} + \frac{\boldsymbol{v}_i}{c} \times \boldsymbol{B} \right), \tag{4.1.1}$$

$$\frac{d\boldsymbol{x}_i}{dt} = \boldsymbol{v}_i, \tag{4.1.2}$$

$$\frac{1}{c}\frac{\partial \boldsymbol{B}}{\partial t} = -\nabla \times \boldsymbol{E}, \tag{4.1.3}$$

$$\frac{1}{c}\frac{\partial \boldsymbol{E}}{\partial t} = \nabla \times \boldsymbol{B} - \frac{4\pi}{c}\boldsymbol{j}, \tag{4.1.4}$$

$$\nabla \cdot \boldsymbol{E} = 4\pi \rho_e, \tag{4.1.5}$$

$$\nabla \cdot \boldsymbol{B} = 0, \tag{4.1.6}$$

where $\boldsymbol{x}_i$, $\boldsymbol{v}_i$, γ_i, m_i, and q_i are the position, velocity, Lorentz factor, rest mass, and the charge for the ith particle and $\boldsymbol{E}$, $\boldsymbol{B}$, ρ_e, $\boldsymbol{j}$ are the electric field, magnetic field, charge density, and the charge current, respectively.

The particle velocities and positions are updated by solving equations (4.1.1) and (4.1.2). The current density ρ_e and the charge current $\boldsymbol{j}$ are then calculated by scattering the particle information on the grid by

$$\rho_e(\boldsymbol{X}) = \sum_i q_i S(\boldsymbol{x}_i - \boldsymbol{X}), \tag{4.1.7}$$

$$\boldsymbol{j}(\boldsymbol{X}) = \sum_i q_i \boldsymbol{v}_i S(\boldsymbol{x}_i - \boldsymbol{X}), \tag{4.1.8}$$

where Σ denotes the sum of all particles and $S(x)$ is a shape factor. Equations (4.1.1) is solved by a conventional Buneman-Borris method (see Birdsall & Langdon 2001), and the electromagnetic fields are solved implicitly by using Incomplete Cholesky Conjugate Gradient (ICCG) method.

Since the particle information is scattered to grids by using the shape factor S following equations (4.1.7) and (4.1.8), the charge conservation equation is not satisfied exactly and the condition of constraint (4.1.5) is thus sometimes violated. To avoid this, we introduce a scalar function $\delta\phi$ defined as

$$\boldsymbol{E} = \boldsymbol{E}' - \nabla(\delta\phi), \tag{4.1.9}$$

where $\boldsymbol{E}'$ is the electric field obtained by solving equation (4.1.4), and $\boldsymbol{E}$ is the corrected electric field which satisfies equation (4.1.5). By taking the divergence of equation (4.1.9), we obtain

$$\nabla^2\phi = \nabla \cdot \boldsymbol{E}' - 4\pi\rho_e. \tag{4.1.10}$$

By solving the Poisson equation (4.1.10), the corrected electric field $\boldsymbol{E}$ is obtained from equation (4.1.9). The constraint (4.1.6) is satisfied by using the staggered mesh. By using the staggered mesh and leap-frog method, we solve equations (4.1.1)-(4.1.8) with second-order accuracy.

4.1.2 Model

We consider the collisionless pair plasma. As the initial condition, we use a relativistic Harris configuration which satisfies the Vlasov equation (Harris 1962; Kirk & Skjæraasen 2003). The magnetic fields are given by

$$\boldsymbol{B} = B_0 \tanh\left(\frac{y}{\lambda}\right) \boldsymbol{e}_x. \tag{4.1.11}$$

The particle distribution function is given by

$$f_s = f_{s,\mathrm{cs}} + f_{s,\mathrm{bg}}, \tag{4.1.12}$$

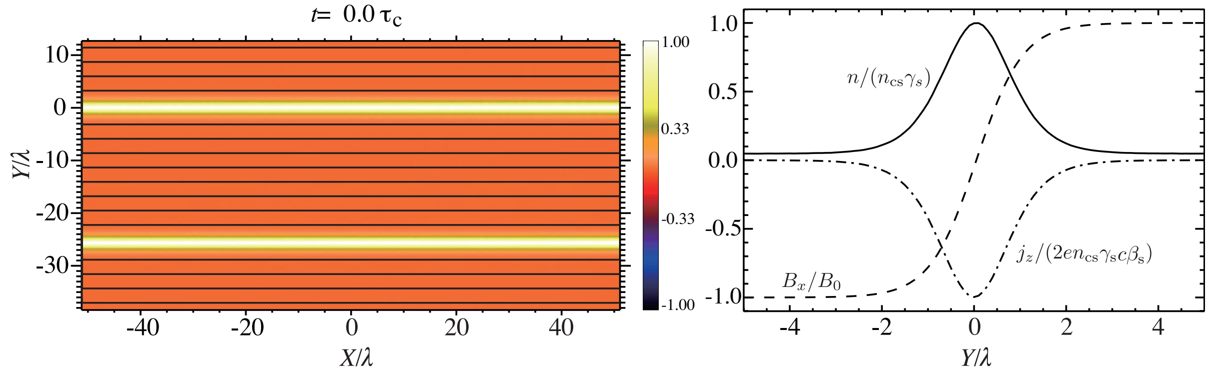

Figure 4.1: Left: Color shows the plasma density and black curves show the magnetic field lines for the whole simulation box at $t = 0$. Right: Plasma density (solid curve), B_x (dashed curve) and j_z (dash-dotted curve) across the current sheet. The plasma density and the charge current are normalized by those at $Y = 0$ of the initial state and B_x is normalized by B_0.

where the subscript s denotes the particle species, and the subscripts 'cs' and 'bg' denote the plasma in the current sheet and background plasmas, respectively. The functions $f_{s,\rm cs}$ and $f_{s,\rm bg}$ are given by

$$f_{s,\rm cs} = \frac{n_{\rm cs}}{4\pi m^2 ck_B T_{\rm cs} K_2(mc^2/k_B T_{\rm cs})} \frac{1}{\cosh^2(y/\lambda)} \exp\left[-\frac{\gamma_s(\epsilon - \beta_s mc^2 u_z)}{k_B T_{\rm cs}}\right], \tag{4.1.13}$$

$$f_{s,\rm bg} = \frac{n_{\rm bg}}{4\pi m^2 ck_B T_{\rm bg} K_2(mc^2/k_B T_{\rm bg})} \exp\left[-\frac{\epsilon}{k_B T_{\rm bg}}\right]. \tag{4.1.14}$$

where n, ϵ, $\boldsymbol{u}$, β_s, γ_s, k_B, T, K_2, are the plasma proper density, the particle energy, the particle four velocity, the drift velocity of the current sheet in unit of c, the Lorentz factor of the drift velocity, the Boltzmann constant, the plasma temperature, and the modified Bessel function of the second kind, respectively. Thickness of the current sheet is denoted by λ.

The number of grids is (1024, 512) on the $X - Y$ plane. The grid size is normalized by λ and the time step is normalized by the light crossing time $\tau_c \equiv \lambda/c$. We used 10 grids on λ. The boundary condition is periodic in both directions. The boundaries are located at $X = -51.2\lambda, 51.2\lambda$ and $Y = -38.4\lambda,\ 12.8\lambda$ (see Fig. 4.1). Since the magnetic field lines change their directions in the current sheets, we set two current sheets at $Y = -25.6\lambda$ and $Y = 0$ (see Fig. 4.1). We hereafter concentrate on the upper current sheet $Y = 0$.

To trigger the magnetic reconnection, we imposed the Z component of the external electric field around $(X, Y) = (0, \pm 3)$. The maximum amplitude is $0.3V_A/c$, where V_A

Run	$k_B T_{\rm cs}/mc^2$	$\alpha_{\rm i}$	$\sigma_{\rm i}$
R005	0.05	0.12	1.91
R01	0.1	0.24	3.82
R05	0.5	1.2	19.1
R1	1.0	2.4	38.1
R4	4.0	9.6	152
R8	8.0	19.2	305
R16	16.0	38.4	611

Table 4.1: Initial parameters $T_{\rm cs}$, $\alpha_{\rm i}$, and $\sigma_{\rm i}$ for each run are summarized.

is the typical Aflvén velocity. The electric field is imposed for the duration of $t_{\rm trig} = 10\lambda/V_A \sim 10 - 15\tau_c$, which is much shorter than the total simulation time and the time before the onset of the magnetic reconnection (Zenitani & Hoshino 2007).

From the pressure balance across the current sheet, we obtain

$$\frac{B_0^2}{8\pi} = 2n_{\rm cs}T_{\rm cs}. \tag{4.1.15}$$

The magnetization parameter of the background plasma (inflow region) $\sigma_{\rm i}$ is then given by

$$\sigma_{\rm i} \equiv \frac{B_0^2}{4\pi(2n_{\rm bg})mc^2\gamma_{\rm i}^2} = 2\frac{T_{\rm cs}}{mc^2}\frac{n_{\rm cs}}{n_{\rm bg}}. \tag{4.1.16}$$

Here we assume $\gamma_{\rm i} = 1$. Since we are interested in the possibility of the relativistic outflow from the relativistic magnetic reconnection (i.e., $\sigma_{\rm i} >> 1$), we study the $\sigma_{\rm i}$ dependence of the outflow velocity by changing the plasma temperature inside the current sheet $T_{\rm cs}$. The number density inside the current sheet and the background plasma temperature are fixed at $n_{\rm cs}\gamma_s = 1000$ pairs and $T_{\rm bg} = 0.2T_{\rm cs}$ in all simulations, respectively. The density ratio $n_{\rm bg}/(n_{\rm cs}\gamma_s)$ is fixed at 0.05 to trigger the fast reconnection. We study the case of $k_B T_{\rm cs}/mc^2 = (0.05,\ 0.1,\ 0.5,\ 1, 4\ ,\ 8,\ 16)$, which corresponds to $\sigma_{\rm i} =$ (1.91, 3.82, 19.1, 38.2, 153, 305, 611), and $\alpha_{\rm i} =$ (0.12, 0.24, 1.2, 2.4, 9.6, 19.2, 38.4), respectively. Here we assume $\Gamma = 4/3$. The model and their parameters are summarized in Table 4.1.

The total energy increases with time by 0.28% at $t = t_{\rm trig}$ since we imposed the triggering electric fields. It is conserved within the error of 0.3% until the end of the simulation $t = 150\tau_c$.

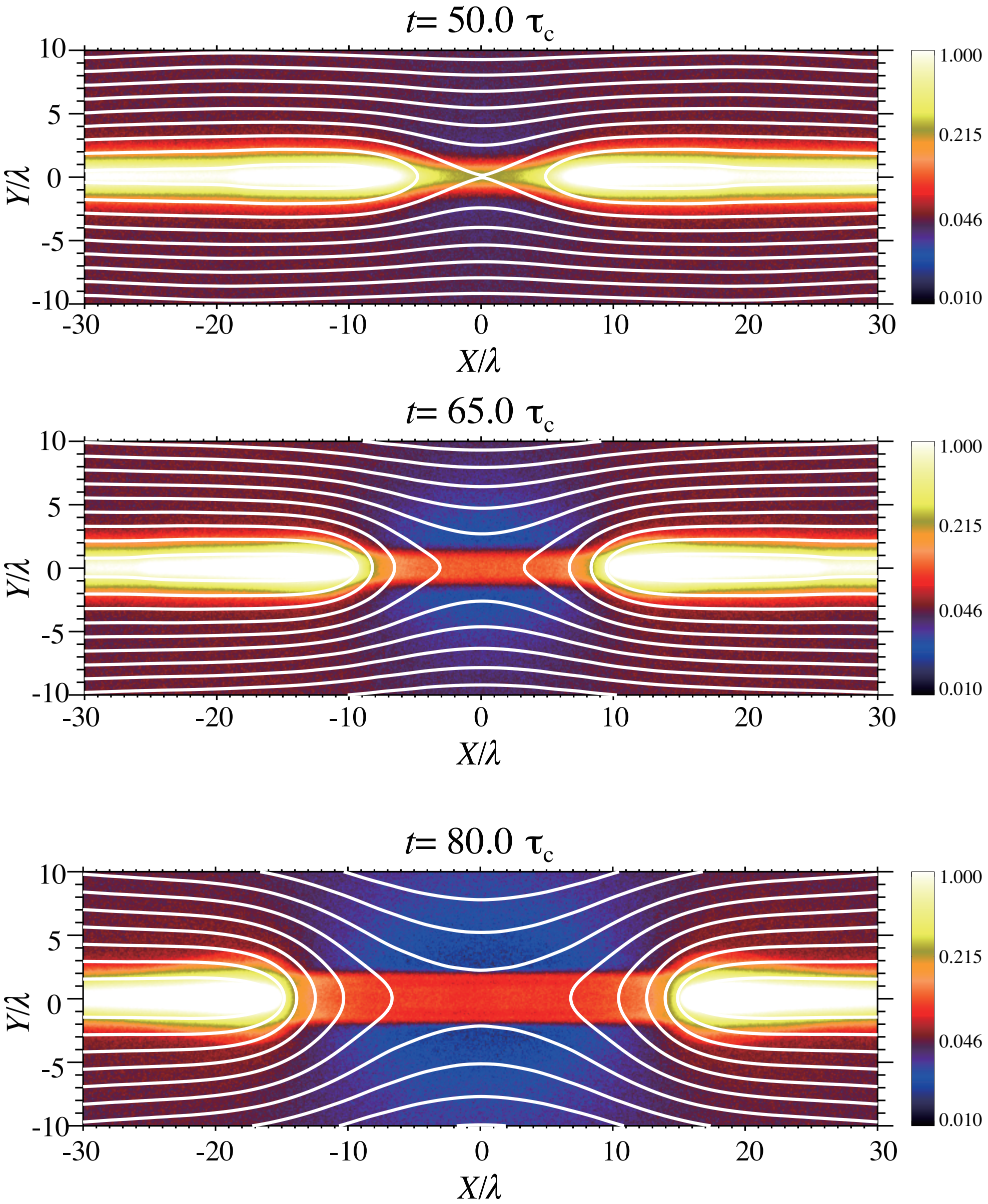

Figure 4.2: Contour plots of the plasma density $n/(2\gamma_s n_{\rm cs})$ (color) and the magnetic field lines (white curves) for R01 at $t/\tau_c = 50, 65, 80$ from top to bottom, respectively.

4.2 Simulation Results

4.2.1 Overview of the Simulation Results

Fig. 4.2 shows the snapshot of a part of the simulation box for R01 at $t/\tau_c = 50, 65, 80$ from top to bottom, respectively. The color contours show the plasma density $n/(2\gamma_s n_{\rm cs})$, while the white curves do the magnetic field lines. The magnetization parameter in the inflow region is ~ 3.8. At the initial state, magnetic field lines are in $+X$ direction in $Y > 0$, and in $-X$ direction in $Y < 0$. By imposing the triggering electric fields, the background plasma flows toward the $(X, Y) = (0, 0)$ with the drift velocity $\boldsymbol{v}_d = c(\boldsymbol{E} \times \boldsymbol{B})/B^2$. The plasma flow results in the onset of the magnetic reconnection. After onset of the magnetic reconnection, the magnetic field lines reconnect and form $X-$type region around $(X, Y) = (0, 0)$. Particles flowing into the $X-$point are accelerated by induced electric fields E_z. Fig. 4.3 shows the $-(E_z - B)/B_0$ at $t/\tau_c = 95$, where B is the magnetic field strength. The electric fields are induced around the X point, whose strength is larger than the local magnetic field strength, $E_z > B$. The accelerated particles evacuate to $\pm X$ directions by deflecting their orbits due to the magnetic fields B_y and form bipolar plasma jets. The magnetic fields are swept up in $\pm X$ directions and the strong electric fields are induced by $\boldsymbol{E} = -\boldsymbol{v} \times \boldsymbol{B}/c$.

The structure of the magnetic reconnection is close to the Sweet-Parker type, which does not have shocks (Zenitani & Hoshino 2007). The maximum outflow velocity $v_{\rm max} \simeq 0.56c$ is less than the Alfvén velocity of the inflow $V_A = 0.87c$.

4.2.2 Effect of the Thermal Pressure of the Inflow

In Chapter 3, we ignored the effects of the thermal pressure in the inflow region. We include this effect and derive the condition for the relativistic outflow in this subsection.

By including the thermal energy of the inflow in the energy conservation equation (3.1.3), we obtain

$$\rho_{\rm i} c^2 \gamma_{\rm i}^2 \beta_{\rm i} L \left(1 + \alpha_{\rm i} + \sigma_{\rm i}\right) = \rho_{\rm o} c^2 \gamma_{\rm o}^2 \beta_{\rm o} \delta \left(1 + \alpha_{\rm o} + \sigma_{\rm o}\right), \tag{4.2.1}$$

The pressure balance condition given by equation (3.0.1) can be rewritten by including the thermal energy of the inflow as

$$p_{\rm N} = p_{\rm i} + \frac{B_{\rm i}^2}{8\pi}. \tag{4.2.2}$$

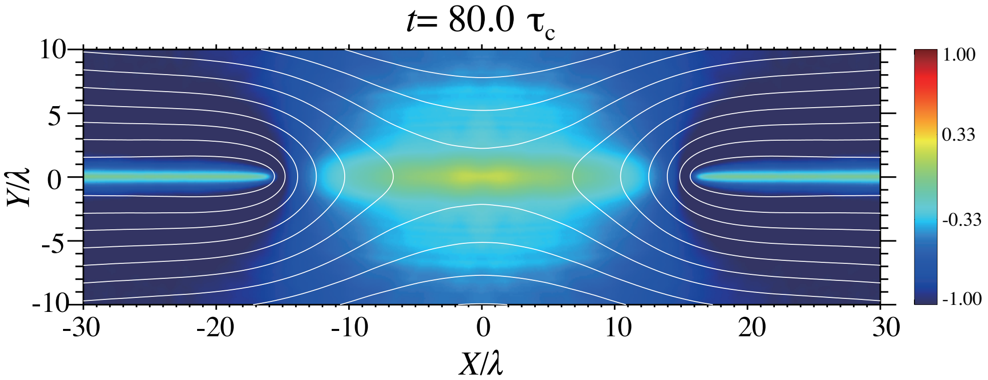

Figure 4.3: Color contours show $-(E_z - B)/B_0$ and the white curves show the magnetic field lines for R01 at $t/\tau_c = 80$.

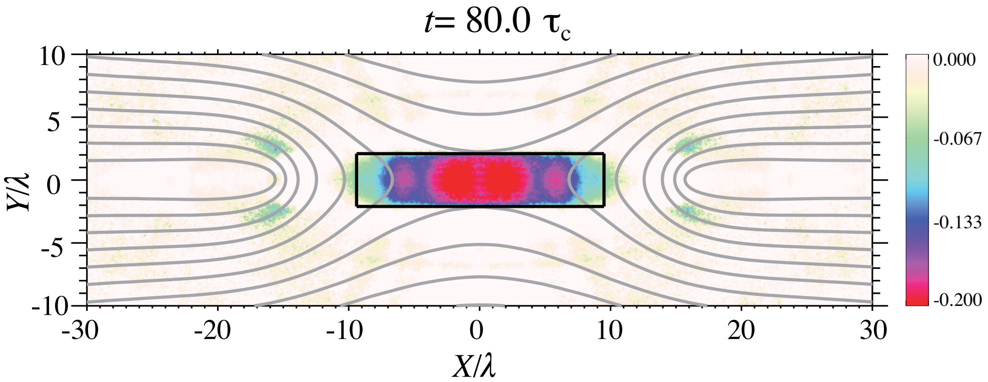

Figure 4.4: Grey curves show the magnetic field lines and color contours show $(\boldsymbol{E} + \boldsymbol{v} \times \boldsymbol{B}/c)_z/B_0$ at $t = 80\tau_c$ for R01. Black rectangular shows the diffusion region.

By using these equations, the Bernoulli's theorem given by equation (3.1.6) can be rewritten as

$$\left(1+\alpha_{\mathrm{i}}+\sigma_{\mathrm{i}}\right)\gamma_{\mathrm{i}}=\left(1+\alpha_{\mathrm{o}}+\sigma_{\mathrm{o}}\right)\gamma_{\mathrm{o}}. \tag{4.2.3}$$

where α_{o} is given by

$$\alpha_{\mathrm{o}}=\frac{1}{g^{\Gamma}}\left(\frac{1}{2}\frac{\Gamma}{\Gamma-1}\gamma_{\mathrm{i}}^{2}\sigma_{\mathrm{i}}+\alpha_{\mathrm{i}}\right)\left(\frac{u_{\mathrm{i}}L}{u_{\mathrm{o}}\delta}\right)^{\Gamma-1}, \tag{4.2.4}$$

and σ_{o} is given by equation (3.1.14). Here, g is the density ratio between the inflow region and the neutral point defined in equation (3.3.1).

By taking approximations of α_{i}, $\sigma_{\mathrm{i}} >> 1$, $(\delta/L)^2 << 1$, $\gamma_{\mathrm{i}} \simeq 1$, and $u_{\mathrm{o}} \simeq \gamma_{\mathrm{o}}$, we obtain

$$u_{\mathrm{o}}\simeq g^{2}\sqrt{\left(\frac{\alpha_{\mathrm{i}}+\sigma_{\mathrm{i}}}{\alpha_{\mathrm{i}}+2\sigma_{\mathrm{i}}}\right)^{3}\frac{\delta}{L}\frac{1}{\beta_{\mathrm{i}}}}. \tag{4.2.5}$$

When $\alpha_{\mathrm{i}}=0$, equation (4.2.5) reduces to equation (3.2.3). The condition for the relativistic outflow from the magnetic reconnection is given by

$$\beta_{\mathrm{i}}<<\frac{\delta}{L}\left(\frac{\alpha_{\mathrm{i}}+\sigma_{\mathrm{i}}}{\alpha_{\mathrm{i}}+2\sigma_{\mathrm{i}}}\right)^{3}\sim\frac{\delta}{L}. \tag{4.2.6}$$

4.2.3 Comparison between the Simulation Results and MHD Analysis

Before comparing the results between each run, we define the size of the current sheet, e.g., L and δ. Color contours in Fig. 4.4 shows $(\boldsymbol{E}+\boldsymbol{v}\times\boldsymbol{B}/c)/B_0$ and curves show the magnetic field lines. MHD condition is violated around the X-point. The shape of the diffusion region is almost rectangular. We approximate the diffusion region as a rectangle (i.e., shown in Fig. 4.4). The size of the diffusion region L and δ are then determined.

We should determine the time to compare each run since we could not manipulate the time at which magnetic reconnection takes place. For this purpose, we specify the points where $B_y(x, y=0)$ is maximum or minimum at $Y=0$. The referenced time is determined when the length between these two points is 30λ. Fig. 4.5 shows the distribution of $B_y(x, y=0)$ at $t=80\tau_c$ for R01.

Fig. 4.6 shows the σ_{i} dependence of the maximum outflow four velocity (crosses) and Alfvén four velocity of the inflow (diamonds). The outflow four velocity is averaged over $|Y|/\lambda \leq 0.3$ and the time is determined by the above procedure. For a smaller σ_{i} ($\lesssim$ a few × 10), the outflow four velocity increases with σ_{i}. For a larger σ_{i}, the outflow

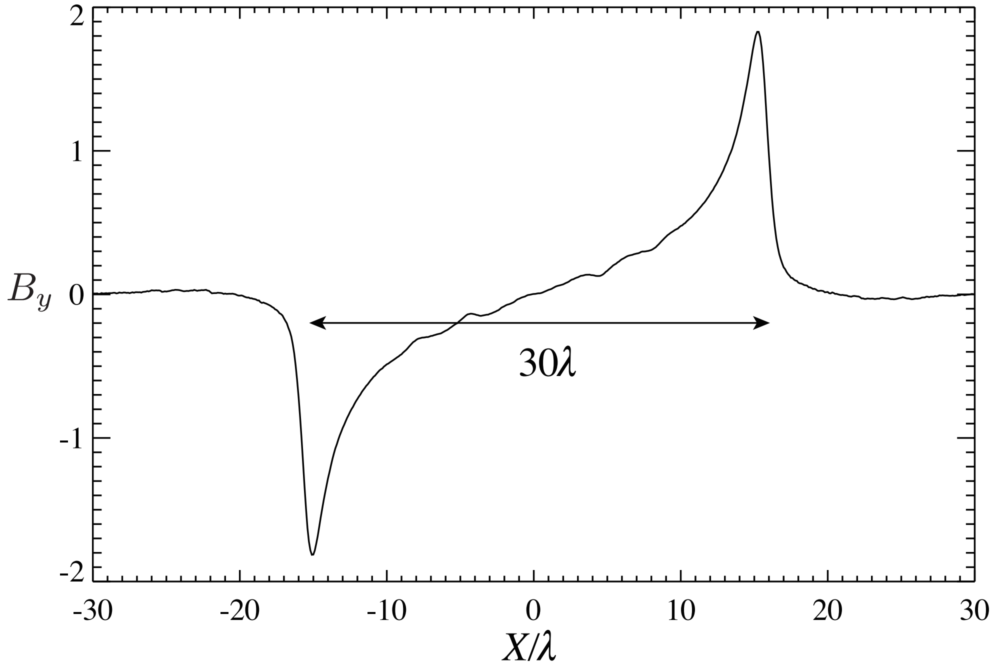

Figure 4.5: The distribution of $B_y(x, y = 0)$ in X direction at $t = 80\tau_c$ for R01.

velocity converges to the saturation value. It is smaller than the Alfvén velocity. The difference between the two velocities is larger for the larger $\sigma_{\rm i}$ but it converges to the certain value.

Fig. 4.7 shows the $\sigma_{\rm i}$ dependence of the maximum inflow velocity $\beta_{\rm i}$ (crosses), the aspect ratio of the diffusion region (triangles), and $\beta_{\rm i} L/\delta$ (diamonds). The condition for the relativistic outflow from the magnetic reconnection is given by equation (4.2.6) which reduces to $\beta_{\rm i} << \delta/L$ in our simulations. In our simulations, the maximum inflow velocity and the aspect ratio are $v_{\rm i} \sim 0.2 - 0.7c$, and $L/\delta \sim 2 - 8$, respectively. They increase with $\sigma_{\rm i}$. Since the condition $\beta_{\rm i} \ll \delta/L$ is not satisfied, the outflow velocity is only mildly relativistic as predicted from the MHD analysis.

Next, we estimate the thermal enthalpy inside the current sheet. The simple method to estimate the thermal energy is to compare the energy momentum tensor

$$T^{\mu\nu} = \int \frac{d^3\boldsymbol{p}}{\epsilon}\, p^\mu p^\nu f(x,p), \tag{4.2.7}$$

where f is the particle distribution function. We take an average and normalize it by the rest mass energy inside the current sheet as $\int d^3x\ T^{\mu\nu} / \int d^3x d^3p\ f$. Fig. 4.8 shows the $\sigma_{\rm i}$ dependence of the diagonal terms of the normalized energy momentum tensor, T_{xx} (crosses), T_{yy} (diamonds), and T_{zz} (triangle) for electrons. Off diagonal terms can be

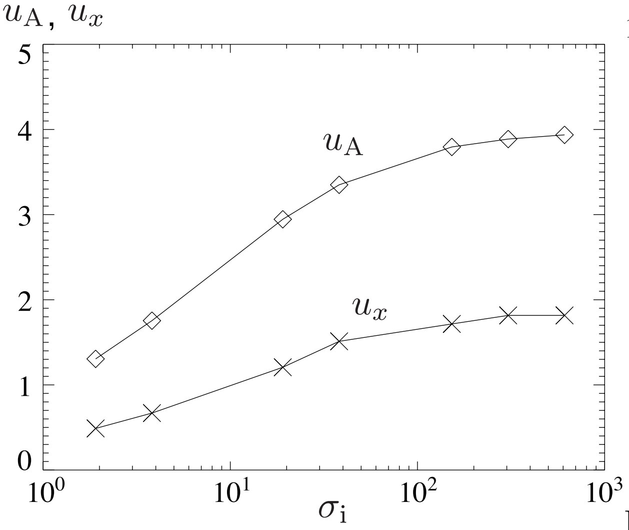

Figure 4.6: σ_i dependence of the outflow four velocity (crosses) and Alfvén four velocity (diamonds).

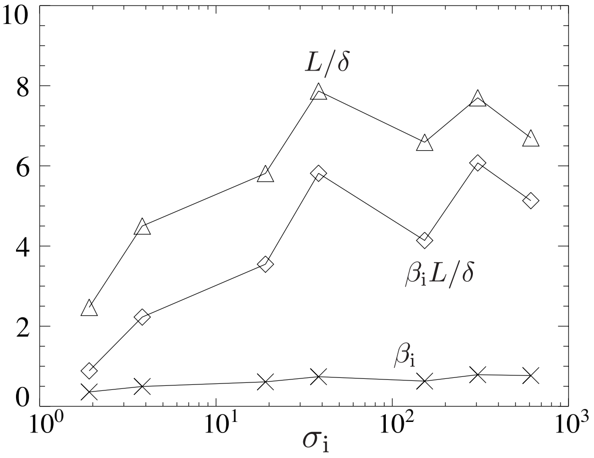

Figure 4.7: σ_i dependence of the maximum inflow velocity in unit of c (crosses), aspect ratio of the current sheet (triangles), and $\beta_i L/\delta$ (diamonds).

ignored compared to the diagonal terms. Inside the current sheet, T_{zz} dominates other terms. All the diagonal terms linearly increase with σ_i. This indicates that the thermal energy increases with σ_i as predicted by the MHD theory.

Note that the pressure tensor given in equation (4.2.7) is evaluated in the observer frame. For larger σ_i, the plasma speed inside the current sheet v_z becomes larger since $4\pi(2nev_z)/c \sim (\nabla \times \boldsymbol{B}_z)$, and we may overestimate the enthalpy. We thus perform the Lorentz transformation $T'^{\mu\nu} = \Lambda^\mu_\alpha \Lambda^\nu_\beta T^{\alpha\beta}$, where Λ^α_β is the transformation matrix in Z direction. To determine the transformation matrix, we calculate the average velocity v_z inside the current sheet. Squares in Fig. 4.8 show T'_{zz} for electrons normalized by the rest mass energy inside the current sheet. Other diagonal terms do not change significantly since we perform the Lorentz transformation in the Z direction. The off-diagonal terms can be ignored compared to the diagonal terms.

Since we performed the Lorentz transformation only in the Z direction, T_{xx} is slightly larger than T'_{zz} in the comoving frame, but the ZZ component is still dominant. T'_{zz} increases with σ_i, consistent with the result of the MHD analysis.

Note that T'_{zz} is larger than unity at $\sigma_i \sim 20$. It coincides with σ_i where the outflow velocity converges to the saturation value. It can be explained by that the outflow cannot be accelerated due to the increase of the enthalpy predicted by the MHD analysis by Lyubarsky (2005) and by ourselves.

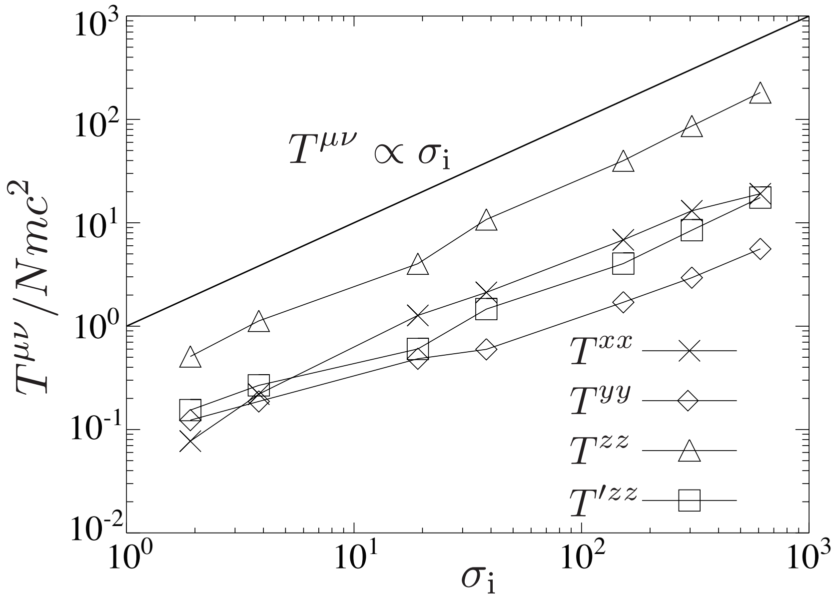

Figure 4.8: σ_i dependence of the diagonal term of the normalized energy momentum tensor, T_{xx} (crosses), T_{yy} (diamonds), and T_{zz} (triangles). Squares show the ZZ component of the energy momentum tensor in the comoving frame T'_{zz}. Solid curve shows the relation $T^{\mu\nu} \propto \sigma_\mathrm{i}$.

4.3 Summary & Discussions

We performed 2-dimensional PIC simulations of relativistic magnetic reconnection to study the possibility of the relativistic outflow.

For smaller σ_i, the outflow velocity increases with σ_i, and it converges a certain value below the Alfvén velocity for larger σ_i. The plasma enthalpy linearly increases with σ_i, and exceeds unity when $\sigma_\mathrm{i} \gtrsim 20$. These results are consistent with those from the MHD analysis. The saturation of the outflow velocity can be explained by the increase in the enthalpy.

We showed from the MHD analysis that the inflow velocity as $\sim \delta/L$, and we showed that the inflow velocity $c\delta/L$ given by Lyubarsky (2005) is the maximum of the flow velocity. In our simulation, the inflow velocity is slightly larger than $c\delta/L$. This is because we observed the maximum inflow velocity. When we measure the inflow velocity by taking an average, the obtained inflow velocity will be close to δ/L

In our simulations, the maximum Alfvén four velocity is 3.96 for R16, which is still only mildly relativistic. This comes from the computational limit. To simulate the case for faster Alfvén velocity, we need to simulate the case when the thermal energy of the inflow is small, $T_{\mathrm{bg}} \ll T_{\mathrm{cs}}$. Such a simulation is hard since the Debye length in the inflow region is too small to be resolved.

Chapter 5

Summary and Discussions

In this chapter, we summarize our results and discuss the particle acceleration in expanding magnetic loops. In § 5.1, we summarize the self-similar solutions of the expanding magnetic loops. The possibility of the relativistic outflow from the magnetic reconnection will be discussed in § 5.2. We discuss the particle acceleration in expanding magnetic loops in § 5.3

5.1 Conclusion of the Self-similar Solutions

In chapter 2, we obtained self-similar solutions of relativistically expanding magnetic loops by extending the non-relativistic solutions obtained by Low (1982). We ignored the stellar rotation and assumed axisymmetry and the purely radial flow.

The self-similar parameter is given by $\eta = r/t$ and the radial velocity can be expressed as $v_r = \eta$. Since the time derivative of the velocity is zero, i.e., $Dv/Dt = 0$, our solutions describe the freely expanding magnetic loops in which we can choose a reference frame where all forces balance.

We found that a shell structure is formed inside the magnetic loops where the pressure and density pulses appear. The magnetic flux is swept up into the shell. The pressure pulse follows the density enhancement. This structure comes from the force balance in the radial direction. The gravity for the density enhancement balances with the pressure gradient force. Behind the pressure pulse, the density decreases. The buoyancy force driven by the density decrease balances with the pressure gradient. The pressure pulse structure is thus maintained by the gravity and the buoyancy forces. The amplitudes of the pressure and density enhancements inside the shell are larger for a thinner shell.

For the relativistic expansion, the effects of the displacement current cannot be ignored. Since the displacement current is larger for a faster expansion, this term dominates to $\nabla \times \boldsymbol{B}/(4\pi)$ for a faster expansion. We found that the displacement current is dominant when $\gamma \gtrsim 2.4$ for the dipolar solution, while it depends on the expansion speed and the shell structure for the shell and flux rope solutions. The displacement current reduces the magnetic tension force and changes the distribution of the plasma.

Inside the magnetic loops, a current sheet is formed. The magnetic reconnection may release the magnetic energy which is responsible for the giant flares (Lyutikov 2006).

The toroidal magnetic fields can be represented by the superposition of the Fourier modes in the polar angle θ. These modes should be determined by the position where magnetic twists are injected on the surface of the star when the crustal motion triggers the expansion. In general, we can construct more complex solutions that the poloidal magnetic field can be expressed as the superposition of the Fourier modes. Since the opening angle of the magnetic loops depends on the boundary at the surface of the star, the actual explosion can be represented as the superposition of the Fourier modes in both directions (i.e., the spherical harmonic function Y_l^m).

We derived the solutions of the freely expanding magnetic loops. How can we derive the solutions which describe the accelerating phase? We assumed that the magnetic flux $\tilde{A}$ depends on the radial distance and the time through the self-similar variable, i.e., $\tilde{A}(t, r, \theta) = \tilde{A}(\eta, \theta)$. Since the time derivative of the self-similar variable is zero, the magnetic flux is conserved, i.e., $D\tilde{A}/Dt = 0$. This means that the magnetic twist, and thus, the twist energy cannot be injected from the footpoints of the magnetic loops during this stage. To construct the solutions describing the accelerating stage, we need to relax this condition. It is left as the future work.

In our treatment, we do not consider the interaction between the expanding magnetic loops and the interstellar matter. When the magnetic loops expand, a fast shock is formed. We also need to include this effect in future work.

5.2 Conclusion of the Relativistic Outflow from the Relativistic Magnetic Reconnection

In chapter 3, we extended the Sweet-Parker magnetic reconnection to the relativistic plasma. We assumed that the plasma velocity, the plasma density, the plasma pressure, and the magnetic fields in the inflow and outflow regions are uniform and ignored the radiative effects. We adopted the energy, mass, and magnetic flux conservation equations between the inflow and the outflow. To close the system, we used the entropy conservation equation instead of using the momentum conservation equation. Although the momentum conservation equation degenerates to the energy conservation equation for the ultra-relativistic speed, the entropy conservation never degenerates to the other equations. By using the entropy conservation equation, we can readily include the effects that inertia decreases due to the expansion which were not included in previous works.

As the results, we found that the outflow velocity increases with $\sigma_{\rm i}$ for the sub relativistic case, i.e., ($\sigma_{\rm i} \lesssim 1$). For the strongly magnetized plasma $\sigma_{\rm i} >> 1$, since the thermal energy density exceeds the rest mass energy density, the outflow velocity saturates and the magnetic energy is not used for further acceleration but for the further heating. The saturated velocity depends on both the aspect ratio and the inflow velocity (reconnection rate) as $u_{\rm o} \sim (\beta_{\rm i} L/\delta)^{-1/2}$. This result indicates that the outflow speed becomes slower for a larger reconnection rate. Since the heating rate is proportional to the reconnection rate, the plasma inertia increases with the reconnection rate because enthalpy increases. The outflow velocity is then slower for a larger reconnection rate when $\sigma_{\rm i} \gtrsim 1$. The maximum inflow velocity can be estimated as $\beta_{\rm i,max} \sim \delta/L$. When $\beta_i \sim \beta_{\rm i,max}$, our solutions coincide with those by Lyubarsky (2005).

When the inflow velocity is much smaller than $\beta_{\rm i,max}$, the outflow speed can be ultra-relativistic ($\gamma_{\rm o} \sim \sigma_{\rm i}$). Although Lyutikov & Uzdensky (2003) also obtained ultra-relativistic outflow from relativistic magnetic reconnections, our solutions are completely different from theirs. They obtained the faster outflow and the larger reconnection rate because they ignored the thermal energy. However, the thermal energy cannot be ignored for the larger reconnection rate as mentioned above when $\sigma_{\rm i} \gtrsim 1$. The outflow can be ultra-relativistic only when the reconnection rate is extremely small for the relativistic magnetic reconnection.

In § 4, we studied the $\sigma_{\rm i}$ dependence of the reconnection outflow speed by 2-dimensional PIC simulations. We found that the outflow velocity is smaller than the Alfvén velocity of the inflow. We also found that the plasma pressure linearly increases with $\sigma_{\rm i}$ without saturation. These results are qualitatively consistent with those by the MHD analysis. The inflow velocity is about $0.2 - 0.7c \sim c\delta/L$. Thus the condition of the relativistic outflow $\beta_{\rm i} << \beta_{\rm i,max} \sim \delta/L$ is not satisfied. These results support the results of MHD analysis by Lyubarsky (2005) and by authors.

Since the magnetic reconnection can efficiently convert the magnetic energy into the plasma energy, it is expected that the relativistic magnetic reconnection can power the jets observed in active galactic nuclei and in galactic microquasars, (see, e.g., Meier et al. 2001) and the explosion in GRBs (see, e.g., Drenkhahn 2002). Our results, however, indicate that the outflow from the magnetic reconnection is only mildly relativistic. Most of the magnetic energy is used for heating the plasma. The thermal energy density of the outflow is larger than that of the rest mass. Is it possible to use the large amount of the thermal energy for further acceleration? The slower outflow from the magnetic reconnection is due to the increase of the enthalpy. When the outflow produced by the magnetic reconnection spreads into a fan, the plasma enthalpy decreases due to the expansion. Swisdak et al. (2008) and Zenitani & Hesse (2008b) performed 2-dimensional PIC simulations and showed that Weibel instability develops in the outflow region. Since the generated magnetic field deflects particle orbits, the enthalpy decreases because the outflow expands. We need to perform simulations in larger scales to confirm whether such an acceleration is possible.

Another possible mechanism to produce the relativistic outflow is the radiation effects. In our analysis, we do not include these effects. For a larger $\sigma_{\rm i}$, a synchrotron radiation is the main source to cool the plasma. The plasma energy is then extracted by the radiation, leading to the decrease in the enthalpy. Pair creations in the diffusion region can also enable the rapid outflow. Since the pair creation is endoergic, the plasma enthalpy decreases. We need to include these radiation processes carefully to study the plasma acceleration.

We have to point out that our discussion on the magnetic reconnection is restricted to the Sweet-Parker type magnetic reconnection. Petschek type magnetic reconnection, which includes slow shocks stemming from the diffusion region, can liberate more magnetic energy. Lyubarsky (2005) showed that the outflow speed is accelerated up to the Alfvén velocity of the inflow $\gamma_{\rm o} \sim \sqrt{\sigma_{\rm i}}$. Watanabe & Yokoyama (2006) performed 2-dimensional relativistic resistive MHD simulations and recovered the solution by Lyubarsky (2005). Shock structures did not appear in their PIC simulation, because the PIC simulation is concentrated on the small scale around the diffusion region. We need further study to judge whether the relativistic outflow is produced by the magnetic reconnection.

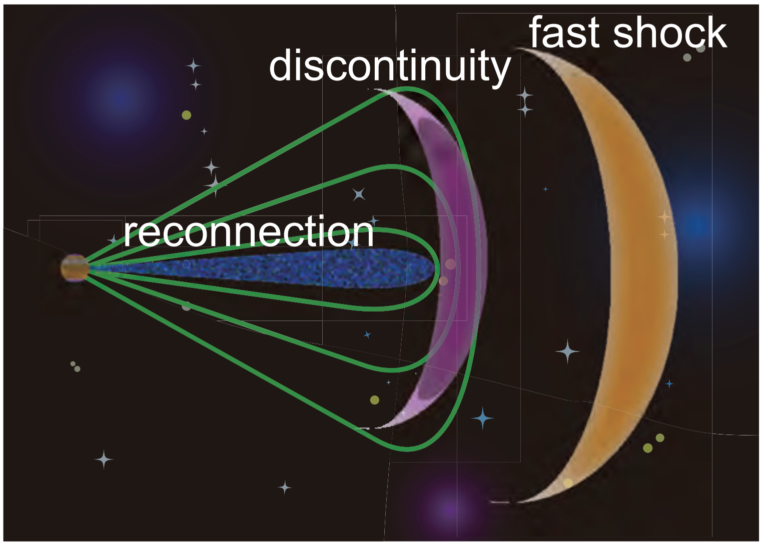

Figure 5.1: Schematic picture of the expanding magnetic loops. Fast shock is formed ahead of the loop top and current sheet is created inside the magnetic loops. Behind the loop top, tangential discontinuity is formed. These sites can be responsible for the particle acceleration.

5.3 Discussion of the Particle Acceleration in Expanding Magnetic Loops

Finally, we would like to discuss the acceleration mechanism associated with the expanding magnetic loops. Since spectrum of the SGR giant flares can be fitted with the power-law (Palmer et al. 2005), nonthermal particles are generated. The observed energy of the gamma-rays exceeds 10 MeV. The corresponding Lorentz factor of the electron is ~ 100 when we assumed that the electrons radiate through the synchrotron process and that mean magnetic field strength is $\sim 10^{12}$ G. When the magnetic loops emerging on the magnetar expand, a first shock is formed in front of the magnetic loops. Inside the magnetic loops, a current sheet is formed. The magnetic energy is released by the magnetic reconnection. First, particles are accelerated through the electric field by the magnetic reconnection. When slow shocks form, particles can be accelerated by the Fermi or other microscopic processes. At the loop top, a tangential discontinuity is formed where the direction of the magnetic field changes significantly. The toroidal magnetic field is dominant behind the discontinuity, while the poloidal magnetic field is dominant ahead of the discontinuity. The resulting electric field $\boldsymbol{E} = -\boldsymbol{v} \times \boldsymbol{B}/c$ also change its direction. Particles can be reflected by the electric field and gain energy. These accelerated particles can be further accelerated at the fast shock again. High energy particles can be generated through the multiple acceleration. If particles gain energy efficiently at each acceleration site, SGRs can be the source of the ultra-high energy cosmic rays, since the potential energy of the magnetar exceeds 10^{20} eV.

Appendix A

Relativistic Magnetohydrodynamics

In this appendix, the special relativistic MHD equations are derived and the properties of the relativistic MHD are reviewed. We take $c = 1$ for simplicity.

A.1 Derivation of the Relativistic MHD Equations

In the framework of the magnetohydrodynamics, electrons and ions have the same velocity, the density profile, and the temperature (1 fluid approximation). Since the electrons and ions move together, the electric fields in the comoving frame always vanish, i.e., $\boldsymbol{E}' = 0$ (dash denotes the comoving frame). By carrying out the Lorentz transformation, this condition in the observer frame moving with the velocity $\boldsymbol{v}$ is written as

$$\boldsymbol{E} + \boldsymbol{v} \times \boldsymbol{B} = 0. \tag{A.1.1}$$

We assume that distribution functions of electrons and ions in the comoving frame are maxwellian. We also assume that they obeys the same equation of states with the specific heat ratio of Γ. Then the energy momentum tensor of the plasma is described as

$$T_M^{\mu\nu} = \rho\xi u^\mu u^\nu - p g^{\mu\nu}, \tag{A.1.2}$$

where ρ, p, u^μ are the gas proper density, the gas proper pressure, and the bulk four velocity $u^\mu = (\gamma, \gamma v^i)$, respectively. Greek indices indicate four vectors ($\mu, \nu = 0, 1, 2, 3$), while Latin indices do the three vector ($i, j = 1, 2, 3$). $g^{\mu\nu} = \text{diag}\ (1, -1, -1, -1)$ is the metric tensor (assuming a flat spacetime and Cartesian space coordinates) and ξ is the relativistic specific enthalpy;

$$\xi = 1 + \frac{\Gamma}{\Gamma - 1}\frac{p}{\rho}. \tag{A.1.3}$$

The energy momentum tensor of the electromagnetic fields is written as

$$T^{\mu\nu}_{em} = \frac{1}{4\pi}\left(-F^{\mu\alpha}F^{\nu}_{\ \alpha} + \frac{1}{4}g^{\mu\nu}F^{\alpha\beta}F_{\alpha\beta}\right) = \left(\begin{array}{cc} U_{em} & S^i \\ S^i & \sigma^{ij} \end{array}\right). \tag{A.1.4}$$

where $F^{\mu\nu}$, U_{em}, S^i and σ^{ij} are the electromagnetc field tensor, the electromagnetc energy density, Poynting flux and the Maxwell stress tensor as

$$F^{\mu\nu} = \partial^{\mu}A^{\nu} - \partial^{\nu}A^{\mu}, \tag{A.1.5}$$

$$U_{em} = \frac{E^2 + B^2}{8\pi}, \tag{A.1.6}$$

$$S^i = \left(\frac{\boldsymbol{E}\times\boldsymbol{B}}{4\pi}\right)^i, \tag{A.1.7}$$

and

$$\sigma^{ij} = -\frac{1}{4\pi}\left[E^iE^j + B^iB^j - \frac{\delta^{ij}}{2}\left(\boldsymbol{E}^2 + \boldsymbol{B}^2\right)\right]. \tag{A.1.8}$$

Here A^{μ} and δ^{ij} are the vector potential in the comoving frame $A^{\mu} = (\phi, A^i)$ and the Kronecker delta, respectively. By taking the divergence of the total energy momentum tensor $T^{\mu\nu} = T^{\mu\nu}_M + T^{\mu\nu}_{em}$, we obtain four equations

$$\frac{\partial}{\partial t}\left[\rho\xi\gamma^2 - p + U_{em}\right] + \frac{\partial}{\partial x^j}\left[\rho\xi\gamma^2 v^j + S^j\right] = 0, \tag{A.1.9}$$

$$\frac{\partial}{\partial t}\left[\rho\xi\gamma^2 v^i + S^i\right] + \frac{\partial}{\partial x^j}\left[\rho\xi\gamma^2 v^i v^j + p\delta^{ij} + \sigma^{ij}\right] = 0. \tag{A.1.10}$$

The mass conservation equation can be written as

$$\frac{\partial(\rho\gamma)}{\partial t} + \frac{\partial(\rho\gamma v^i)}{\partial x^i} = 0. \tag{A.1.11}$$

The Maxwell equations are

$$\nabla\cdot\boldsymbol{B} = 0, \tag{A.1.12}$$

$$\nabla\cdot\boldsymbol{E} = 4\pi\rho_e, \tag{A.1.13}$$

$$\frac{\partial\boldsymbol{B}}{\partial t} = -\nabla\times\boldsymbol{E}, \tag{A.1.14}$$

and

$$\frac{\partial\boldsymbol{E}}{\partial t} = \nabla\times\boldsymbol{B} - 4\pi\boldsymbol{j}, \tag{A.1.15}$$

where ρ_e and $\boldsymbol{j}$ are the charge density and the charge current, respectively. Since equations (A.1.12) and (A.1.13) give conditions of constraint (divergence-free conditions), equations (A.1.1), (A.1.9), (A.1.10), (A.1.11), and (A.1.14) give the full set of the relativistic MHD equations. Equation (A.1.15) is not needed to close the system in ideal MHD. When we take into account the magnetic diffusivity, equation (A.1.1) is not satisfied and we need to solve equation (A.1.15). Another equation is needed to close the system, namely the Ohm's law which relates the electric field and the charge current $\boldsymbol{E} = \boldsymbol{E}(\boldsymbol{j})$ (see, e.g., Blackman & Field 1993).

From equations (A.1.14) and (A.1.15), we obtain

$$\frac{\partial U_{em}}{\partial t} + \frac{\partial S^j}{\partial x^j} = -E^j j^j, \tag{A.1.16}$$

and

$$\frac{\partial S^i}{\partial t} + \frac{\partial \sigma^{ij}}{\partial x^j} = -\rho_e E^i - (\boldsymbol{j} \times \boldsymbol{B})^i. \tag{A.1.17}$$

By substituting equations (A.1.16) and (A.1.17) into equation (A.1.9) and (A.1.10), we obtain

$$\begin{aligned} \frac{\partial}{\partial t}\left(\rho\xi\gamma^2 - p\right) + \frac{\partial}{\partial x^j}\left(\rho\xi\gamma^2\beta^j\right) &= j^j E^j, & \text{(A.1.18)} \\ \frac{\partial}{\partial t}\left(\rho\xi\gamma^2\beta^i\right) + \frac{\partial}{\partial x^j}\left(\rho\xi\gamma^2\beta^i\beta^j + p\delta^{ij}\right) &= \rho_e E^i + (\boldsymbol{j} \times \boldsymbol{B})^i, & \text{(A.1.19)} \end{aligned}$$

The right hand side of equation (A.1.18) denotes the Ohmic heating and that in equation (A.1.19) denote the electromagnetic force. By using equation (A.1.11), equation (A.1.19) can be written as

$$\rho\gamma\left[\frac{\partial}{\partial t} + (\boldsymbol{v}\cdot\nabla)\right](\xi\gamma\boldsymbol{v}) = \rho_e\boldsymbol{E} + \boldsymbol{j}\times\boldsymbol{B} - \nabla p. \tag{A.1.20}$$

This is the equation of motion in special relativistic MHD. Equation (A.1.20) reduces to that of the non-relativistic MHD by taking $\xi = 1$ and $(v/c)^2 = 0$. Note that the pressure term contributes to the inertia. The plasma inertia is larger for a larger thermal energy when the thermal energy density dominates to that of rest mass.

When the plasma inertia and the gas pressure can be ignored (force-free approximation), equation (A.1.20) is reduced to

$$\boldsymbol{E} + \boldsymbol{j}\times\boldsymbol{B} = 0. \tag{A.1.21}$$

The equations (A.1.14), (A.1.15) and (A.1.21) give us the force-free equations. Equation (A.1.21) corresponds to the Ohm's law for the relativistic force-free dynamics (Lyutikov 2003).

A.2 Derivation of the Gas Energy Equation

In the previous section, the full set of the relativistic MHD equations are derived. The derivation of the energy conservation is implicitly assumed that the entropy is conserved. The energy, momentum and entropy conservation equations are not independent. In this section, we derive the entropy conservation equation from the energy momentum conservation equations. We consider the purely hydrodynamics (without magnetic field) for simplicity. The procedure below is following to Mihalas & Mihalas (1984).

From the energy momentum conservation, i.e., $T^{\mu\nu}_{,\nu} = 0$, we obtain

$$u_\mu(\rho\xi u^\mu u^\nu)_{,\nu} - u^\mu p_{,\mu} = 0, \tag{A.2.1}$$

Because $u^\mu u_\mu = 1$, equation (A.2.1) can be written as

$$(\rho\xi u^\mu)_{,\mu} - u^\mu p_{,\mu} = 0. \tag{A.2.2}$$

By subtracting ξ times continuity equation (A.1.11), we obtain

$$\rho u^\mu \left(\epsilon_{,\mu} - \frac{p}{\rho^2}\rho_{,\mu}\right) = 0, \tag{A.2.3}$$

where ϵ is the specific internal energy. Using the expression of $u^\mu\partial_\mu \equiv D/D\tau$, where τ is the proper time, we obtain

$$\frac{D\epsilon}{D\tau} + p\frac{D}{D\tau}\left(\frac{1}{\rho}\right) = 0, \tag{A.2.4}$$

as the relativistic generalization of the gas energy equation for an deal gas (second law of the thermodynamics). Thus the entropy is conserved when the momentum and energies are conserved for the ideal fluids.

A.3 Waves in Relativistic Fluids

In relativistic MHD, there are 7 independent equations and thus there are 7 waves propagating in the magnetized fluids. These waves are named as fast waves, Alfvén waves, slow waves and entropy wave. When the magnetic field is always vanished, fast, slow and Alfvén waves disappear.

In this subsection, we derive the dispersion relation of the sound and Alfvén waves. The subscript 0 and 1 denote the zeroth (equilibrium part) and first order (perturbation part) of the variables, respectively. The quadratic of the perturbation part is assumed to be negligible.

A.3.1 Sound Wave

Consider non-magnetized fluids without bulk velocity ($v_0 = 0$). The energy momentum tensor is given by equation (A.1.2). Energy conservation equation can be written as

$$\frac{\partial e_1}{\partial t} + (e_0 + p_0)\nabla \cdot \boldsymbol{v}_1 = 0, \tag{A.3.1}$$

and momentum conservation equation can be written as

$$(e_0 + p_0)\frac{\partial \boldsymbol{v}_1}{\partial t} + \nabla p_1 = 0. \tag{A.3.2}$$

Here we ignore the quadratic terms of the perturbations. Combining these equations, we obtain

$$\frac{\partial^2 e_1}{\partial t^2} - \nabla^2 p = 0. \tag{A.3.3}$$

Thus the phase velocity (= the group velocity for the sound wave) of the sound wave c_s is given by

$$c_s = \sqrt{\frac{\partial p}{\partial e}}. \tag{A.3.4}$$

The equation of state for the ultra-relativistic gas is given by $p = e/3$ and sound speed is $c_s = 1/\sqrt{3}$.

A.3.2 Alfvén Wave

Let us consider the wave propagation in X-direction. We assume the uniform and static field in zeroth order and that the magnetic field assumed to be uniform in X-direction. We also assume $\boldsymbol{v}_0 = 0$ and $\boldsymbol{k} \cdot \boldsymbol{v}_1 = 0$, where $\boldsymbol{k}$ is the wave number.

From the Faraday's law (A.1.14) and (A.1.1), we obtain

$$\omega \boldsymbol{B}_1 + k B_0 \boldsymbol{v}_1 = 0. \tag{A.3.5}$$

From the equation of motion (A.1.20), we obtain

$$\rho_0 \xi_0 \omega \boldsymbol{v}_1 = k p_1 \frac{\boldsymbol{k}}{k} - \frac{k B_0}{4\pi}\boldsymbol{B}_1 - \frac{\omega B_0^2}{4\pi}\boldsymbol{v}_1. \tag{A.3.6}$$

By taking inner product with $\boldsymbol{k}$, we obtain $p = 0$. By substituting equations (A.3.5) and $p = 0$ into equation (A.3.6), we obtain the Alfvén velocity v_A as

$$v_A^2 \equiv \left(\frac{\omega}{k}\right)^2 = \frac{B_0^2/4\pi}{\rho_0 \xi_0 + B_0^2/4\pi}. \tag{A.3.7}$$

Note that the denominator of the right hand side of equation (A.3.7) includes not only the rest mass density, but also the thermal and magnetic energy densities which is interpreted as the enthalpy. In the non-relativistic limit, this term reduces to the rest mass energy density. While the sound speed is limited about 58% of the light speed, the Alfvén speed approaches the light speed for larger magnetic fields. When the plasma inertia and the gas pressure can be ignored (force-free approximation), the phase velocity of the Alfvén wave approaches the light speed. In force-free dynamics, only fast and sound waves can propagate with the light speed.

Appendix B

Self-similar Solutions

In this appendix, we explicitly show the self-similar solutions of the shell and flux rope solutions. The procedure of deriving solutions are mentioned in

B.1 Construction of the Shell Solutions

The functions Q and P in region I are given by

$$Q^I(\eta,\theta)=\sum_n \frac{Q_{0,n}}{1-\eta^2}\sin^n\theta, \tag{B.1.1}$$

$$P^I(\eta,\theta)=P_0(\eta)+P^I_A(\eta,\theta)+P^I_Q(\eta,\theta), \tag{B.1.2}$$

where P^I_A and P^I_Q are given by

$$P^I_A(\eta,\theta)=\frac{A_0^2a^4}{2\pi\eta^4}\sin^2\theta, \tag{B.1.3}$$

$$P^I_Q(\eta,\theta)=\begin{cases} -\displaystyle\sum_{m+n\neq 2}\frac{nQ_{0,m}Q_{0,n}}{4\pi(m+n-2)\eta^2(1-\eta^2)}\sin^{m+n-2}\theta, & \text{for}\quad m+n\neq 2,\\ -\displaystyle\sum_{m+n=2}\frac{nQ_{0,m}Q_{0,m}}{4\pi\eta^2(1-\eta^2)}\log(\sin\theta), & \text{for}\quad m+n=2. \end{cases} \tag{B.1.4}$$

The function D in region I is given by

$$D^I(\eta,\theta)=D_0(\eta)+D^I_A(\eta,\theta)+D^I_Q(\eta,\theta), \tag{B.1.5}$$

where D^I_A and D^I_Q are given by

$$D^I_A(\eta,\theta)=\frac{2A_0^2a^4}{\pi GM\eta^3(1-\eta^2)}\sin^2\theta, \tag{B.1.6}$$

$$D_Q^I(\eta,\theta) = \begin{cases} -\displaystyle\sum_{m+n\neq 2} \frac{nQ_{0,m}Q_{0,n}}{2\pi GM(m+n-2)\eta(1-\eta^2)^2}\sin^{m+n-2}\theta, & \text{for } \; m+n\neq 2, \\ -\displaystyle\sum_{m+n=2} \frac{nQ_{0,m}Q_{0,m}}{2\pi GM\eta(1-\eta^2)^2}\log(\sin\theta), & \text{for } \; m+n=2. \end{cases} \tag{B.1.7}$$

The functions Q and P in region II are given by

$$Q^{II}(\eta,\theta) = \sum_n \frac{Q_{0,n}}{1-\eta^2}\Lambda^{\frac{n}{2}}(\eta)\sin^n\theta, \tag{B.1.8}$$

$$P^{II}(\eta,\theta) = P_0(\eta) + P_A^{II}(\eta,\theta) + P_Q^{II}(\eta,\theta), \tag{B.1.9}$$

where P_A^{II} and P_Q^{II} are given by

$$P_A^{II}(\eta,\theta) = \frac{A_0^2a^4}{2\pi\eta^4}\Lambda(\eta)\left\{1-\frac{\sin^2 T(\eta)}{\sin^4 T(a)}\Psi(\eta)\right\}\sin^2\theta, \tag{B.1.10}$$

$$P_Q^{II}(\eta,\theta) = \begin{cases} -\displaystyle\sum_{m+n\neq 2} \frac{nQ_{0,m}Q_{0,n}\Lambda^{\frac{(m+n)}{2}}(\eta)}{4\pi(m+n-2)\eta^2(1-\eta^2)}\sin^{m+n-2}\theta, & \text{for } \; m+n\neq 2, \\ -\displaystyle\sum_{m+n=2} \frac{nQ_{0,m}Q_{0,n}\Lambda(\eta)}{4\pi\eta^2(1-\eta^2)}\log(\sin\theta), & \text{for } \; m+n=2. \end{cases} \tag{B.1.11}$$

Here $\Psi(\eta)$ is a function of η defined as

$$\Psi(\eta) = \left[\sin^2 T(\eta) + 4k\eta^3\sin T(\eta)\cos T(\eta) - 2k^2\eta^2(1-\eta^2)\left(3-4\sin^2 T(\eta)\right)\right]. \tag{B.1.12}$$

The function D^{II} is given by

$$D^{II}(\eta,\theta) = D_0(\eta) + D_A^{II}(\eta,\theta) + D_Q^{II}(\eta,\theta), \tag{B.1.13}$$

where D_A^{II} and D_Q^{II} are given by

$$D_A^{II}(\eta,\theta) = \frac{2A_0^2a^4}{\pi GM\eta^3(1-\eta^2)}\Lambda(\eta)\left[1-\frac{\sin^4 T(\eta)}{\sin^4 T(a)}\Xi(\eta)\right]\sin^2\theta, \tag{B.1.14}$$

$$D_Q^{II}(\eta,\theta) = \begin{cases} -\displaystyle\sum_{m+n\neq 2} \frac{nQ_{0,m}Q_{0,n}\Lambda^{\frac{m+n-2}{2}}(\eta)}{2\pi GM(m+n-2)\eta(1-\eta^2)^2} \\ \qquad \left\{1-\dfrac{\sin^4 T(\eta)}{\sin^4 T(a)}\left[1-2k\eta(1-\eta^2)\cot T(\eta)\right]\right\}\sin^{m+n-2}\theta, \\ \qquad\qquad \text{for } \; m+n\neq 2, \\ -\displaystyle\sum_{m+n=2} \frac{nQ_{0,m}Q_{0,n}}{2\pi GM\eta(1-\eta^2)^2} \\ \quad \left\{\log(\sin\theta)-\dfrac{\sin^4 T(\eta)}{\sin^4 T(a)}\left[\log(\sin\theta)+k\eta(1-\eta^2)\cot T(\eta)(1-2\log(\sin\theta))\right]\right\}, \\ \qquad\qquad \text{for } \; m+n=2. \end{cases} \tag{B.1.15}$$

Here $\Xi(\eta)$ is a function of η given by

$$\begin{aligned}\Xi(\eta) = 1 \quad & - \quad k\eta(1+\eta^2)(1-3\eta^2)\cot T(\eta) \\ & + \quad k^2\eta^2(1-\eta^2)(1+3\eta^2)\left[1-3\cot^2 T(\eta)\right] \\ & + \quad k^3\eta^3(1-\eta^2)^2\left[3\cot^3 T(\eta) - 5\cot T(\eta)\right]. \end{aligned} \tag{B.1.16}$$

$P_0(\eta)$ is an arbitrary function of η and is related to the function $D_0(\eta)$ through equation (2.2.12).

B.2 Construction of the Flux Rope Solutions

The function P in region I is given by

$$P^I(\eta,\theta) = P_0(\eta) + P_A^I(\eta,\theta) + P_Q^I(\eta,\theta), \tag{B.2.1}$$

where P_A^I and P_Q^I are

$$P_A^I(\eta,\theta) = \frac{A_0^2 a^4}{4\pi\eta^4}\frac{2-3\eta^2}{(1-\eta^2)^2}\sin^2\theta, \tag{B.2.2}$$

$$P_Q^I(\eta,\theta) = \begin{cases} -\displaystyle\sum_{m+n\neq 2}\frac{nQ_{0,m}Q_{0,n}}{4\pi(m+n-2)}\frac{\sin^{m+n-2}\theta}{\eta^2(1-\eta^2)^{1+(m+n)/4}}, & \text{for} \quad m+n\neq 2, \\ -\displaystyle\sum_{m+n=2}\frac{nQ_{0,m}Q_{0,n}}{4\pi}\frac{\log(\sin\theta)}{\eta^2(1-\eta^2)^{\frac{3}{2}}}, & \text{for} \quad m+n=2. \end{cases} \tag{B.2.3}$$

The function D in region I is given by

$$D^I(\eta,\theta) = D_0(\eta) + D_A^I(\eta,\theta) + D_Q^I(\eta,\theta), \tag{B.2.4}$$

where D_A^I and D_Q^I are

$$D_A^I(\eta,\theta) = \frac{A_0^2 a^4}{4\pi GM\eta^3}\frac{8-12\eta^2+3\eta^4}{(1-\eta^2)^3}\sin^2\theta, \tag{B.2.5}$$

$$D_Q^I(\eta,\theta) = \begin{cases} -\displaystyle\sum_{m+n\neq 2}\frac{nQ_{0,m}Q_{0,n}}{4\pi GM(m+n-2)}\frac{2-\eta^2}{\eta(1-\eta^2)^{2+(m+n)/4}}\sin^{m+n-2}\theta, & \text{for} \quad m+n\neq 2, \\ -\displaystyle\sum_{m+n=2}\frac{nQ_{0,m}Q_{0,n}}{8\pi GM}\frac{\eta^2+2(2-\eta^2)\log(\sin\theta)}{\eta(1-\eta^2)^{\frac{5}{2}}}, & \text{for} \quad m+n=2. \end{cases} \tag{B.2.6}$$

The function P in region II is described as

$$P^{II}(\eta,\theta) = P_0(\eta) + P_A^{II}(\eta,\theta) + P_Q^{II}(\eta,\theta), \tag{B.2.7}$$

where P_A^{II} and P_Q^{II} are

$$P_A^{II} = \frac{A_0^2 a^4}{4\pi\eta^4}\Lambda(\eta)\left[\frac{2-3\eta^2}{(1-\eta^2)^2}\Lambda(\eta) + 4k^2\eta^2\frac{\sin^2 T(\eta)(3-4\sin^2 T(\eta))}{\sin^4 T(a)}\right]\sin^2\theta, \tag{B.2.8}$$

$$P_Q^{II}(\eta,\theta) = \begin{cases} -\displaystyle\sum_{m+n\neq 2}\frac{nQ_{0,m}Q_{0,n}}{4\pi(m+n-2)}\frac{\Lambda^{\frac{m+n}{2}}(\eta)}{\eta^2(1-\eta^2)^{1+(m+n)/4}}\sin^{m+n-2}\theta, & \text{for } \ m+n\neq 2, \\ -\displaystyle\sum_{m+n=2}\frac{nQ_{0,m}Q_{0,n}}{4\pi}\frac{\Lambda(\eta)}{\eta^2(1-\eta^2)^{\frac{3}{2}}}\log(\sin\theta), & \text{for } \ m+n=2. \end{cases} \tag{B.2.9}$$

The function D is given by

$$D^{II}(\eta,\theta) = D_0(\eta) + D_A^{II}(\eta,\theta) + D_Q^{II}(\eta,\theta), \tag{B.2.10}$$

where D_A^{II} and D_Q^{II} are

$$D_A^{II}(\eta,\theta) = \frac{A_0^2 a^4}{4\pi GM\eta^3}\Lambda(\eta)\left[d_0(\eta)+d_1(\eta)+d_2(\eta)+d_3(\eta)\right]\sin^2\theta, \tag{B.2.11}$$

$$D_Q^{II}(\eta,\theta) = -\sum_{m,n}\frac{nQ_{0,m}Q_{0,m}}{4\pi GM\eta(1-\eta^2)^{2+\frac{m+n}{4}}}Y(\eta,\theta). \tag{B.2.12}$$

The functions d_0, d_1, d_2, d_3, and Y are given by

$$d_0(\eta) = \frac{3\eta^4-12\eta^2+8}{(1-\eta^2)^3}\Lambda(\eta), \tag{B.2.13}$$

$$d_1(\eta) = \frac{4k\eta(2-3\eta^2)}{(1-\eta^2)^2}\frac{\sin^3 T(\eta)\cos T(\eta)}{\sin^4 T(a)}, \tag{B.2.14}$$

$$d_2(\eta) = \frac{4k^2\eta^2(2+3\eta^2)}{1-\eta^2}\frac{\sin^2 T(\eta)(3-4\sin^2 T(\eta))}{\sin^4 T(a)}, \tag{B.2.15}$$

$$d_3(\eta) = -8k^3\eta^3\frac{\sin T(\eta)\cos T(\eta)(3-8\sin^2 T(\eta))}{\sin^4 T(a)}, \tag{B.2.16}$$

$$Y(\eta,\theta) = \begin{cases} \dfrac{\Lambda^{\frac{m+n-2}{2}}(\eta)}{m+n-2}\left[(2-\eta^2)\Lambda(\eta) + 4k\eta(1-\eta^2)\dfrac{\sin^3 T(\eta)\cos T(\eta)}{\sin^4 T(a)}\right]\sin^{m+n-2}\theta, \\ \qquad\qquad\qquad\qquad\qquad\qquad \text{for } \ m+n\neq 2, \\ \dfrac{1}{2}\left[\eta^2 + 2(2-\eta^2)\log(\sin\theta)\right]\Lambda(\eta) \\ \qquad\qquad +2k\eta(1-\eta^2)(-1+2\log(\sin\theta))\dfrac{\sin^3 T(\eta)\cos T(\eta)}{\sin^4 T(a)}, \\ \qquad\qquad\qquad\qquad\qquad\qquad \text{for } \ m+n=2. \end{cases} \tag{B.2.17}$$

The functions P_0 and D_0 are related each other through equation (2.2.12).

Appendix C

Wave Propagation with the Moving boundary in Vacuum

C.1 Electromagnetic Pulse Propagation

In chapter 2, the relativistic self-similar solutions in $r \leqq R(t)$ are derived. These solutions indicate that for the shell and flux rope solutions, the electromagnetic pulse is emitted from the loop top at $r = R(t)$ unless the condition (2.2.32) is satisfied. Electromagnetic pulse is also emitted in dipolar solutions. In this section, we study the propagation of the electromagnetic pulse in the vacuum ($r > R(t)$, region III) by imposing the boundary conditions at $r = R(t)$.

The Maxwell equations in vacuum are

$$\frac{\partial \boldsymbol{B}}{\partial t} + \nabla \times \boldsymbol{E} = 0, \tag{C.1.1}$$

$$\frac{\partial \boldsymbol{E}}{\partial t} = \nabla \times \boldsymbol{B}. \tag{C.1.2}$$

In the radiation gauge, the electromagnetic fields are represented in terms of the vector potential $\boldsymbol{A}$ as

$$\boldsymbol{E} = -\frac{\partial \boldsymbol{A}}{\partial t}, \tag{C.1.3}$$

$$\boldsymbol{B} = \nabla \times \boldsymbol{A}. \tag{C.1.4}$$

The Maxwell equations reduce to the following equation

$$\frac{\partial^2 \boldsymbol{A}}{\partial t^2} + \nabla \times (\nabla \times \boldsymbol{A}) = 0. \tag{C.1.5}$$

The boundary conditions at $r = R(t)$ are given as

$$\left[T_{\mathrm{M}}^{\prime ir} + T_{\mathrm{EM}}^{\prime ir} \right] = 0, \tag{C.1.6}$$

$$[\boldsymbol{E}'_{\perp}] = 0, \tag{C.1.7}$$

$$\left[B'_{\|}\right] = 0, \tag{C.1.8}$$

where T'^{ij}_{M} and T'^{ij}_{EM} denote the space-space components of energy momentum tensor for the matter and electromagnetic fields, respectively. The brackets [ ] denote the jump across the boundary $r = R(t)$. The subscript $\perp$ or $\|$ denotes the field component perpendicular/parallel to the velocity, and the prime denotes the variables defined in the rest frame.

Let us assume that

$$P_0(\eta = a) = D_0(\eta = a) = 0. \tag{C.1.9}$$

where $P_0(\eta)$ and $D_0(\eta)$ are arbitrary functions related by equation (2.2.12). By using these conditions, the jump condition (C.1.6) can be written as

$$[\sigma'^{rr}] = 0, \tag{C.1.10}$$

where σ^{ij} is the Maxwell stress tensor. Let us assume further that the toroidal magnetic field vanishes in the region where $r > R(t)$ (region III). The electromagnetic field in $r > R(t)$ can be expressed by a scalar function $\tilde{A}_{\mathrm{V}}$ as

$$\boldsymbol{A} = \frac{\tilde{A}_{\mathrm{V}}}{r\sin\theta}\boldsymbol{e}_{\phi}, \tag{C.1.11}$$

$$\boldsymbol{E} = \frac{1}{r\sin\theta}\left(0, 0, -\frac{\partial \tilde{A}_{\mathrm{V}}}{\partial t}\right), \tag{C.1.12}$$

$$\boldsymbol{B} = \frac{1}{r\sin\theta}\left(\frac{1}{r}\frac{\partial \tilde{A}_{\mathrm{V}}}{\partial \theta}, -\frac{\partial \tilde{A}_{\mathrm{V}}}{\partial r}, 0\right). \tag{C.1.13}$$

By carrying out the Lorentz transformation for the electromagnetic fields given by (2.1.8), (2.1.10), (C.1.12) and (C.1.13), the electromagnetic fields in the rest frame are given as

$$\boldsymbol{E}' = \begin{cases} \boldsymbol{0}, & (r \leqq R(t)), \\ -\dfrac{\gamma}{r\sin\theta}\left(\dfrac{\partial \tilde{A}_{\mathrm{V}}}{\partial t} + v\dfrac{\partial \tilde{A}_{\mathrm{V}}}{\partial r}\right)\boldsymbol{e}_{\phi}, & (r > R(t)), \end{cases} \tag{C.1.14}$$

$$\boldsymbol{B}' = \begin{cases} \dfrac{1}{r\sin\theta}\left[\dfrac{1}{r}\dfrac{\partial \tilde{A}}{\partial \theta}, -\dfrac{1}{\gamma}\dfrac{\partial \tilde{A}}{\partial r}, \dfrac{B}{\gamma}\right], & (r \leqq R(t)), \\ \dfrac{1}{r\sin\theta}\left[\dfrac{1}{r}\dfrac{\partial \tilde{A}_{\mathrm{V}}}{\partial \theta}, -\gamma\left(\dfrac{\partial \tilde{A}_{\mathrm{V}}}{\partial r} + v\dfrac{\partial \tilde{A}_{\mathrm{V}}}{\partial t}\right), 0\right], & (r > R(t)). \end{cases} \tag{C.1.15}$$

By substituting equations (C.1.14) and (C.1.15) into (C.1.7), (C.1.8), and (C.1.10), the boundary conditions for the scalar function $\tilde{A}_{\mathrm{V}}$ can be obtained as

$$\left.\frac{\partial \tilde{A}_{\mathrm{V}}}{\partial t} + v\frac{\partial \tilde{A}_{\mathrm{V}}}{\partial r}\right|_{r=R(t)} = 0, \tag{C.1.16}$$

$$\left.\frac{\partial \tilde{A}_{\mathrm{V}}}{\partial \theta}\right|_{r=R(t)} = 0, \tag{C.1.17}$$

$$\left.\frac{\partial \tilde{A}_{V}}{\partial r}\right|_{r=R(t)} = \begin{cases} -\dfrac{2A_0 a}{t\sqrt{1-a^2}}\sin^2\theta, & \text{(dipolar solution)}, \\ -\dfrac{4A_0 a^2 k \cot T(a)}{t}\sin^2\theta, & \text{(shell solution)}, \\ -\dfrac{4A_0 a^2 k \cot T(a)}{t\sqrt{1-a^2}}\sin^2\theta, & \text{(flux rope solution)}, \end{cases} \tag{C.1.18}$$

By substituting equation (C.1.11) into the Maxwell equations (C.1.5), we obtain

$$\frac{\partial^2 \tilde{A}_{\mathcal{V}}}{\partial t^2} - \hat{\mathcal{L}}_{(r,\theta)}\tilde{A}_{\mathrm{V}} = 0. \tag{C.1.19}$$

The equation (C.1.19) with the boundary conditions (C.1.16), (C.1.17) and (C.1.18) are identical to those of the non-relativistic case (Low 1982).

Let us expand the flux function $\tilde{A}_{\mathrm{V}}$ in a series of t as

$$\tilde{A}_{\mathrm{V}} = \sum_{\mu} t^{\mu} G(\mu;\eta)\sin^2\theta, \tag{C.1.20}$$

where G is a function of η. Substituting equation (C.1.20) into equation (C.1.19), we obtain

$$(1-\eta^2)\frac{d^2 G}{d\eta^2} + 2(\mu-1)\eta\frac{dG}{d\eta} - \left[\mu(\mu-1) + \frac{2}{\eta^2}\right]G = 0. \tag{C.1.21}$$

Here we abbreviate the summation of the series of t. Next, we change variables as

$$x = \eta^2, \tag{C.1.22}$$

$$\sigma(\mu;\eta) = \eta G. \tag{C.1.23}$$

Substituting equations (C.1.22) and (C.1.23) into equation (C.1.21), we obtain

$$x(1-x)\frac{d^2\sigma}{dx^2} + \left[-\frac{1}{2} - \frac{x}{2}(1-2\mu)\right]\frac{d\sigma}{dx} - \frac{\mu(\mu+1)}{4}\sigma = 0. \tag{C.1.24}$$

This differential equation can be recognized to be that for the Gauss Hypergeometric function $F(\alpha,\beta,\gamma;x)$.

Then $\tilde{A}_{\rm V}$ can be written as

$$\tilde{A}_{\rm V} = \sum_{\mu} \frac{t^{\mu}}{\eta} s_0(\mu) F\left(-\frac{\mu}{2}, -\frac{\mu+1}{2}, -\frac{1}{2}; \eta^2\right) + s_1(\mu)\eta^3 F\left(\frac{3-\mu}{2}, \frac{2-\mu}{2}, \frac{5}{2}; \eta^2\right), \quad \text{(C.1.25)}$$

where s_0 and s_1 are constants of integral. Substituting equation (C.1.20) into equation (C.1.18), we obtain $\mu = 0$. Then equation (C.1.25) is reduced to

$$\tilde{A}_{\rm V} = \left\{ \frac{s_0}{\eta} + \frac{s_1}{\eta}\left[\eta - \frac{1}{2}\ln\frac{1+\eta}{1-\eta}\right]\right\} \sin^2\theta. \quad \text{(C.1.26)}$$

By imposing boundary conditions (C.1.16), (C.1.17) and (C.1.18), we obtain

$$s_0 = -2A_0\sqrt{1-a^2}\left[a - \frac{1}{2}\ln\frac{1+a}{1-a}\right], \quad \text{(C.1.27)}$$

$$s_1 = 2A_0\sqrt{1-a^2}, \quad \text{(C.1.28)}$$

and thus we obtain

$$\tilde{A}_{\rm V} = 2A_0\sqrt{1-a^2}\left[1 - \frac{a}{\eta} + \frac{1}{2\eta}\ln\frac{1-\eta}{1+\eta}\frac{1+a}{1-a}\right]. \quad \text{(C.1.29)}$$

for dipolar solution.

Electromagnetic fields in $r > R(t)$ for the shell and flux rope solutions can be obtained by replacing A_0 with $2A_0ak\sqrt{1-a^2}\cot T(a)$ and $2A_0ak\cot T(a)$, respectively.

Fig. C.1 shows the profile of the function $J(\eta)$ (left) and the contours of the magnetic flux (right) for the dipolar solution with $a = 0.7$. The infinity in the electromagnetic field at $r = t$ is originated from the assumption of the self-similarity. Since we assumed a point source at $r = 0$, the magnetic field strength becomes infinite as $t \to 0$. In turn, the electric current diverges as $t \to 0$. This infinite current generates an electromagnetic pulse at the electromagnetic wave front at $r = t$. To avoid the infinite magnetic field, we should replace the boundary conditions at $r = R(t)$ given by (C.1.16), (C.1.17) and (C.1.18) with those at $t = t_0$, and its radius $r = r_0$ when the self-similar stage starts. It is out of the scope of this thesis to study the non self-similar stage before $t = t_0$.

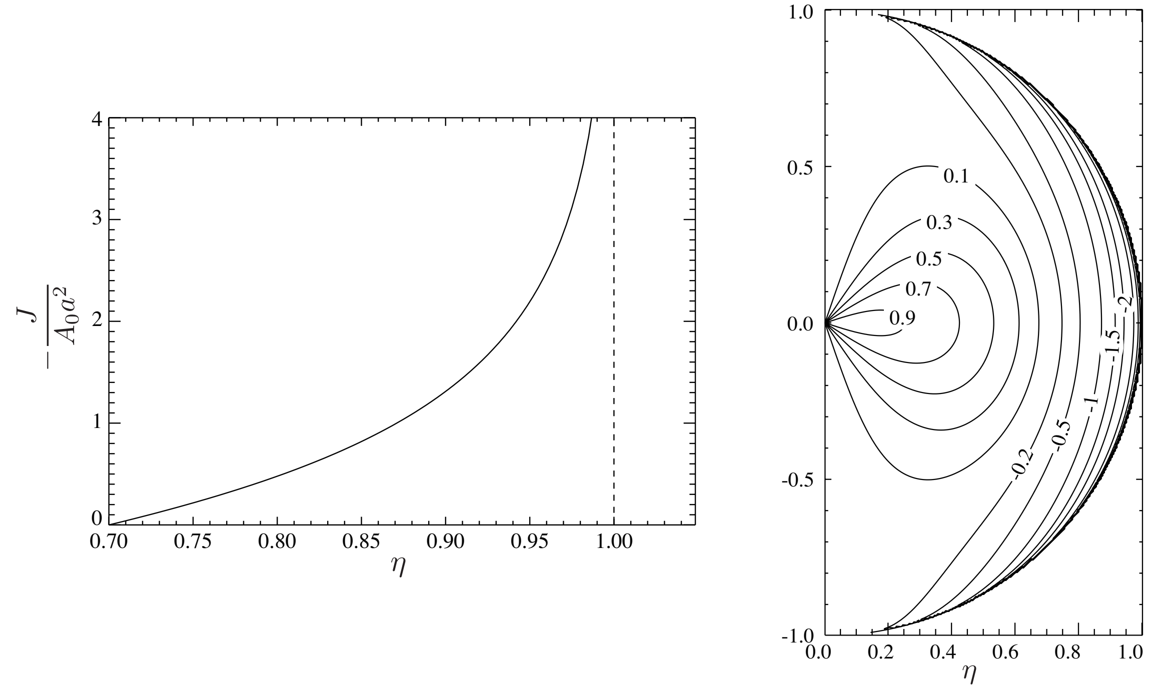

Figure C.1: Left: the profile of the function $J(\eta)$ for the dipolar solution in the region $\eta > a$ with $a = 0.7$. The dashed line shows the boundary at $r = t$. Right: contour plots of the magnetic flux in $\eta - \theta$ plane for the dipolar solution with $a = 0.7$.

Appendix D

Some Algebra Calculations Used in the Self-similar Solution

D.1 Derivation of a_*

In this appendix, we derive a_* given in equation (2.3.22) which is the critical value for $P_A > 0$. We change the variables a and η into α and x as

$$\alpha = a^2, \tag{D.1.1}$$

and

$$x = \eta^2, \tag{D.1.2}$$

where α and ξ are defined in

$$0 \leq x \leq \alpha \leq 1. \tag{D.1.3}$$

By using these variables, equation (2.3.21) can be rewritten as

$$g(x) = 2x^3 - x^2 - 3\alpha x + 2\alpha. \tag{D.1.4}$$

The critical vale a_* is obtained by solving $g(x) = 0$ in region (D.1.3). The solution of $dg/dx = 0$ is given by

$$x = x_\pm \equiv \frac{1 \pm \sqrt{1 + 18\alpha}}{6}, \tag{D.1.5}$$

where the subscript ± coincides with the sign of the term of the square root. The function $g(x)$ has two extrema, x_- is the negative value, while x_+ is positive value. Since $g(0) = 2\alpha \geq 0$, $g(x)$ has a negative value when $g(x_+) \leq 0$ and $x_+ \leq \alpha$ in the domain $0 \leq x \leq \alpha \leq 1$ (see Fig. D.1).

From the condition that $x_+ < \alpha$, we obtain

$$\alpha > \frac{5}{6}. \tag{D.1.6}$$

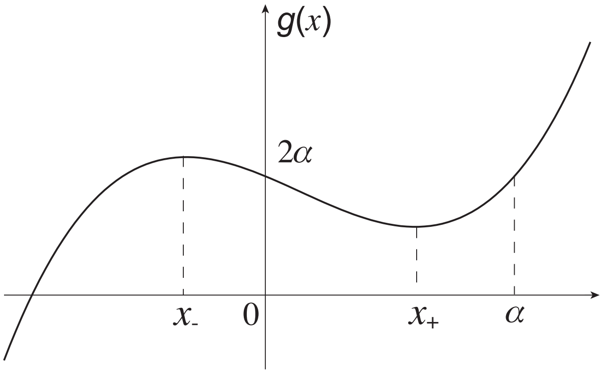

Figure D.1: Profile of the function $g(x)$. $g(x)$ can be negative at $x = x_+$. The function $g(x)$ has a negative value when $x_+ < \alpha$ and $g(x_+) \leq 0$.

and from the equation that $g(x_+) = 0$, we obtain

$$\alpha_\pm = \frac{69 \pm 11\sqrt{33}}{144}. \tag{D.1.7}$$

From these equations, the function g_+ is always positive when $\alpha < \alpha_+$. Thus the critical value a_* is obtained as

$$a_* = \frac{\sqrt{69 + 11\sqrt{33}}}{12}. \tag{D.1.8}$$

D.2 Proof of $j_{\rm rot} > 0$

According to equation (2.3.24), we define the following function

$$f(x) = 2\alpha - 5\alpha x + 5x^2 - 2x^3, \tag{D.2.1}$$

where the definition of α and x are given in equations (D.1.1) and (D.1.2), respectively. This function has the extremum at

$$x_\pm = \frac{5 \pm \sqrt{25 - 30\alpha}}{6}. \tag{D.2.2}$$

When $\alpha \geq 5/6$, the function f does not have a extremum. Since the function f is the cubic function and the sign of x^3 is minus, f decreases monotonically. The both end of the function f are

$$f(x = 0) = 2\alpha \geq 0, \tag{D.2.3}$$

and

$$f(x = \alpha) = 2\alpha(1 - \alpha^2) \geq 0. \tag{D.2.4}$$

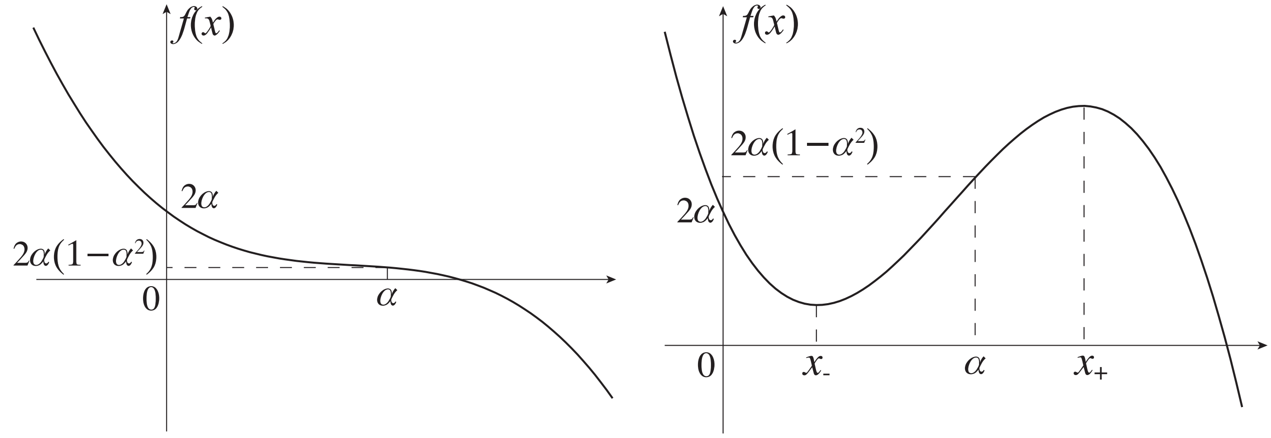

Figure D.2: Left: Profile of the function f for $\alpha > 5/6$. Since both bound is positive and the function f decreases monotonically, f is positive. Right: Profile of the function f for $\alpha < 5/6$.

Thus the function f is always positive for $\alpha > 5/6$ (see Fig. D.2).

When $\alpha < 5/6$, x_+ is larger than α as

$$x_+ = \frac{5 + \sqrt{25 - 30\alpha}}{6} \geq \frac{5}{6} > \alpha. \tag{D.2.5}$$

and x_- is smaller than α as

$$\alpha - x_- = \frac{1}{6}\left[-(5 - 6\alpha) + \sqrt{5(5 - 6\alpha)}\right] \geq 0. \tag{D.2.6}$$

Since $f(0), f(\alpha) > 0$ and f is the cubic function, $f(x)$ is always positive when $f(x_-) > 0$ (see, Fig. D.2).

The function $F(\alpha) \equiv f(x_+)$ and its derivatives are given by

$$F(\alpha) = \frac{1}{54}\left[125 - 117\alpha - 5\sqrt{5}(5 - 6\alpha)^{\frac{3}{2}}\right], \tag{D.2.7}$$

$$\frac{dF(\alpha)}{d\alpha} = -\frac{13}{6} + \frac{5}{6}\frac{6 - 5\alpha}{\sqrt{1 - 6\alpha/5}}, \tag{D.2.8}$$

$$\frac{d^2F(\alpha)}{d\alpha^2} = -\frac{5}{2}\frac{1}{\sqrt{1 - 6\alpha/5}}. \tag{D.2.9}$$

The function $F(\alpha)$ has a local maximum at $a = 76/125 < 5/6$ and its derivative decreases monotonically. Since $F(\alpha = 0) = 0$ and $F(\alpha = 5/6) = 55/108$, the function $F(\alpha)$ is positive in the range $0 \leq \alpha \leq 5/6$. Thus the function $f(x)$ is positive when $0 \leq x \leq \alpha \leq 1$.

Appendix E

The Virial Theorem of the Self-similar Relativistic MHD

The virial theorem in non-relativistic MHD was derived by Chandrasekhar & Fermi (1953). Low (1982) applied it to the expanding magnetic loops by evaluating the surface term. Landau & Lifshitz (1975) derived the theorem for a relativistic case in elegant way by integrating the energy momentum tensor. In this appendix, we derive the virial theorem for a relativistic self-similar MHD.

We start from the equations of motion in self-similar stage given by (2.1.36). Taking the inner product with $\boldsymbol{r}$ and integrating it within a volume V, we obtain

$$\int dV \left[\frac{\Gamma}{\Gamma-1}\frac{p\gamma^2 v^2(\boldsymbol{r}\cdot\boldsymbol{e}_r)}{r} - \boldsymbol{r}\cdot\nabla p + \boldsymbol{r}\cdot(\rho_e\boldsymbol{E}+\boldsymbol{j}\times\boldsymbol{B}) - \frac{GM\gamma\rho}{r^2}(\boldsymbol{r}\cdot\boldsymbol{e}_r)\right] = 0. \quad \text{(E.0.1)}$$

The first term is the thermal inertial term $U_{\rm in}$ and the forth term is the gravitational potential energy W. Integrating the second term by parts, we obtain

$$\int dV \boldsymbol{r}\cdot\nabla p = -3(\Gamma-1)U_{\rm th} + \int p\boldsymbol{r}\cdot d\boldsymbol{\mathcal{A}} \quad \text{(E.0.2)}$$

where $\boldsymbol{\mathcal{A}}$ is a closed surface of the volume V. The third term can be rewritten by using the Maxwell equations as follows,

$$\int_V dV\left[\boldsymbol{r}\cdot(\rho_e\boldsymbol{E}+\boldsymbol{j}\times\boldsymbol{B})\right] = -\int dV\frac{\partial}{\partial t}(\boldsymbol{r}\cdot\boldsymbol{S}) - \int dV\boldsymbol{r}\cdot(\nabla\cdot\boldsymbol{\sigma}), \quad \text{(E.0.3)}$$

where $\boldsymbol{S}$ and $\boldsymbol{\sigma}$ are the Poynting flux and the Maxwell's stress tensor, respectively. Note that the time derivative cannot be exchanged with the integration with volume in the first term since the volume V changes with time.

The second term on the right hand side of equation (E.0.3) has a form

$$-\int dV\boldsymbol{r}\cdot(\nabla\cdot\boldsymbol{\sigma}) = U_{\rm E}+U_{\rm M}+\frac{1}{8\pi}\int\left\{2\left[(\boldsymbol{r}\cdot\boldsymbol{E})(\boldsymbol{E}\cdot d\boldsymbol{\mathcal{A}})+(\boldsymbol{r}\cdot\boldsymbol{B})(\boldsymbol{B}\cdot d\boldsymbol{\mathcal{A}})\right]-(\boldsymbol{E}^2+\boldsymbol{B}^2)(\boldsymbol{r}\cdot d\boldsymbol{\mathcal{A}})\right\}, \quad \text{(E.0.4)}$$

where U_{E} and U_{M} are the electric and magnetic energies given by equations (2.3.5) and (2.3.6), respectively. By using these results, we obtain the virial theorem for the relativistic self-similar MHD;

$$3(\Gamma-1)U_{\mathrm{th}}+U_{\mathrm{in}}+U_{\mathrm{M}}+U_{\mathrm{E}}+W=\mathcal{H}+\mathcal{S}, \tag{E.0.5}$$

where

$$\mathcal{H}=\int p\boldsymbol{r}\cdot d\boldsymbol{\mathcal{A}}-\frac{1}{8\pi}\int\left\{2\left[(\boldsymbol{r}\cdot\boldsymbol{E})(\boldsymbol{E}\cdot d\boldsymbol{\mathcal{A}})+(\boldsymbol{r}\cdot\boldsymbol{B})(\boldsymbol{B}\cdot d\boldsymbol{\mathcal{A}})\right]-(\boldsymbol{E}^2+\boldsymbol{B}^2)(\boldsymbol{r}\cdot d\boldsymbol{\mathcal{A}})\right\}, \tag{E.0.6}$$

and

$$\mathcal{S}=\int dV\frac{\partial}{\partial t}\left(\boldsymbol{r}\cdot\frac{\boldsymbol{E}\times\boldsymbol{B}}{4\pi}\right). \tag{E.0.7}$$

Here, K is the kinetic energy given by equation (2.3.2).

Readers may wonder why the thermal inertial term appears. Actually, the kinetic, thermal, and thermal inertial energies should not be considered separately because they depend on the frame of reference. Even so, we used this definition in chapter 2.2 to make clear the difference between the non-relativistic and relativistic expansions. We can easily figure out that the total plasma energy can be described as the sum of these energies, as

$$K+U_{\mathrm{th}}+U_{\mathrm{in}}=\int dV\left[\left(\rho+\frac{\Gamma}{\Gamma-1}p\right)\gamma^2-p\right]. \tag{E.0.8}$$

Appendix F

Magnetic Reconnection in a Forming Current Sheet

In Chapter 4, we showed the results of 2-dimensional PIC simulations of the relativistic magnetic reconnection assuming a preexisting current sheet at the initial state. The magnetic reconnection is driven by the external electric fields. In this chapter, we study how the magnetic reconnection takes place in a forming current sheet. For this purpose, we performed 2-dimensional PIC simulations without postulating the initial current sheet.

F.1 Initial Model

Simulation region is a 2-dimensional box in the $X-Y$ plane. We assumed a collisionless pair plasma.

We adopted the model studied by Mikic et al. (1988) as the initial condition. The initial magnetic fields are given by

$$\begin{aligned} B_x &= -B_0 \cos(y - L_y/2) \exp(-k_y x), \\ B_y &= B_0 \sin(y - L_y/2) \exp(-k_y x), \\ B_z &= 0, \end{aligned} \tag{F.1.1}$$

where L_y is the box size in Y direction and $k_y = 2\pi/L_y$. A schematic picture of the initial condition is shown in Fig. F.1.

Since the magnetic field given by equation (F.1.1) is the potential field, plasma distributes homogeneously in coordinate space and isotropic in momentum space. The initial plasma temperature is $T = 0.01mc^2$. The ratio of the gyro frequency to the plasma frequency is unity. The grid size Δ and the time step is normalized by the gyro radius r_g

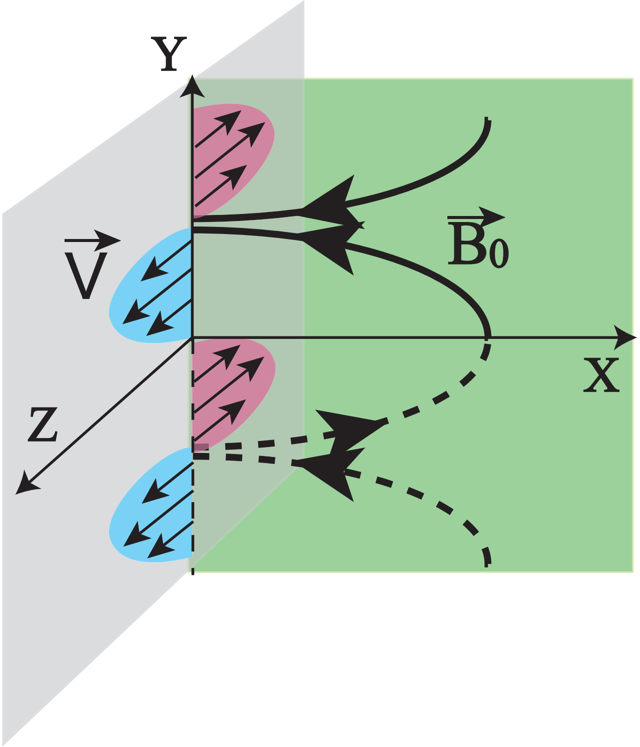

Figure F.1: Schematic picture of the initial condition for the expanding magnetic loops. Simulations are performed in the $X-Y$ plane. The initial magnetic fields are in the $X-Y$ plane, while the shear flow at $X=0$ is in Z direction.

and the gyro frequency Ω_g, respectively. We set $\Delta = 0.2r_g$. The number of mesh points is $(N_x, N_y) = (4096, 256)$ and the corresponding simulation box size is $-25.6 \leq X/r_g \leq 25.6$ and $0 \leqq Y/r_g \leqq 819.2$. The number density at the initial state is 50 pairs per cell.

We imposed a shear flow at the footpoints of the magnetic loops ($X = 0$). The profile of the shear velocity is given by

$$V_z = V_0 \sin(2k_y y). \tag{F.1.2}$$

The maximum shear velocity is $0.3c$. The electric fields at the footpoints of the magnetic loops are calculated by $\boldsymbol{E} = -\boldsymbol{V} \times \boldsymbol{B}/c$. The induced electric field is calculated at each time step. The boundary condition is periodic in Y direction and absorbing boundary in $X = X_{\max} = 819.2r_g$. We use more grids in X direction to avoid the wave reflection at $X = X_{\max}$.

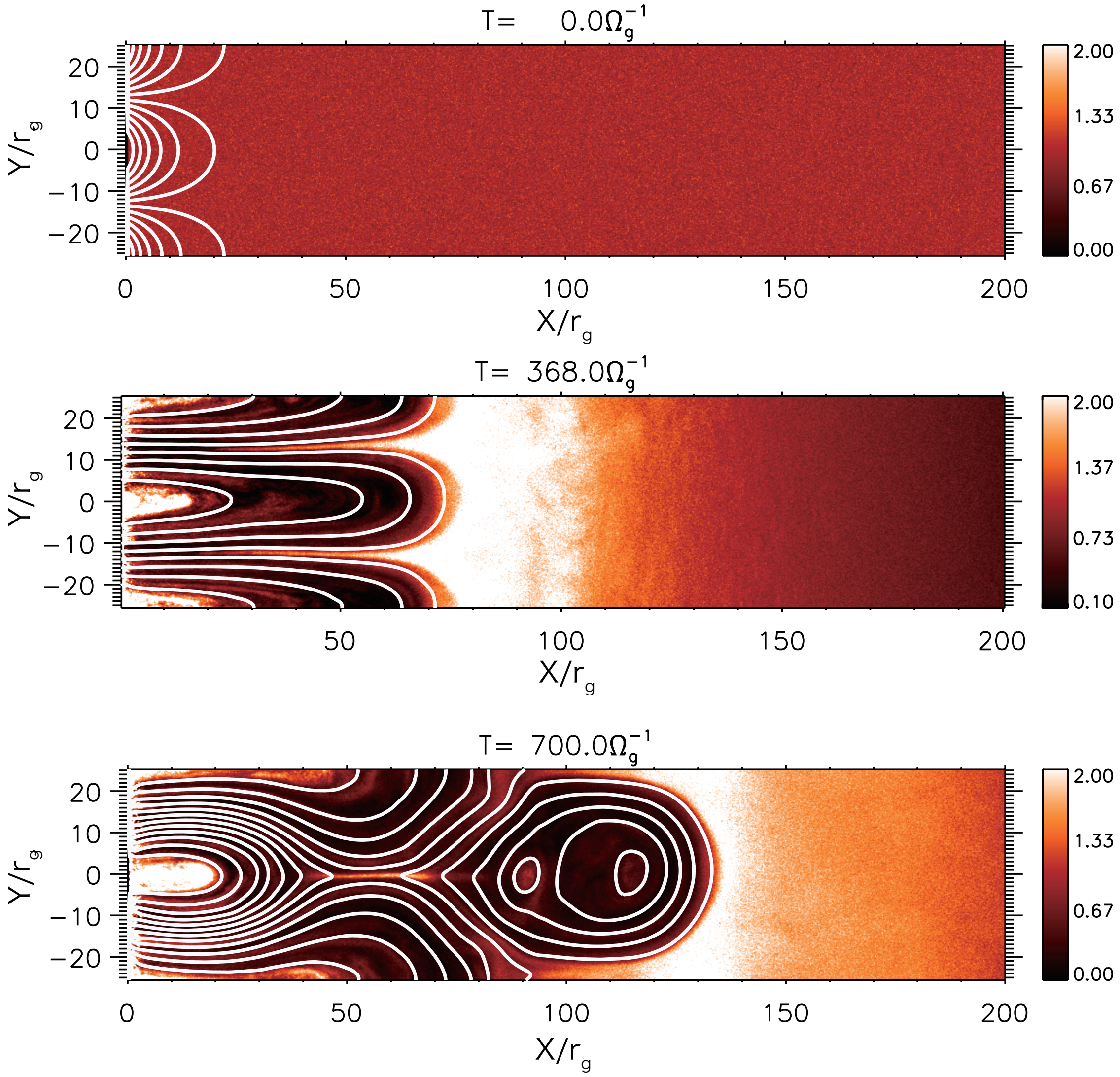

Figure F.2: Color contours show the plasma density and the curves show the magnetic field lines at $t = 0$, 368, $700\Omega_c^{-1}$ from top to bottom, respectively. The plasma density is normalized by that of the initial value.

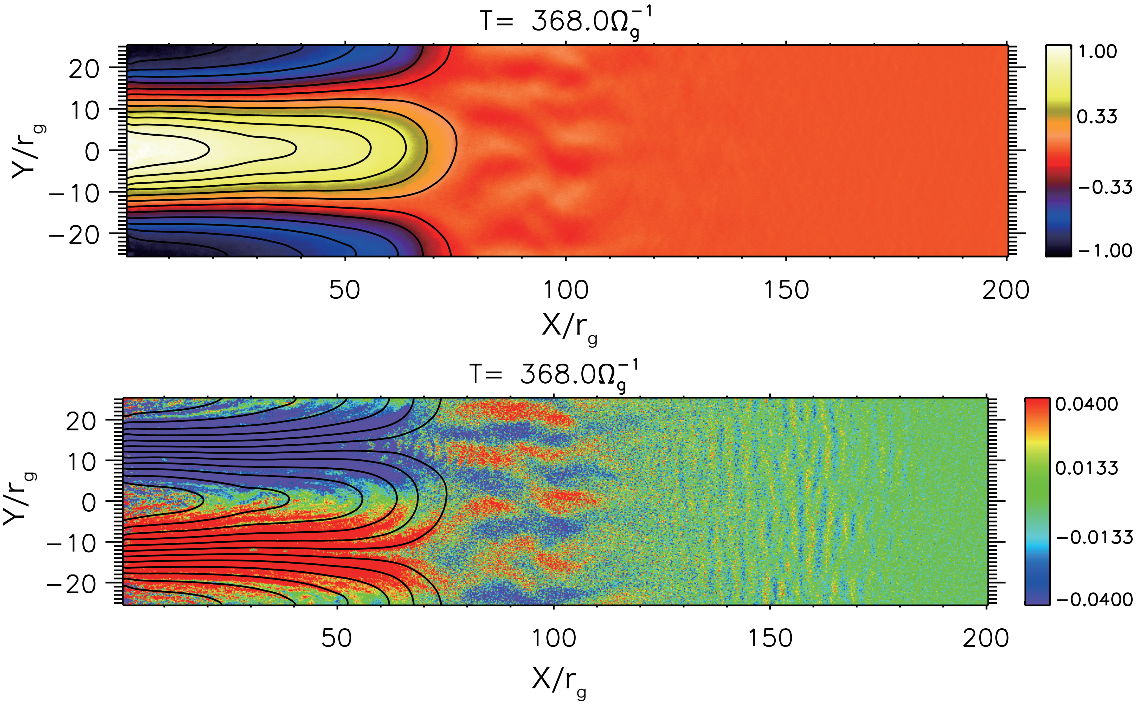

Figure F.3: Snapshots at $t = 368\Omega_g^{-1}$. Color contours show the toroidal magnetic fields (top panel), and the current density j_x, while the curves show the magnetic field lines in both panels.

F.2 Results

Fig. F.2 shows the evolution of the magnetic loops. Color contours show the plasma density, while the curves show the magnetic field lines at $t = 0$, 368, $700\Omega_c^{-1}$ from top to bottom, respectively. After the shear injection, current circuits along the magnetic field lines are created by the induced electric field. The electric currents along the magnetic field lines create the Z component of (toroidal) magnetic fields obeying the Faraday's law. The direction of the toroidal magnetic fields coincides with that of the shear flow. These mechanism can be explained as that the magnetic field lines are frozen in to the plasma. The toroidal magnetic fields exert the Lorentz force on the current along the magnetic field lines. This force leads to the expansion of the magnetic loops (the expansion by the magnetic pressure). The expansion speed $\sim 0.2c$ is comparable to the shear velocity at the footpoints.

Fig. F.3 shows the snapshot at $t = 368\Omega_g^{-1}$. Color contours show the toroidal (Z component of the) magnetic fields (top panel) and the charge current j_x (bottom). Curves show the magnetic field lines. Fig. F.4 shows the profile of the magnetic pressure at

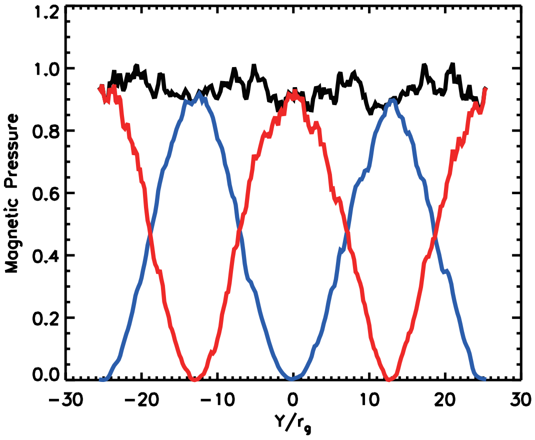

Figure F.4: Magnetic pressure by the poloidal (blue curve) and toroidal (red curve) components at $X = 20r_g$. Horizontal axis shows Y/r_g. The total magnetic pressure is plotted in black curve.

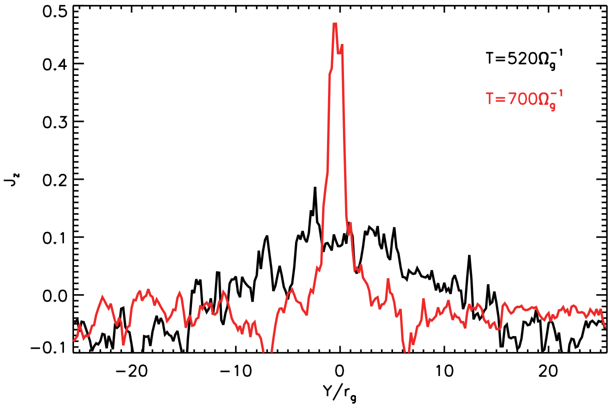

Figure F.5: Time evolution of the current density at $X = 20r_g$. Horizontal axis shows Y/r_g. Black curve is at $t = 520\Omega_g^{-1}$, while the red one is at $t = 700\Omega_g^{-1}$

$X = 20r_g$. Inside the magnetic loops, the magnetic pressure by the toroidal component is dominant to that of the poloidal (X and Y) component. The magnetic pressure by the toroidal magnetic field is sandwiched by that by poloidal magnetic fields. This structure satisfies the pressure balance in Y direction.

Note that the charge current j_x is created ahead of the loop top (see the bottom panel of Fig. F.3). Subsequently, magnetic fields B_z weaker than that inside the magnetic loops also appear. This magnetic field is generated by the Weibel instability (Weibel 1959). Behind the loop top, since the magnetic field lines are swept up due to the expansion, the magnetic field strength becomes strong. The ambient plasma (distributed forward the magnetic loops) is reflected at the loop top by the induced electric fields, $\boldsymbol{E} = -\boldsymbol{v} \times \boldsymbol{B}/c$. An anisotropy of the distribution function in the momentum space then arises between the ambient and reflected plasmas. The interaction between these plasmas can generate the magnetic fields in parallel to increasing the entropy.

Due to the expansion of the magnetic loops, the magnetic field lines become antiparallel. A resulting current sheet is created inside the magnetic loops. Fig. F.5 shows the evolution of the electric current (j_z) at $X = 20r_g$. Horizontal axis shows Y/r_g. The black curve is at $t = 520\Omega_g^{-1}$, while the red one is at $t = 700\Omega_g^{-1}$. The current sheet is elongated in X direction due to the expansion as well as thinning in Y direction and increasing in the current density. When the thickness of the current sheet is of order the gyro radius, the magnetic reconnection takes place.

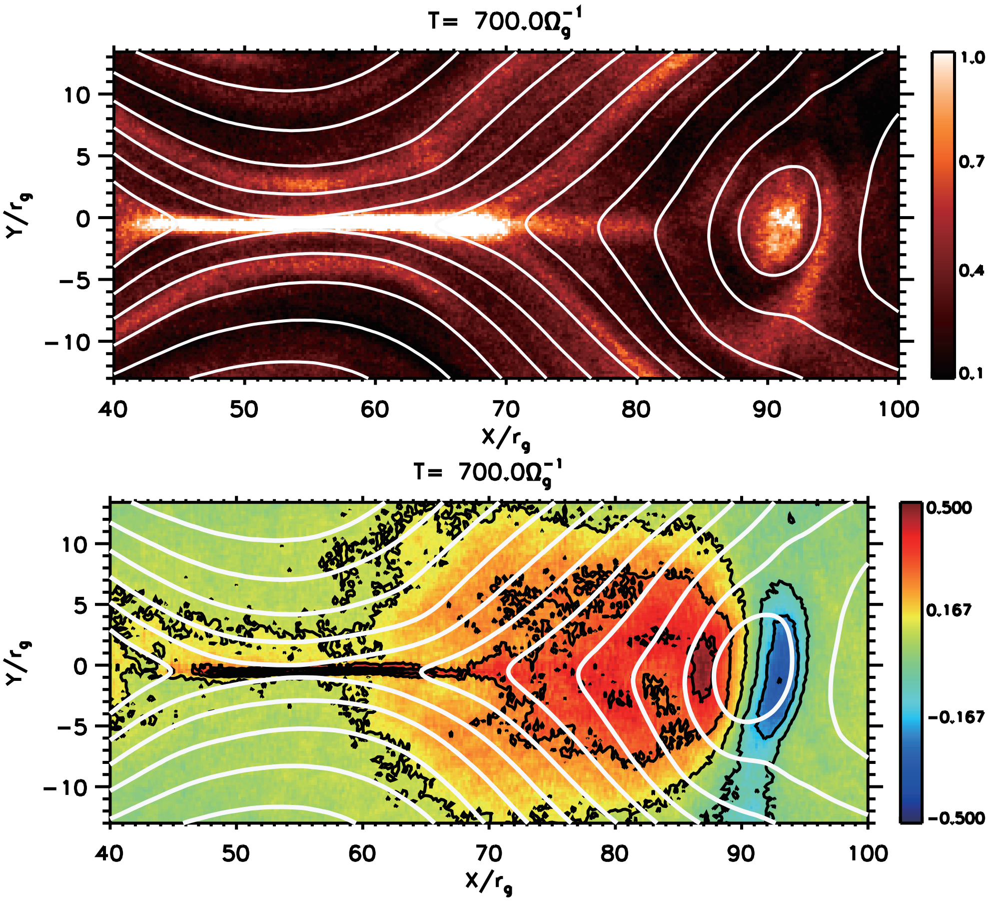

Figure F.6: Snapshot at $t = 700\Omega_g^{-1}$ when the magnetic reconnection takes place. Color contours show the plasma density (top panel) and E_z/B (bottom panel). White curves show the magnetic field lines in both panels. Black curves in the bottom panel shows the contour of E_z/B.

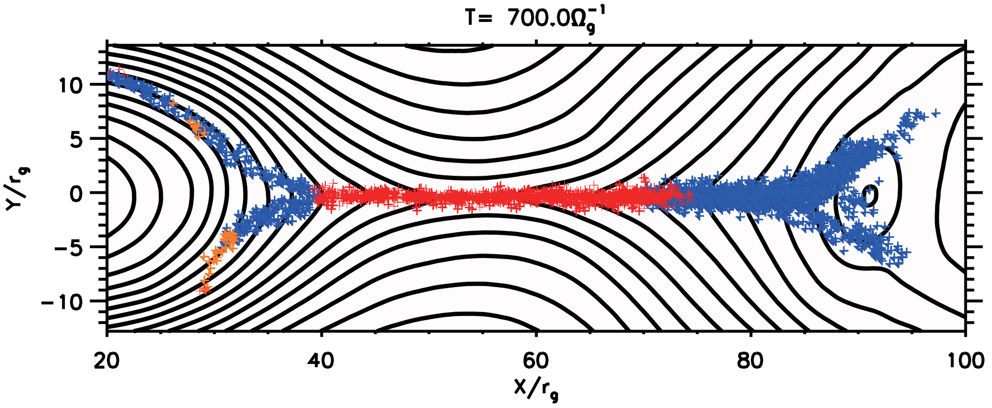

Figure F.7: Spacial distribution of the accelerated particles with the energy $\geq 5mc^2$. The red marks show the particles which Z component of the momentum is larger than other components, while blue and orange marks do those whose momentum component parallel to the $X-Y$ plane is dominant, respectively.

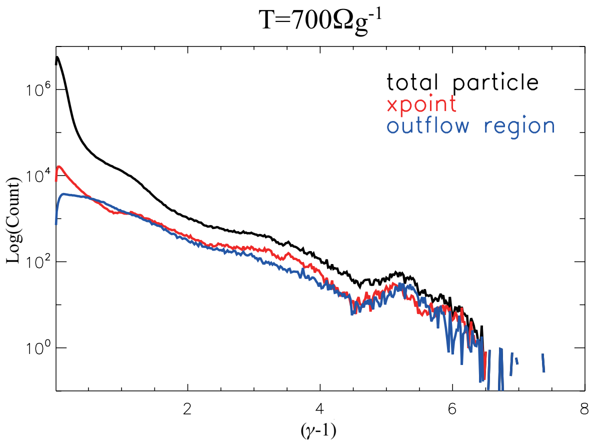

Figure F.8: Energy spectrum at $t = 700\Omega_g$. Black curve shows the spectrum of all particles, while red and blue curves do that around the acceleration region ($40 \le X/r_g \le 65$, $-2 \le Y/r_g \le 2$) and the outflow region ($65 < X/r_g \le 90$, $-2 \le Y/r_g \le 2$), respectively.

When the magnetic reconnection takes place, a strong electric field is induced by liberating the magnetic energy. Fig. F.6 shows the snapshot at $t = 700\Omega_g^{-1}$ when the magnetic reconnection takes place. Color contours show the plasma density (top panel) and E_z/B (bottom panel). The white curves show the magnetic field lines , while the black curves in the bottom panel show the contours of E_z/B. Around $(X, Y) = (55, 0)$ (acceleration region), strong electric fields ($|E_z/B > 1|$) are induced by the magnetic reconnection. This indicates that the electric field does not vanish in any reference frame and thus the MHD condition is violated. In such region, particles are strongly accelerated by the electric field in Z direction. The accelerated particles escape from the acceleration region by deflecting their orbits by the local magnetic field. These particles form plasmoids which are ejected into $\pm X$ direction (see the top panel in Fig. F.6). The outflow velocity $\sim 0.8c$ is close to the local Alfvén velocity. The maximum inflow velocity is $\sim 0.2c$. The plasmoid moving in X direction induces the electric field by $\boldsymbol{E} = -\boldsymbol{v} \times \boldsymbol{B}/c$. The induced electric field distributes more diffusively than that induced by the magnetic reconnection. Its field strength is smaller than that of the magnetic fields ($|E_z/B < 1$).

Fig. F.7 shows the spacial distribution of the accelerated particles. Red marks show the particles whose Z component of the momentum is larger than other components, while blue and orange marks do those whose X and Y component of the momentum are dominant, respectively. These particles have energy larger than $5mc^2$. The high energy particles are mainly distributed around the X point.

Fig. F.8 shows the energy spectrum at $t = 700\Omega_g^{-1}$. The black curve shows the spectrum of all particles, while the red and blue ones do that around the acceleration region ($40 \leq X/r_g \leq 65$, $-2 \leq Y/r_g \leq 2$) and the outflow region ($65 < X/r_g \leq 90$, $-2 \leq Y/r_g \leq 2$), respectively. Note that each spectrum is almost the same in high energy part ($\gamma > 5$). This indicates that the particles are mainly accelerated by the reconnection electric fields.

F.3 Summary & Discussions

We performed 2-dimensional PIC simulations for the pair plasma to study the current sheet formation in magnetic loops by shear flows and resulting magnetic reconnection. Magnetic field lines are twisted in the direction parallel to the shear flow. Inside the magnetic loops, the toroidal component of the magnetic field parallel to the shear flow dominates that of the poloidal component. Due to the enhanced magnetic pressure, magnetic loops expand in the direction perpendicular to the velocity gradient. The expansion speed is almost the same as the shear velocity. The magnetic field lines become anti-parallel inside the magnetic loops due to the expansion and form a current sheet between the anti-parallel magnetic fields. The current sheet is elongated in the direction perpendicular to the velocity gradient. The current sheet becomes thinner as well as increasing the current density. When the thickness of the current sheet is of order the gyro radius, the magnetic reconnection takes place.

The electric field induced by the magnetic reconnection can strongly accelerate particles. The accelerated particles escape from the acceleration region since their orbits are deflected by the magnetic fields. The escape (accelerated) particles form the plasmoids ejecting in $\pm X$ directions. The plasmoids also induce the electric field $\boldsymbol{E} = \boldsymbol{v} \times \boldsymbol{B}/c$ which distributes more diffusively than that induced by the magnetic reconnection. Particles are mainly accelerated by the electric field induced by the magnetic reconnection.

We showed that magnetic fields are generated ahead of the magnetic loops through the Weibel instability when the magnetic loops expand. Hededal et al. (2004) performed 3-dimensional PIC simulation of unmagnetized shocks for electron-ion plasma and showed that the electrons are accelerated when the Weibel instability is developed. When the instability grows, the ion and electron channels are created, which are responsible for generation of the magnetic fields. Since the ions have a larger inertia, the ion channel is more stable than that of electrons. When the electron flows into the ion channel, electron is accelerated by the electric fields. This acceleration cannot be expected in our simulation since we treat the pair plasma. The current channels merge each other faster in electron-positron plasma than in electron-ion plasma. When we include the ions, they can be accelerated ahead of the magnetic loops.

Another acceleration mechanism through the Weibel instability has been proposed by Zenitani & Hesse (2008b). They showed that the instability is developed in the reconnection jets. When the magnetic reconnection takes place, the plasma is ejected from the acceleration region. The interaction between the ejected particles and the ambient plasma triggers the growth of the Weibel instability. The orbits of the accelerated particles are deflected by the Weibel magnetic fields. The particles interact with the piled-up magnetic field (reconnected magnetic field) and are further accelerated by the electric field $\boldsymbol{E} = -\boldsymbol{v} \times \boldsymbol{B}/c$. This mechanism seems to be working ahead of the magnetic loops. The particles deflected their orbits by the generated magnetic fields continuously interact with the magnetic loops. Since the magnetic field is strong at the loop top, the particles can be accelerated by the induced electric fields.

References

Alcock, C., Farhi, E., & Olinto, A. 1986, Physical Review Letters, 57, 2088

Aptekar, R. L., Frederiks, D. D., Golenetskii, S. V., Il'inskii, V. N., Mazets, E. P., Pal'shin, V. D., Butterworth, P. S., & Cline, T. L. 2001, ApJS, 137, 227

Asano, E. 2007, PhD. thesis, Chiba Univ.

Asano, E., Uchida, T., & Matsumoto, R. 2005, PASJ, 57, 409

Barnes, C. W. & Sturrock, P. A. 1972, ApJ, 174, 659

Beloborodov, A. M. & Thompson, C. 2007, ApJ, 657, 967

Bethe, H. A., Brown, G. E., & Cooperstein, J. 1987, ApJ, 322, 201

Birdsall, C. K. & Langdon, A. B. 2001, Plasma Physics via Computer Simulations (New York, McGraw-Hill, 2001)

Birn, J., Drake, J. F., Shay, M. A., Rogers, B. N., Denton, R. E., Hesse, M., Kuznetsova, M., Ma, Z. W., Bhattacharjee, A., Otto, A., & Pritchett, P. L. 2001, J. Geophys. Res., 106, 3715

Birn, J. & Hesse, M. 2001, J. Geophys. Res., 106, 3737

Biskamp, D. 1986, Physics of Fluids, 29, 1520

Blackman, E. G. & Field, G. B. 1993, Physical Review Letters, 71, 3481

—. 1994, Physical Review Letters, 72, 494

Braithwaite, J. & Nordlund, Å. 2006, A&A, 450, 1077

Braithwaite, J. & Spruit, H. C. 2006, A&A, 450, 1097

Cameron, P. B., Chandra, P., Ray, A., Kulkarni, S. R., Frail, D. A., Wieringa, M. H., Nakar, E., Phinney, E. S., Miyazaki, A., Tsuboi, M., Okumura, S., Kawai, N., Menten, K. M., & Bertoldi, F. 2005, Nature, 434, 1112

Campana, S., Mangano, V., Blustin, A. J., Brown, P., Burrows, D. N., Chincarini, G., Cummings, J. R., Cusumano, G., Della Valle, M., Malesani, D., Mészáros, P., Nousek, J. A., Page, M., Sakamoto, T., Waxman, E., Zhang, B., Dai, Z. G., Gehrels, N., Immler, S., Marshall, F. E., Mason, K. O., Moretti, A., O'Brien, P. T., Osborne, J. P., Page, K. L., Romano, P., Roming, P. W. A., Tagliaferri, G., Cominsky, L. R., Giommi, P., Godet, O., Kennea, J. A., Krimm, H., Angelini, L., Barthelmy, S. D., Boyd, P. T., Palmer, D. M., Wells, A. A., & White, N. E. 2006, Nature, 442, 1008

Chandrasekhar, S. & Fermi, E. 1953, ApJ, 118, 116

Christon, S. P., Mitchell, D. G., Williams, D. J., Frank, L. A., Huang, C. Y., & Eastman, T. E. 1988, J. Geophys. Res., 93, 2562

Coroniti, F. V. 1990, ApJ, 349, 538

Denisenko, D. V. 2008, GRB Coordinates Network, 8114, 1

Drake, J. F., Swisdak, M., Cattell, C., Shay, M. A., Rogers, B. N., & Zeiler, A. 2003, Science, 299, 873

Drenkhahn, G. 2002, A&A, 387, 714

Drenkhahn, G. & Spruit, H. C. 2002, A&A, 391, 1141

Duncan, R. C. & Thompson, C. 1992, ApJ, 392, L9

Feroci, M., Caliandro, G. A., Massaro, E., Mereghetti, S., & Woods, P. M. 2004, ApJ, 612, 408

Forbes, T. G. & Priest, E. R. 1982, Sol. Phys., 81, 303

—. 1983, Sol. Phys., 84, 169

—. 1984, Sol. Phys., 94, 315

Ghosh, P., Angelini, L., & White, N. E. 1997, ApJ, 478, 713

Goldreich, P. & Julian, W. H. 1969, ApJ, 157, 869

Golenetskii, S. V., Ilinskii, V. N., & Mazets, E. P. 1984, Nature, 307, 41

Göğüş, E., Kouveliotou, C., Woods, P. M., Thompson, C., Duncan, R. C., & Briggs, M. S. 2001, ApJ, 558, 228

Harris, E. G. 1962, Nuovo Cimento, 23, 115

Hayashi, M. R., Shibata, K., & Matsumoto, R. 1996, ApJ, 468, L37+

Hededal, C. B., Haugbølle, T., Frederiksen, J. T., & Nordlund, Å. 2004, ApJ, 617, L107

Hesse, M., Schindler, K., Birn, J., & Kuznetsova, M. 1999, Physics of Plasmas, 6, 1781

Horiuchi, R. & Sato, T. 1997, Physics of Plasmas, 4, 277

Hoshino, M., Mukai, T., Terasawa, T., & Shinohara, I. 2001, J. Geophys. Res., 106, 25979

Hurley, K., Boggs, S. E., Smith, D. M., Duncan, R. C., Lin, R., Zoglauer, A., Krucker, S., Hurford, G., Hudson, H., Wigger, C., Hajdas, W., Thompson, C., Mitrofanov, I., Sanin, A., Boynton, W., Fellows, C., von Kienlin, A., Lichti, G., Rau, A., & Cline, T. 2005, Nature, 434, 1098

Hurley, K., Cline, T., Mazets, E., Barthelmy, S., Butterworth, P., Marshall, F., Palmer, D., Aptekar, R., Golenetskii, S., Il'Inskii, V., Frederiks, D., McTiernan, J., Gold, R., & Trombka, J. 1999, Nature, 397, 41

Ibrahim, A. I., Safi-Harb, S., Swank, J. H., Parke, W., Zane, S., & Turolla, R. 2002, ApJ, 574, L51

Ibrahim, A. I., Swank, J. H., & Parke, W. 2003, ApJ, 584, L17

Israel, G. L., Rea, N., Mangano, V., Esposito, P., Tiengo, A., Mereghetti, S., Gotz, D., Zane, S., Kennea, J., Perri, M., Cusumano, G., Burrows, D. N., Gehrels, N., Palmer, D., & Barthelmy, S. 2008, The Astronomer's Telegram, 1692, 1

Jaroschek, C. H., Lesch, H., & Treumann, R. A. 2004, ApJ, 605, L9

Karlický, M. 2008, ApJ, 674, 1211

Kato, Y., Hayashi, M. R., & Matsumoto, R. 2004, ApJ, 600, 338

Katz, J. I., Toole, H. A., & Unruh, S. H. 1994, ApJ, 437, 727

Kirk, J. G. & Skjæraasen, O. 2003, ApJ, 591, 366

Komissarov, S. S. 2002, MNRAS, 336, 759

Kouveliotou, C., Dieters, S., Strohmayer, T., van Paradijs, J., Fishman, G. J., Meegan, C. A., Hurley, K., Kommers, J., Smith, I., Frail, D., & Murakami, T. 1998, Nature, 393, 235

Krimm, H. A., Beardmore, A. P., Gehrels, N., Page, K. L., Palmer, D. M., Starling, R. L. C., & Ukwatta, T. N. 2008, GRB Coordinates Network, 8312, 1

Landau, L. D. & Lifshitz, E. M. 1959, Fluid mechanics (Course of theoretical physics, Oxford: Pergamon Press, 1959)

—. 1975, The classical theory of fields (Course of theoretical physics - Pergamon International Library of Science, Technology, Engineering and Social Studies, Oxford: Pergamon Press, 1975, 4th rev.engl.ed.)

Larrabee, D. A., Lovelace, R. V. E., & Romanova, M. M. 2003, ApJ, 586, 72

Livio, M. & Taam, R. E. 1987, Nature, 327, 398

Low, B. C. 1982, ApJ, 261, 351

—. 1984, ApJ, 281, 392

Lyubarsky, Y. & Kirk, J. G. 2001, ApJ, 547, 437

Lyubarsky, Y. & Liverts, M. 2008, ApJ, 682, 1436

Lyubarsky, Y. E. 2005, mnras, 358, 113

Lyutikov, M. 2002, Physics of Fluids, 14, 963

—. 2003, MNRAS, 346, 540

—. 2006, MNRAS, 367, 1594

Lyutikov, M. & Blandford, R. 2003, astro-ph/0312347

Lyutikov, M. & Uzdensky, D. 2003, ApJ, 589, 893

Mayle, R. & Wilson, J. R. 1988, ApJ, 334, 909

Mazets, E. P., Cline, T. L., Aptekar, R. L., Frederiks, D. D., Golenetskii, S. V., Il'inskii, V. N., & Pal'shin, V. D. 2005, ArXiv Astrophysics e-prints

Mazets, E. P. & Golenetskii, S. V. 1981, Ap&SS, 75, 47

Mazets, E. P., Golentskii, S. V., Ilinskii, V. N., Aptekar, R. L., & Guryan, I. A. 1979, Nature, 282, 587

Meier, D. L., Koide, S., & Uchida, Y. 2001, Science, 291, 84

Mereghetti, S. 2008, A&A Rev., 15, 225

Mereghetti, S., Tiengo, A., Esposito, P., Götz, D., Stella, L., Israel, G. L., Rea, N., Feroci, M., Turolla, R., & Zane, S. 2005, ApJ, 628, 938

Mihalas, D. & Mihalas, B. W. 1984, Foundations of radiation hydrodynamics (New York, Oxford University Press, 1984, 731 p.)

Mikic, Z., Barnes, D. C., & Schnack, D. D. 1988, ApJ, 328, 830

Murakami, T., Tanaka, Y., Kulkarni, S. R., Ogasaka, Y., Sonobe, T., Ogawara, Y., Aoki, T., & Yoshida, A. 1994, Nature, 368, 127

Nakagawa, Y. E., Yoshida, A., Hurley, K., Atteia, J.-L., Maetou, M., Tamagawa, T., Suzuki, M., Yamazaki, T., Tanaka, K., Kawai, N., Shirasaki, Y., Pelangeon, A., Matsuoka, M., Vanderspek, R., Crew, G. B., Villasenor, J. S., Sato, R., Sugita, S., Kotoku, J., Arimoto, M., Pizzichini, G., Doty, J. P., & Ricker, G. R. 2007, PASJ, 59, 653

Olive, J.-F., Hurley, K., Sakamoto, T., Atteia, J.-L., Crew, G., Ricker, G., Pizzichini, G., Barraud, C., & Kawai, N. 2004, ApJ, 616, 1148

Palmer, D. M., Barthelmy, S., Gehrels, N., Kippen, R. M., Cayton, T., Kouveliotou, C., Eichler, D., Wijers, R. A. M. J., Woods, P. M., Granot, J., Lyubarsky, Y. E., Ramirez-Ruiz, E., Barbier, L., Chester, M., Cummings, J., Fenimore, E. E., Finger, M. H., Gaensler, B. M., Hullinger, D., Krimm, H., Markwardt, C. B., Nousek, J. A., Parsons, A., Patel, S., Sakamoto, T., Sato, G., Suzuki, M., & Tueller, J. 2005, Nature, 434, 1107

Palmer, D. M. & Barthelmy, S. D. 2008, GRB Coordinates Network, 8115, 1

Parker, E. N. 1957, Physical Review, 107, 830

Petschek, H. E. 1964, in The Physics of Solar Flares, ed. W. N. Hess, 425–+

Prendergast, K. H. 2005, MNRAS, 359, 725

Priest, E. & Forbes, T. 2000, Magnetic Reconnection (Magnetic Reconnection, by Eric Priest and Terry Forbes, pp. 612. ISBN 0521481791. Cambridge, UK: Cambridge University Press, June 2000.)

Rea, N., Esposito, P., Krimm, H. A., Palmer, D. M., Mereghetti, S., Tiengo, A., & Israel, G. L. 2008a, GRB Coordinates Network, 8313, 1

—. 2008b, The Astronomer's Telegram, 1756, 1

Rea, N., Israel, G. L., Mereghetti, S., Tiengo, A., Zane, S., Turolla, R., & Stella, L. 2006, Chinese Journal of Astronomy and Astrophysics Supplement, 6, 010000

Rothschild, R. E., Kulkarni, S. R., & Lingenfelter, R. E. 1994, Nature, 368, 432

Sato, T. & Hayashi, T. 1979, Physics of Fluids, 22, 1189

Scholer, M. 1989, J. Geophys. Res., 94, 8805

Spitkovsky, A. 2005, in KITP Program: Physics of Astrophysical Outflows and Accretion Disks

Spitkovsky, A. 2006, ApJ, 648, L51

Stone, J. M., Hawley, J. F., Evans, C. R., & Norman, M. L. 1992, ApJ, 388, 415

Strohmayer, T. E. & Ibrahim, A. I. 2000, ApJ, 537, L111

Sweet, P. A. 1958, in IAU Symposium, Vol. 6, Electromagnetic Phenomena in Cosmical Physics, ed. B. Lehnert, 123–+

Swisdak, M., Liu, Y.-H., & Drake, J. F. 2008, ApJ, 680, 999

Terasawa, T., Tanaka, Y. T., Takei, Y., Kawai, N., Yoshida, A., Nomoto, K., Yoshikawa, I., Saito, Y., Kasaba, Y., Takashima, T., Mukai, T., Noda, H., Murakami, T., Watanabe, K., Muraki, Y., Yokoyama, T., & Hoshino, M. 2005, Nature, 434, 1110

Thompson, C. & Duncan, R. C. 1993, ApJ, 408, 194

—. 1995, MNRAS, 275, 255

—. 2001, ApJ, 561, 980

Thompson, C., Lyutikov, M., & Kulkarni, S. R. 2002, ApJ, 574, 332

Uchida, T. 1997a, Phys. Rev. E, 56, 2181

—. 1997b, Phys. Rev. E, 56, 2198

Ugai, M. & Tsuda, T. 1977, Journal of Plasma Physics, 17, 337

van Paradijs, J., Taam, R. E., & van den Heuvel, E. P. J. 1995, A&A, 299, L41+

Vasisht, G., Kulkarni, S. R., Frail, D. A., & Greiner, J. 1994, ApJ, 431, L35

von Kienlin, A. & Briggs, M. S. 2008, GRB Coordinates Network, 8315, 1

Watanabe, N. & Yokoyama, T. 2006, ApJ, 647, L123

Weibel, E. S. 1959, Physical Review Letters, 2, 83

Woods, P. M., Gogus, E., & Kouveliotou, C. 2008, The Astronomer's Telegram, 1691, 1

Woods, P. M., Kouveliotou, C., Göğüş, E., Finger, M. H., Swank, J., Smith, D. A., Hurley, K., & Thompson, C. 2001, ApJ, 552, 748

Woods, P. M. & Thompson, C. 2006, in Lewin W., van der Klis M., eds, Cambridge Astrophys. Ser. Vol. 39, Compact stellar X-ray sources, Cambridge Univ. Press, Cambridge

Yan, M., Lee, L. C., & Priest, E. R. 1992, J. Geophys. Res., 97, 8277

Yokoyama, T. & Shibata, K. 1994, ApJ, 436, L197

Zenitani, S. & Hesse, M. 2008a, ApJ, 684, 1477

—. 2008b, Physics of Plasmas, 15, 022101

Zenitani, S. & Hoshino, M. 2001, ApJ, 562, L63

—. 2005, Physical Review Letters, 95, 095001

—. 2007, ApJ, 670, 702

—. 2008, ApJ, 677, 530